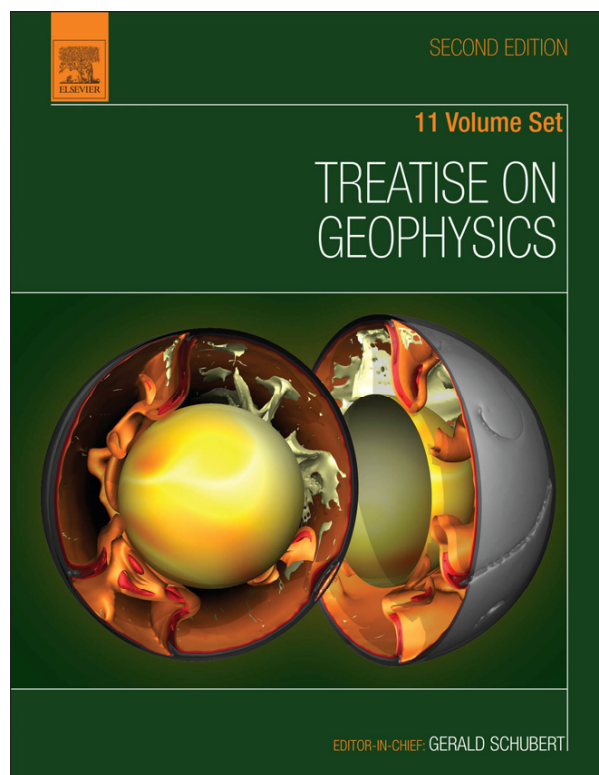


Provided for non-commercial research and educational use.  
Not for reproduction, distribution or commercial use.

This article was originally published in *Treatise on Geophysics, Second Edition*, published by Elsevier, and the attached copy is provided by Elsevier for the author's benefit and for the benefit of the author's institution, for non-commercial research and educational use including without limitation use in instruction at your institution, sending it to specific colleagues who you know, and providing a copy to your institution's administrator.



All other uses, reproduction and distribution, including without limitation commercial reprints, selling or licensing copies or access, or posting on open internet sites, your personal or institution's website or repository, are prohibited. For exceptions, permission may be sought for such use through Elsevier's permissions site at:

<http://www.elsevier.com/locate/permissionusematerial>

Avouac J.-P., and Leprince S Geodetic Imaging Using Optical Systems. In: Gerald Schubert (editor-in-chief) *Treatise on Geophysics, 2<sup>nd</sup> edition, Vol 3*. Oxford: Elsevier; 2015. p. 387-424.

## 3.13 Geodetic Imaging Using Optical Systems

J-P Avouac and S Leprince, California Institute of Technology, Pasadena, CA, USA

© 2015 Elsevier B.V. All rights reserved.

<b>3.13.1</b>	<b>Introduction</b>	387
<b>3.13.2</b>	<b>Principles</b>	388
3.13.2.1	Problem to be Solved	388
3.13.2.2	Measurement Principle	389
<b>3.13.3</b>	<b>Background Information on Optical Sensing Systems</b>	391
3.13.3.1	Geodetic Scanning Laser	391
3.13.3.2	Passive Optical Imaging	394
<b>3.13.4</b>	<b>Matching Techniques</b>	395
3.13.4.1	From 3-D to 2-D Matching	395
3.13.4.2	Algorithms for 3-D Matching	397
3.13.4.3	Algorithms for 2-D Matching	398
3.13.4.3.1	Homogeneous rotation and heterogeneous translation	398
3.13.4.3.2	Optical flow	399
3.13.4.3.3	Statistical correlation	399
3.13.4.3.4	Phase correlation	400
3.13.4.3.5	Regularized solutions and large displacements	400
<b>3.13.5</b>	<b>Geometric Modeling and Processing of Passive Optical Images</b>	400
3.13.5.1	The Orthorectification	400
3.13.5.1.1	The orthorectification mapping	401
3.13.5.1.2	Resampling the image	401
3.13.5.2	Bundle Adjustment	402
3.13.5.3	Stereo Imaging	402
3.13.5.4	Processing Flowchart	403
3.13.5.5	Performance, Artifacts, and Limitations	404
<b>3.13.6</b>	<b>Applications to Coseismic Deformation</b>	406
3.13.6.1	Usefulness of Coseismic Deformation Measurement from Image Geodesy	406
3.13.6.2	Surface Displacement in 2-D due to the 1999 Mw 7.6 Chichi Earthquake, Measured from SPOT Images	408
3.13.6.3	Surface Displacement in 2-D due to the 2005 Mw 7.6 Kashmir Earthquake, Measured from ASTER Images	410
3.13.6.4	Surface Displacement in 2-D due to the 1999 Mw 7.1 Hector Mine Earthquake Measured from SPOT Images	411
3.13.6.5	Surface Displacement in 2-D due to the 1999 Mw 7.1 Hector Mine Earthquake Measured from Air Photos	413
3.13.6.6	Surface Displacement in 3-D due to the 2010 Mw 7.2 El Mayor–Cucapah Earthquake from LiDAR and Optical Images Stereomatching	414
<b>3.13.7</b>	<b>Applications to Geomorphology and Glacier Monitoring</b>	415
3.13.7.1	Glacier Monitoring	415
3.13.7.2	Earthflows	417
3.13.7.3	Dune Migration	420
<b>3.13.8</b>	<b>Conclusion</b>	420
<b>References</b>		422

### 3.13.1 Introduction

It was realized soon after its invention that photography could be used onboard airborne platforms, initially kites and balloons, for topographic surveying. The first experiment, inspired by the work of mathematician François Arago on image geometry, was actually carried out by Aimé Laussedat in 1849, laying the foundations for photogrammetry (Laussedat, 1854, 1859). There is nowadays a vast archive of photographs taken from various types of aircrafts and spacecrafts available from various national and international agencies and commercial companies. The archive is growing fast as numerous Earth-observing systems or air photo topographic programs are delivering images with ground resolution down to 50 cm or better.

Similarly, it also did not take long after the laser was invented by the end of the 1950s before it was used for geodesy and terrain mapping. Over the last decade, systems that operate a laser scanning of the Earth's surface have emerged as new powerful optical systems to sense the Earth's surface from the ground and from airborne and spaceborne platforms (e.g., Carter et al., 2007; French, 2003; Slatton et al., 2007). Geodetic laser scanning is generally referred to as light detection and ranging (LiDAR) or airborne laser swath mapping. Although they differ in fundamental ways, passive and active optical sensing systems both measure a signal reflected at the Earth's surface toward a collector and focused on some sensor. These data provide information on the geometry and physical properties of the Earth's surface. The surface of the Earth is

continuously evolving as a result of geodynamic, climatic, environmental, and human factors. Time series of optical remote sensing data can then in principle be used to monitor those changes and investigate the processes at their origin.

Data collected from optical remote sensing systems can effectively be used to measure the evolution of the topographic surface with enough accuracy to allow investigation of a variety of processes. Probably one of the earliest applications of this approach has been the measurement of ice flow velocity from tracking features such as crevasses or debris on a series of aerial and satellite images (Brecher, 1986; Lucchitta and Ferguson, 1986), prompting later efforts to develop automatic procedures (Scambos et al., 1992). Application of this approach to the solid Earth, for example, the measurement of ground displacements or topographic changes induced by earthquakes and geomorphic processes, has been explored in a number of studies (e.g., Aryal et al., 2012; Corsini et al., 2009; Crippen, 1992; Delacourt et al., 2007; Käab et al., 1997; Mackey et al., 2009; Oskin et al., 2012; Roering et al., 2009; Van Puymbroeck et al., 2000). This is a rapidly growing area of research due to the need for a better understanding of those processes, motivated in particular by the need to monitor and understand better the impact of climate change on the landscape and water resources and the growing body of optical remote sensing techniques (Bishop et al., 2012; Tarolli et al., 2009).

In this chapter, we review the methods used in such studies and illustrate with particular applications the measurement of the Earth's surface changes produced by earthquakes, ice flow, landslides, and sand dune migration. We are concerned here with characterizing the geometric changes of the Earth's surface, which have occurred between various epochs of acquisition. We do not cover the literature on the characterization of tectonic or geomorphic processes from morphometric measurements. The reader is referred to textbooks or review papers on that topic (Burbank and Anderson, 2001; Kirby and Whipple, 2012). We focus on optical remote sensing systems but many of the techniques described here apply to radar images. With regard to the processing and exploitation of radar images, the reader is referred to review papers on this technique (Massonnet and Feigl, 1998) and to the chapter by Simons and Rosen in this same volume (Chapter 3.12).

Here, we start with describing the principle of how optically sensed terrain models might be used to quantify geologic and geomorphological processes. We next move on with describing practical implementations for the exploitation of either LiDAR or optical images. We do not review in-depth photogrammetric and LiDAR techniques, but we mention the aspects of importance with regard to applications to Earth sciences. We illustrate the potential and limitations of these techniques based on an overview of case studies, and finally, we discuss research perspectives.

### 3.13.2 Principles

#### 3.13.2.1 Problem to be Solved

We are interested in quantitatively characterizing geometric changes of the Earth's surface topography between two epochs of acquisition of remote sensing optical data (Figure 1). Let us consider that the data provide some rendering of the Earth's surface,  $S_1$  and  $S_2$  at time  $t_1$  and  $t_2$ , respectively.  $S_i$  would characterize the topographic surface at time  $t_i$  with respect to a geodetic reference frame (represented by  $Oxy$  in Figure 1 where the problem is sketched in 2-D), which in practice could be a particular realization of the International Terrestrial Reference Frame (Altamimi et al., 2002) associated to a particular datum and its optical reflective properties. The optical properties of the surface and the geometry contribute to determining the radiometry measured by any optical system, whether passive or active. The surface cover (vegetation and human infrastructures) and the substrate determine these properties.

In practice, the geometry is represented by a digital elevation model (DEM), which is a discretized representation of the topography elevation. The sampling grid can be regular or not depending on the technique used.

Let us now consider a material point in the subsurface located at  $M_1$  at epoch  $t_1$ . This same point lies at  $M_2$  at epoch  $t_2$ , with respect to the same geodetic reference frame. In practice, the displacement vector  $(d_x, d_y, d_z)$  could be due to tectonics (e.g., an earthquake) or other processes such as landslide or ice flow as we will see in the application section

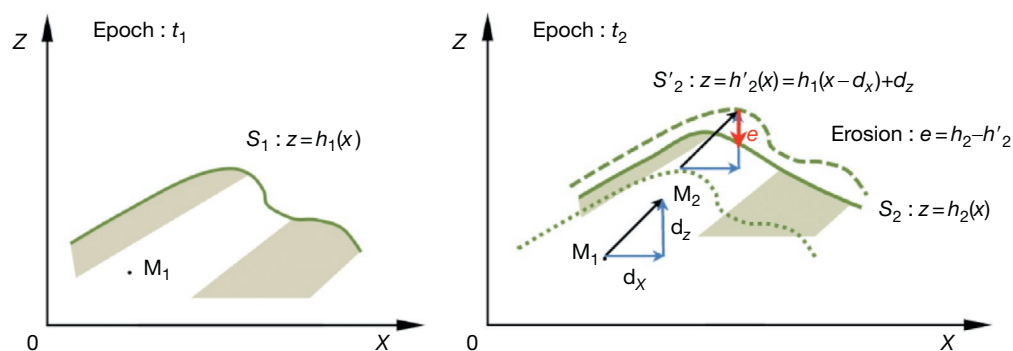


**Figure 1** Schematic 2-D representation of the problem to solve. We are interested in characterizing quantitatively geometric changes of the Earth's surface topography between epochs  $t_1$  and  $t_2$ .  $S_1$  and  $S_2$  refer to the Earth's surface at time  $t_1$  and  $t_2$ , respectively, with respect to a geodetic reference frame, represented by  $Oxy$ . The Earth's surface may have changed as a result of displacement of the subsurface medium with respect to the reference frame, represented by the displacement vector  $M_1M_2$ . It may also have changed as a result of erosion or sedimentation at the Earth's surface, represented by the scalar quantity  $e$ .

in the succeeding text. Note that the medium around  $M_1$  could have deformed although this is not represented in **Figure 1** for the sake of simplicity. The surface topography, represented by  $S_1$  and  $S_2$  at epochs 1 and 2, respectively, is not a passive marker in general. Between epochs  $t_1$  and  $t_2$ , it may have evolved as a result of erosion or sedimentation. As a result, advective transport of the initial topography yields a surface  $S'_2$ , which differs from the topography at epoch  $t_2$  (dashed line in **Figure 1**). The elevation difference between  $S'_2$  and  $S_2$  is the measurement that quantifies the evolution of the topography due to erosion ( $h_2 < h'_2$ ) or sedimentation ( $h_2 > h'_2$ ). The applications reviewed in this chapter hinge on the measurements of either topographic changes, that is, the difference between  $h_2$  and  $h'_2$ , a scalar field  $e = h_2 - h'_2$ , or the ground displacement vector field  $(d_x, d_y, d_z)$  (represented by  $M_1M_2$  in **Figure 1**). The information derived from sensing the Earth's surface with optical systems is, however, inherently insufficient to solve for both the change of elevation of the topography and the ground displacement vector. In principle, any erosion or sedimentation should make it impossible to decompose the measured difference in elevation between two epochs into a ground displacement  $(d_x, d_y, d_z)$  and erosion of the topography. Thus, in practice, one or the other term must be assumed negligible or known independently. Often, these assumptions appear natural given the context of the observations and are not always stated explicitly.

In most geodetic applications, it is assumed that the topography is advected as a passive marker. It follows that the displacement field, which allows matching the topography at epochs  $t_1$  and  $t_2$ , would also be matching the radiometric texture of the surface, provided that it has not changed between the two epochs (as they might have due to change of the land cover, surface hydrology, or human activities). Let us stress here the fundamental difference between the 'geodetic optical imaging' techniques described in this chapter and standard geodetic techniques, which allow measuring directly the displacements of material points  $M_1M_2$ .

### 3.13.2.2 Measurement Principle

Let us assume that the same portion of the Earth's surface was sensed at two epochs from optical sensing methods and that these data were used to produce perfectly registered DEMs and some representation of surface optical properties at the two epochs. Let us refer to  $h_1$  and  $h_2$  as the functions describing the topographic surface at time  $t_1$  and  $t_2$ , respectively. The DEMs are discrete sampling of these functions. In general, the elevation change measured from the difference between the topographic surfaces,  $h_2 - h_1$ , will combine the effect of advection and erosion,  $e(x, y)$ , of the surface (**Figure 1**):

$$h_2(x, y) - h_1(x, y) = h_1(x - d_x, y - d_y) + d_z(x, y) - h_1(x, y) + e(x, y) \quad [1a]$$

The term in the brackets on the right side represents the elevation change due to horizontal advection of the topography. Assuming that this equation can be approximated by a Taylor expansion to first order, we get

$$h_2(x, y) - h_1(x, y) \approx d_z(x, y) - d_x(x, y) \frac{\partial h_1}{\partial x}(x, y) - d_y(x, y) \frac{\partial h_1}{\partial y}(x, y) + e(x, y) \quad [1b]$$

If ground displacements can be neglected, changes of the topography are most simply characterized by differencing the two topographic surfaces:

$$e = h_2 - h_1 \quad [2]$$

This yields directly an estimate of erosion ( $e < 0$ ) or sedimentation ( $e > 0$ ) at the Earth's surface (**Figure 2**). As erosion and sedimentation presumably reset the surface optical properties, this measurement is in principle the only one that is meaningful in the presence of erosion or sedimentation. The measurement requires essentially some technique to resample the two DEMs on a common grid. This resampling procedure should in principle take into account how the DEMs were produced so as to respect the physics of the measuring technique. Resampling errors will inevitably be introduced.

In practice, DEMs produced independently from the data acquired at different epochs are not perfectly registered. As a result, differencing the topographic surfaces may, for a large part, reflect the resulting bias with registration errors possibly in excess of the signal of interest. **Figure 1** can be taken to illustrate this issue if  $(d_x, d_y, d_z)$  is now meant to represent a misregistration  $(\epsilon_x, \epsilon_y, \epsilon_z)$ . Due to the bias introduced by the misregistration, eqn [2] becomes

$$h_2(x, y) - h_1(x, y) = e(x, y) + h_1(x - \epsilon_x, y - \epsilon_y) - h_1(x, y) \quad [3a]$$

or in its Taylor expansion form

$$h_2(x, y) - h_1(x, y) \approx e(x, y) + \epsilon_z(x, y) - \epsilon_x(x, y) \frac{\partial h_1}{\partial x}(x, y) - \epsilon_y(x, y) \frac{\partial h_1}{\partial y}(x, y) \quad [3b]$$

The data analysis then requires a procedure for precise co-registration of the DEMs so as to minimize this bias. In most instances, the co-registration will be achieved by assuming that some particular areas have not experienced any topographic changes (the topographic differences in those areas should be null) or by using a priori constraints on the displacements at some ground control points (GCP). In general, DEM differencing will therefore reflect the combined effects of misregistration, resampling errors, and advective transport of the topography.

If the topography is assumed to have been transported advectively, in which case  $e = 0$  (**Figure 3**), the 3-D displacement field between two epochs might in principle be retrieved from matching the two DEMs. This requires some technique for matching DEMs in 3-D. The matching procedure solves for the displacement field vector  $(d_x, d_y, d_z)$ , which satisfies

$$h_2(x, y) = h_1(x - d_x, y - d_y) + d_z(x, y) \quad [4a]$$

or in its Taylor expansion form

$$h_2(x, y) - h_1(x, y) \approx d_z(x, y) - d_x(x, y) \frac{\partial h_1}{\partial x}(x, y) - d_y(x, y) \frac{\partial h_1}{\partial y}(x, y) \quad [4b]$$

Equation [4b] illustrates that the determination of the displacement field from matching the topography measured at

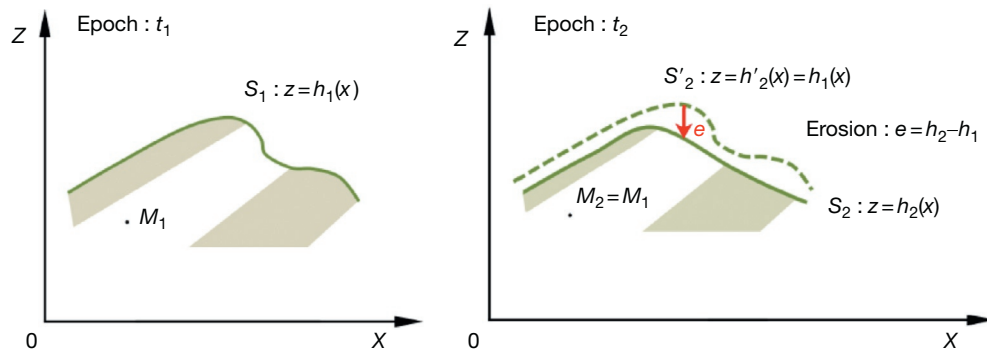


**Figure 2** Simplified version of **Figure 1** in the case with no advective transport of the subsurface ( $M_1=M_2$ ). The Earth's surface may have changed as a result of erosion or sedimentation represented by  $e$ .

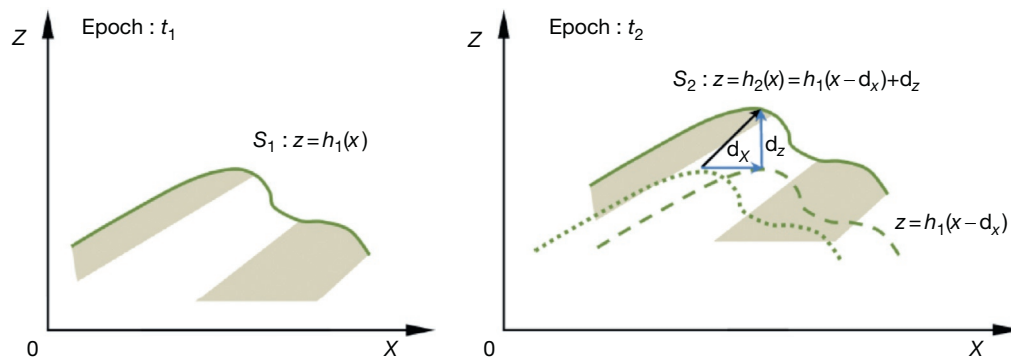


**Figure 3** Simplified version of **Figure 1** in the case with no erosion nor sedimentation. The Earth's surface is simply advected according to ground displacement vector field  $M_1/M_2$ .

two epochs is intrinsically an ill-posed problem: only the displacement along the gradient of the topography can be determined. Some assumptions are therefore needed regarding the regularity of the displacement field.

A simple procedure to regularize the matching problem (whether the quantity to be matched is the topography or any other scalar field) is to assume that the displacement field is continuous and varies smoothly (continuously differentiable). In that case, the horizontal displacement vector at a given point  $M_1$  can be determined from optimizing the matching between two windows of the same size  $w$  centered on  $M_1$  in  $h_1$  and on  $M_2$  in  $h_2$  as a function of the position  $M_2$  (**Figure 3**). For the regularization to be effective, the window size must be large enough so that the direction of topographic gradient varies significantly within that window. In practice, this requires the window size to be at least five to ten times larger than the average distance between measurements. The measurement provides an estimate of some average of displacement within that window. The nature of the averaging depends on the choice of a particular matching procedure. An important implication is that the displacement field is always resolved with a lower spatial resolution than the original DEM. In principle, regularization can be achieved with a relatively small matching window,  $3 \times 3$ , for example, for a scene rich in small-scale features of various orientations. Images from natural scenes generally require larger windows. The spatial

resolution is therefore generally no better than about five times the ground sampling distance (GSD) of the two stereoscopic optical images.

In the case of DEMs obtained from geodetic laser scanning, some radiometric information (the reflected intensity or the waveform of the reflected pulse) might be available in addition to the geographic coordinates of the scanned points. This information can in principle be used to optimize and help regularize the matching problem (again assuming the advective transport of the topography). This requires that the radiometric measurement can be converted into a stationary property of the ground's surface. In practice, the effects of the atmosphere and changes of the land cover can be a limitation.

In the case where the DEMs were computed from stereoscopic pairs of images, matching of DEMs is, however, not an optimal approach. This is so because DEMs generally fall short of representing accurately the information contained in the original data used to construct the topography. The radiometry at one pixel of an optical image depends on the surface's optical properties (determined by the land cover and substrate) and local topography (terrain roughness and average slope at the scale of the sensed spot on the ground), modulated by the atmospheric filter and transfer function of the optical system. If this texture is advectively transported with the topography, it is then a richer source of information on ground displacement than the DEM itself. It follows that ground displacements can

be measured more accurately by matching the image texture, very much the same way parallax offsets are measured to calculate DEMs. In addition, from a mathematical point of view, matching the radiometry and matching the topography are equivalent problems, both ill-posed. However, the topographic and radiometric gradients do not need to be parallel so that when radiometry is used, the determination of the displacement field is in principle less of an ill-posed problem. Note, however, that this is not true if the surface has a uniform albedo as the radiometry will then be entirely determined by the topography (e.g., sand dunes). Regularization of the matching problem is less stringent as the optical images generally have more texture than the DEMs at high spatial frequencies, simply because the DEMs are themselves often produced from the determination of stereoscopic offsets from matching the images. The regularization of the matching problem imposes that the DEMs have a lower spatial resolution than the images they were derived from.

The measurement of surface displacements from optical remote sensing data or directly from DEMs thus relies on matching measurements acquired at different epochs. In essence, matching techniques yield at any point of a reference dataset, a measurement of the vector field that best brings into coincidence a window centered on that point with a corresponding window in the second dataset. The output of the matching procedure is a vector field (Figures 4 and 5), which can be represented by shaded representation of the horizontal and vertical components in 3-D, as will be the case in the studies shown in the succeeding text.

As an illustration, Figure 6 shows the output from matching two Satellite Pour l'Observation de la Terre (SPOT) images, with a ground resolution of 10 m, acquired before and after the 1999 Mw 7.1 Hector Mine earthquake (Leprince et al., 2007). These images were orthorectified, to remove stereoscopic distortions due to the topography, and correlated using the methodology described in the succeeding text and a preexisting regional DEM. In this case, the offset field between the two orthoimages should show both horizontal displacements due to the earthquake and orthorectification errors. Clearly, the offset field is dominated by the ground displacement induced by the earthquake: the surface rupture shows up as a discontinuity of surface displacements. Profiles that run across the fault trace can be used to measure surface fault slip with accuracy better than 1 m (1/10 of pixel size). In this particular case, the offsets due to inaccurate modeling of stereoscopic effects related to the topography are small compared to the amplitude of the displacement signal. In most studies, reduction of these artifacts is a critical challenge.

In principle, the approach outlined here might be applied to passive or active optical data. In both cases, the exploitation of optical remote sensing data for documenting geometric changes of the Earth's surface requires some model of the imaging system, namely, a model that allows projecting back on the surface the information collected by the optical sensor. Recent advances in geodetic imaging from optical methods have, for a great deal, resulted from the improved accuracy of this geometric modeling. In the following section, we provide background information on optical sensing systems relevant to the development of such models.

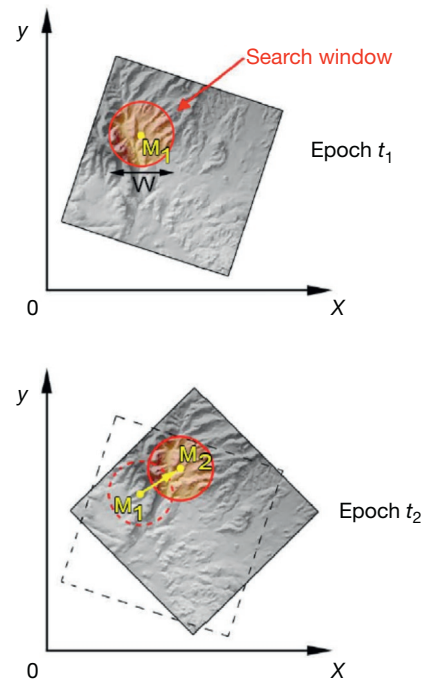


**Figure 4** Scheme of the matching procedure used to determine offsets between two datasets (two images or two DEMs and two clouds of LiDAR data). Because the matching (eqn [4]) is intrinsically ill-posed, the offset vector is determined from optimizing the matching between a window centered on a running point  $M_1$  in the dataset acquired at epoch  $t_1$  and a search window of same size in the second dataset. The window size must be large enough that it contains enough texture to solve for the matching problem. The measured offset is the vector  $M_1M_2$ , where  $M_2$  is the center of the best matching position of the search window in the second dataset. The principle holds in 2-D, as represented here, and in 3-D.

### 3.13.3 Background Information on Optical Sensing Systems

A key element in image geodesy, as with photogrammetry, is the proper modeling of the imaging system so that the accuracy of the projection on the Earth's surface of the signal measured by the optical sensing system meets geodetic standards. The modeling is specific to the particular imaging system. It is therefore important that the users be aware of the various elements that determine this geometric modeling and the various potential factors of geometric distortions. These distortions introduce misregistrations that, if not compensated for, will bias the measurement of topographic changes. The focus of this section is therefore to introduce those factors in the case of both active optical sensing and passive optical sensing.

#### 3.13.3.1 Geodetic Scanning Laser

It was not long after the laser was invented at the end of the 1950s that it started being used from space to sense the surface of Earth satellites and other planets (Arnold, 1967; Kovalevsky and Barlier, 1967). The principle of the geodetic laser scanning is simple (e.g., Baltasvias, 1999; Carter et al., 2007) (Figure 7). The laser technology allows the production of short intense pulses of monochromatic light. A variety of instruments that

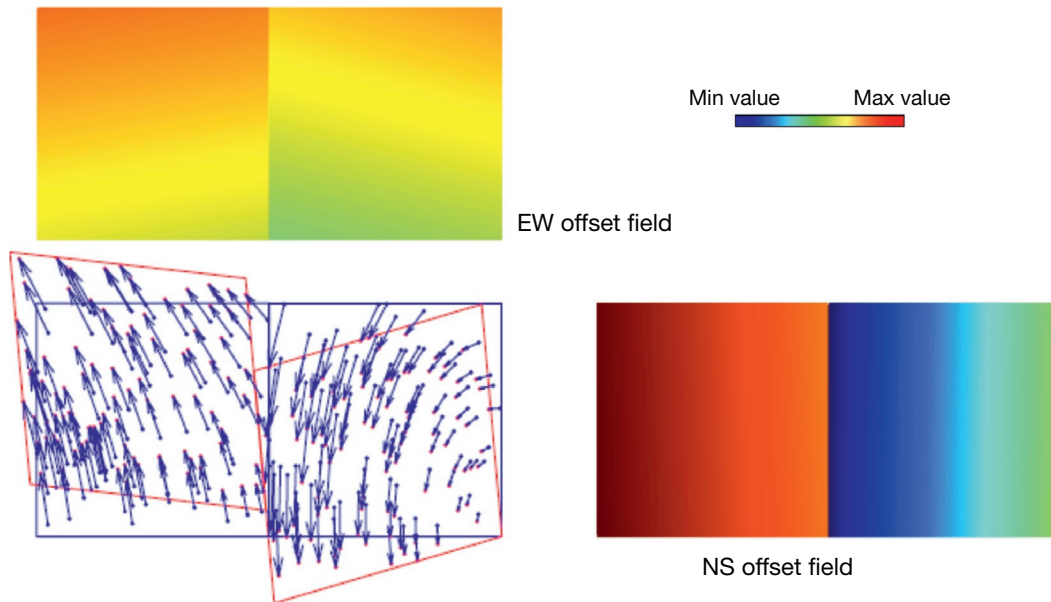


**Figure 5** The output of the matching procedure between two datasets is an offset field, which can be represented as a vector field or as scalar fields for individual components. Offset can be measured in the space or image space. In the space domain, those offset would represent ground displacement and potential misregistrations of the dataset. The figure represents schematically the horizontal displacement field due to an earthquake corrupted by registration errors.

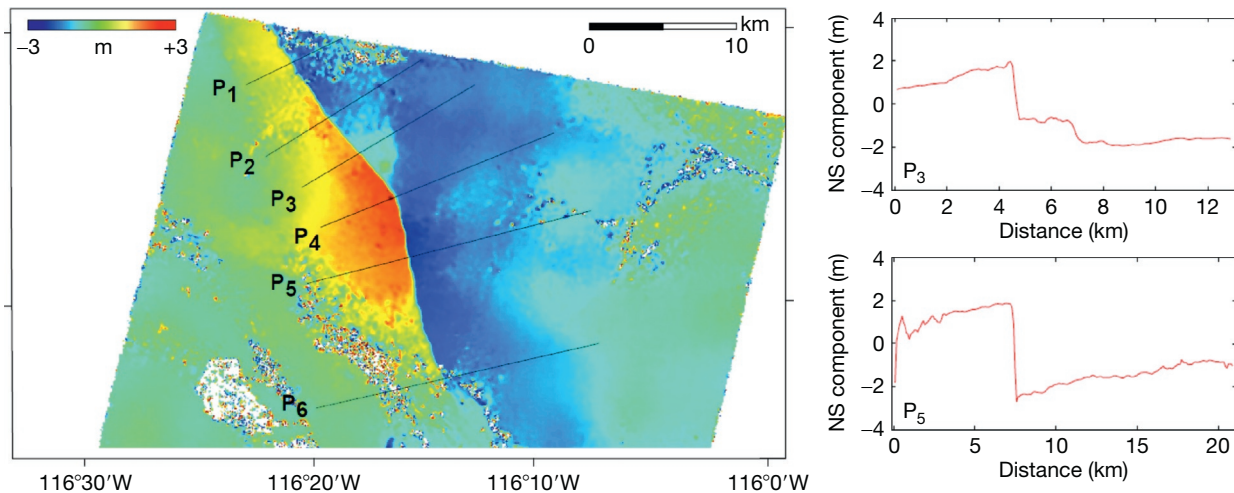


**Figure 6** North component (positive to the North) of the coseismic displacement field due to the 1999 Mw 7.1 Hector Mine earthquake in California measured from correlated SPOT 2 and SPOT 4 monochromatic images with 10 m GSD acquired on 12 August 1998 and 10 August 2000. Both images were orthorectified and co-registered on a 10 m-resolution grid using COSI-Corr. Offsets were measured from subpixel correlation with a  $32 \times 32$ -pixel sliding window and a 16-pixel step. The offset field was denoised using the nonlocal means filter (Buades et al., 2008). The standard deviation on individual measurements is around 0.8 m. Right panels show 2 km wide swath profiles across the fault trace. These profile showing a clear discontinuity of surface displacement at the fault trace with up to 5.5 m right-lateral strike slip.

differ with regard to the energy per pulse, the number of pulses per second, and the electro-optical scanning system can be operated from the ground, aircraft, or space platforms. Lasers for airborne geodetic applications generate 5–10 ns long pulses with a frequency 50–150 kHz at a wavelength in the infrared (1064 nm, e.g., for neodymium-doped yttrium aluminum garnet) (e.g., Carter et al., 2007). The narrow bandwidth allows tight collimation of a beam, which is deflected toward the

target using an oscillating mirror. An optical system collects, filters, and focuses the reflected pulse on a photodetector. The two-way travel time is measured and provides a determination of the range. The uncertainty in the measured laser range results from the uncertainties on flight time, atmospheric correction, and range walk. The  $1\text{-}\sigma$  precision is typically 2–3 cm in airborne surveys. The intensity of the reflected light depends on the distance to the reflecting surface (it decays at

$1/d^2$ ), orientation, and optical properties at the given wavelength (reflectance and roughness). The measurement of the direction of the beam relative to the sensor together with the flight time provides information on the position of the reflecting surface, averaged over the spot size, relative to the sensor. This information about the position of the reflecting surfaces with respect to the sensor (the 'interior orientation model') is combined with the information about orientation of the sensor determined from the navigation (the 'exterior orientation model').

The orientation of the sensor head is measured from an inertial measurement unit (IMU), and its position is measured from GPS receivers on board the aircraft. The position of these dual-frequency receivers is determined, at a sampling rate of about 5 Hz, from kinematic GPS processing relative to a set of GPS stations on the ground. The exterior orientation model therefore consists of six measurements (the roll, pitch, and yaw characterizing the pointing direction of the sensor head and its geographic coordinates in 3-D) (Figure 7).

The infrared beam can be reflected by the vegetation as well as the ground surface. Multiple reflections from the canopy and ground surface are generally detected over vegetated areas. Postprocessing is then needed to separate reflections from the ground and canopy.

The interest of airborne LiDAR for geographic mapping was explored early on (Krabill et al., 1984) and later on, as the technique became more affordable, for geomorphic and seismotectonic applications (e.g., Hudnut et al., 2002; McKean and Roering, 2004; Woolard and Colby, 2002). Much effort has been made over the last decade to collect airborne LiDAR data over areas of potential interest for tectonics and geomorphology in particular thanks to the establishment in 2003 of the National Center for Airborne Laser Mapping (<http://www.ncalm.cive.uh.edu/>). Existing surveys generally consist of shots with a density of a few points per square meter.

Altogether, the technique provides the positions of a cloud of points in 3-D and their associated intensities. The positions are measured relative to the reference frame defined by the positions assigned to the ground-based GPS stations in the kinematic GPS processing, for example, some realization of the ITRF system. Registration errors might result from both the inaccuracies of the interior and exterior geometric models and errors on the positioning of the ground-based stations. Vertical and horizontal errors (at the  $1-\sigma$  confidence level) are on the order of 5–10 and 10–25 cm, respectively. The main source of error is probably due to the uncertainty on the elevation of the sensor, which can be as large as 15 cm, due to the difficulty of modeling accurately the effect of the troposphere on kinematic GPS (Shan et al., 2007). Intensities

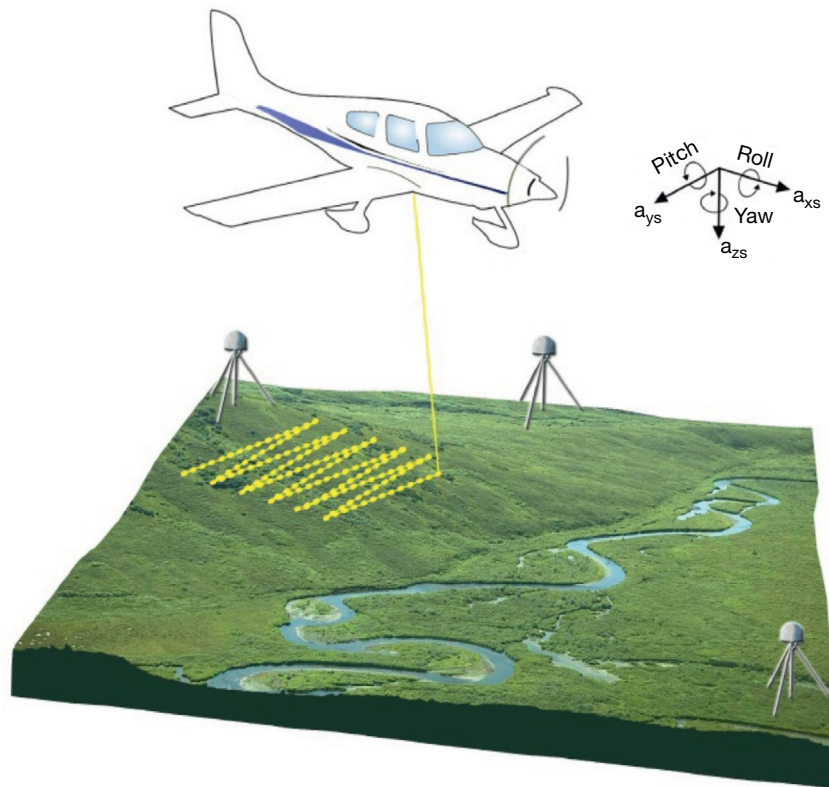


**Figure 7** Setting for an airborne LiDAR survey. An optical scanner distributes laser pulses in a zigzag pattern within a swath on the ground. The beam direction relative to sensor, the intensity of the return, and the two-way travel time required for each pulse to travel to and from a reflecting point below are recorded. The position of the sensor is determined from the positions of GPS receivers onboard the aircraft relative to a set of local GPS ground stations. The orientation (roll, pitch, and yaw) and accelerations of the sensor head ( $a_x$ ,  $a_y$ ,  $a_z$ ), measured from an inertial measurement unit, are used, along with the scanner mirror angle and measured range values, to calculate the coordinates of surface points. Modified from Carter WE, et al. (2007) Geodetic laser scanning. *Physics Today* 60 (12): 41–47.

can potentially be exploited to match datasets acquired at different times provided that the geometric attenuation of the return pulse is corrected for and that reflective properties of the ground are stationary.

### 3.13.3.2 Passive Optical Imaging

In passive imaging systems, the terrain is illuminated by the natural light emitted by the Sun or possibly reflected by the Moon. In this case, only the energy integrated over the bandwidth of the imaging system is measured since the source signal is incoherent.

A passive optical remote sensing system consists of a platform and an optical system to collect the light (telescope), eventually filter it in several spectral bands, and focus each band on detectors (Figure 8). Panchromatic systems measure at each pixel the intensity of the light collected across the visible range. In multispectral imaging, the visible to near-infrared range is filtered into a number of narrowbands. Spectral resolution generally comes at the expense of spatial resolution due to the limited sensitivity of the detectors, the limited storage capacity onboard the platform, and the bandwidth for data downloading. For geodetic applications, there is generally no advantage to using multispectral data. This is because most of the factors on geometric distortions, which limit the application, are common to all the bands and the various bands are generally correlated, so the matching accuracy does not really scale as the inverse of the square root of the number of bands as one might hope.

The platform can be an aircraft or a spacecraft. Its position and orientation are generally estimated from the navigation

information of the aircraft or from the information on the orbit and attitude of the spacecraft. This information, together with the orientation of the optical axis of the collector with respect to the platform, defines the exterior orientation model.

The detectors are charge-coupled devices (CCDs), which are organized in linear or 2-D arrays. The 'interior orientation model' defines the position of each CCD in the focal plane of the collector. Generally, the CCD spacing is adapted to the resolving power of the telescope characterized by its point spread function (PSF). Generally, the CCD spacing is about half the width of the PSF so that optical images are generally aliased (to avoid aliasing, the CCD spacing should be about 1/5 of the width of the PSF). The distance between the pixel centers projected on the ground is referred to as the GSD. In principle, this distance varies within an image depending on the topography and geometric model of the optical system. It is typically 15–30 m for Landsat images (for the bands in the visible range), 10 m for SPOT 1 to SPOT 4 panchromatic images, 2.5–5 m for SPOT 5 panchromatic images, 15 m for ASTER images, and 50 cm to 1 m for IKONOS and DigitalGlobe images. The resolution of film-based or digital aerial photographs is generally metric to submetric for standard topographic survey.

The intensity measured at a pixel of a digital image results from the optical properties, roughness, and slope orientation of the spot at the Earth's surface that is contributing to the reflected light collected by the CCD (the size of the spot is determined by the PSF) and from the filtering effect of the atmosphere.

The position of a CCD in the focal plane of the image determines the direction toward the spot on the ground that is sensed by this particular CCD. The unit vector pointing

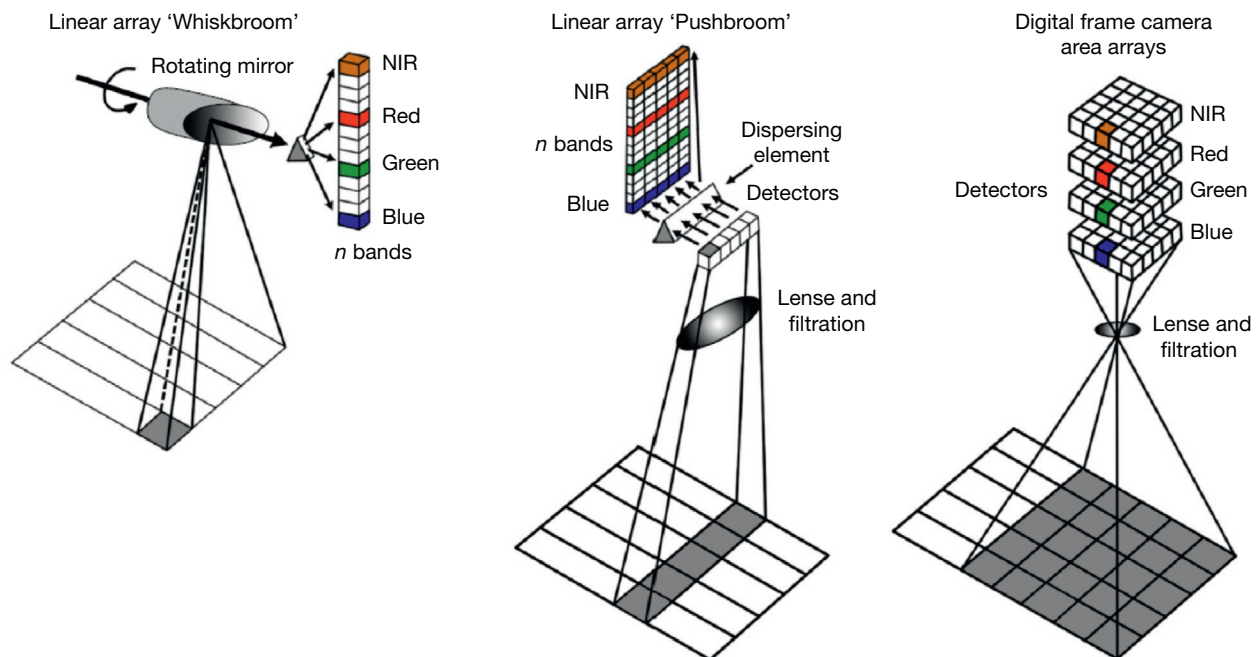


**Figure 8** Schematic representation of whiskbroom, pushbroom, and frame camera imaging systems. The gray area shows for each imaging system the pixels measured simultaneously during the image acquisition. The exterior orientation, which defines the orientation of the optical axis of the collector, is common to all these pixels. Modified from Jensen JR (2006) *Remote Sensing of the Environment: An Earth Resource Perspective*. Upper Saddle River, NJ: Prentice Hall.

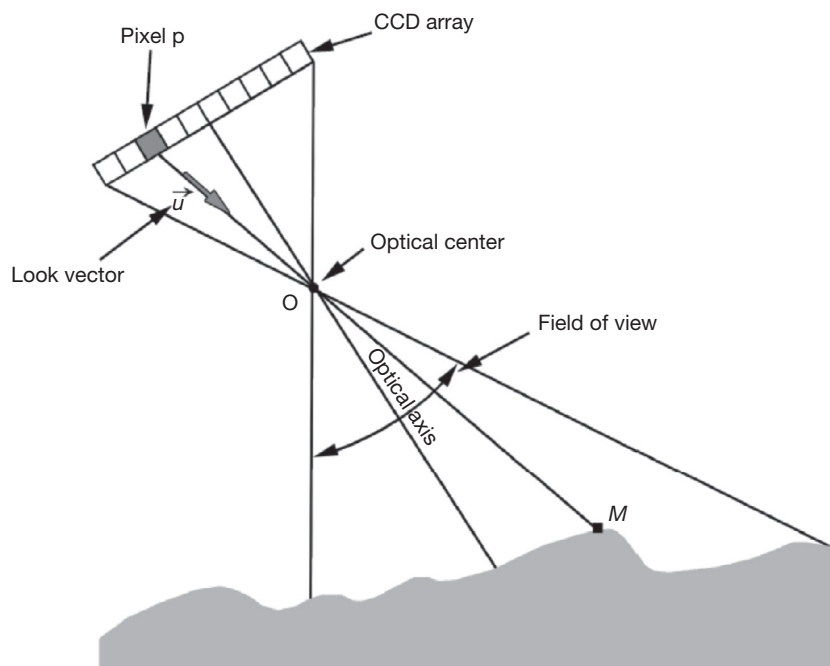


**Figure 9** The spot on the ground around point  $M$  that illuminates pixel  $p$  in the focal plane of the imaging optical telescope is determined based on classical optical geometry. Light is assumed to follow a ray connecting  $M$  and  $p$  through the optical center of the collector. The position of  $M$  relative to  $p$  depends on the interior orientation model (where the CCD corresponding to pixel  $p$  lies in the focal plane), on the position of the optical center  $O$ , and the exterior orientation model (the orientation of optical axis of the collector).

along that direction is called the look vector (Figure 9). The interior orientation model defines its orientation relative to the optical axis of the telescope.

A traditional analogue camera or a digital camera scans the light collected simultaneously within the field of view of the telescope (Figure 9). Only six parameters are necessary to characterize the exterior orientation of such a frame camera at the time of acquisition of a particular image (the geographic position in 3-D of the optical center and the roll, pitch, and yaw of the platform). The interior orientation model is in principle fixed and generally has been calibrated by the manufacturer of the sensor. The calibration model accounts for the geometric distortions due to the aberrations of the telescope, the focal length of the telescope, and the physical position of the CCD in the focal plane. In principle, only six parameters need to be determined to characterize the ground projection of any pixel on the ground. These six parameters determine uniquely, given the interior model, the position of the optical center of the image and the look vector at any point in the image (the three angles determining the orientation of the ray hitting a particular CCD or point of an analogue film). Optimization of the geometric modeling requires reducing the errors on the a priori estimate of only these six parameters. As is customary in photogrammetry, a small number of GCPs may be required as is detailed in the succeeding text.

Optical satellite remote systems take advantage of the satellite motion along its track to scan the ground. Some systems (such as Landsat launched in 1972) operate a whisk broom scanning, similar to the LiDAR scanning system described in the previous section in which only one pixel is sensed at a time.

The interior model is determined by the rotating mirror, which allows line scanning. Each pixel is acquired at a different time along the track. It results that each pixel has an independent look vector determined by the attitude of the satellite and orientation of the scanning mirror at the time of light detection. The errors on these look vectors are for a large part independent and cannot be optimized globally.

Most systems, however, operate a push broom scanning in which an entire line of the image is acquired at a given time (Figure 8). In that case, the parameters of the exterior orientation model are common to each line. This is a better situation than for the whisk broom system as the estimated exterior model can be optimized to improve the registration of the image as misregistrations errors due to the exterior orientation model are common for a line. The internal orientation (IO) model is fixed and can be improved using an in-flight calibration procedure (Leprince et al., 2008b).

### 3.13.4 Matching Techniques

#### 3.13.4.1 From 3-D to 2-D Matching

In essence, matching techniques are meant to yield at any point of a reference space (epoch  $t_1$ ) a measurement of the offset vector field that best brings into coincidence this point with a paired point in a deformed space (epoch  $t_2$ ). Matching can in principle be carried on in the 3-D physical space or the 2-D image space. In the physical space, the output will be directly a measurement of the displacement vector, provided that the Earth's surface has been advectively transported between

epochs  $t_1$  and  $t_2$ . The noise will come from the misregistration of the data. In the image space, the measured 2-D offset will reflect both stereoscopic effects and ground displacement.

The matching criterion can be based on some radiometric measurement or on the geometry of the sensed surface provided that both can be assumed to have been advected with no or negligible modifications. In case the geometries of the sensed surfaces are matched, there is an implicit assumption that there exists a scale at which the geometry has been preserved. This scale is defined by the size of the search window used in the matching procedure.

As we mentioned earlier, matching the scalar function is intrinsically an ill-posed problem. In principle, matching various bands of a multispectral image should help alleviate the ill-posedness. In practice, this is not that effective due to the strong correlations among the various bands, to the variability of the measured radiometry due to the atmosphere variability, and also to geometric and environmental modifications of the Earth's surface. For this reason, it is also necessary to regularize matching based on the radiometry, generally through matching the radiometric texture within a search window.

Let us now assume that we have a set of optical data, which were acquired at two epochs  $t_1$  and  $t_2$ , and accurate geometric models of the imaging systems. Some matching procedure is wished to measure ground displacement and to improve the co-registration of the datasets.

Let us first consider the case where the data consist of a digital rendering of the topography from LiDAR measurements or some other technique, referred to as DEM. The dataset consists of a cloud of points at the Earth's surface with their positions defined in 3-D with respect to some reference frame. The differencing of two DEMs acquired at different epochs is the simplest representation of topographic changes between the two epochs. This operation requires resampling of the dataset on a common grid. Matching the two DEMs might, however, be a more relevant measurement. This is the case if ground displacement has occurred and if surface changes due to erosion, sedimentation, or land cover modifications can be neglected. As mentioned in the preceding text, the matching procedure solves for the displacement field vector  $(d_x, d_y, d_z)$ , provided regularization assumptions, so that eqn [4] is verified as closely as possible.

Algorithms have been developed in computer vision, which allow 3-D matching of digital representations of surfaces, which include various possible regularization techniques. An example of such an algorithm is the Iterative Closest Point (ICP) technique (Besl and McKay, 1992), which has been tested recently on LiDAR data (Nissen et al., 2012; Teza et al., 2007). Details about this approach and its performance are given in the next section.

As the topography can always be parameterized in 2-D, most simply by expressing elevation as a function of geographic coordinates, the 3-D matching of optical remote sensing data of the Earth's surface can generally be transformed into a 2-D matching problem, except at locations of cliffs and overhangs. In practice, the matching problem expressed in eqn [4] can be solved in two steps as illustrated in Figure 3. First, the horizontal displacement fields,  $d_x(x,y)$  and  $d_y(x,y)$ , can be determined from a 2-D matching technique as correlation of  $h_1$  and  $h_2$  is unaffected by the shift represented by the vertical

displacement  $d_z(x,y)$  (e.g., Aryal et al., 2012; Borsa and Minster, 2012). The vertical displacement field can be obtained next by differencing the topography at epoch 2 and the topography measured at epoch 1 advected horizontally (Figure 3). Such a measurement is here also biased by registration errors.

In case of passive optical images, the geometric modeling of the imaging system provides in principle a determination of the look direction at each pixel in the image. If the topography is known independently at epochs  $t_1$  and  $t_2$ , the model can be used to produce orthoimages.

The geometric modeling can in principle be optimized and ground displacements retrieved from matching these orthoimages in 3-D. Errors in the DEMs and registration errors of the DEM relative to the images introduce spurious geometric distortions of the orthoimages. These distortions can be systematic and quite large in the common situation where the optical images have a better ground resolution than the DEM or if a DEM is available at only one epoch while the topography is known to have changed (e.g., due to advective transport). The geometric distortions are enhanced at higher ground resolution due to the topographic roughness being proportionally larger. This difficulty seriously limits the benefit of using higher-ground-resolution images to improve the resolution of ground displacement measurements. As a result, 2-D matching of orthoimages is generally not an optimal approach.

In the ideal case where stereoscopic pairs of images are available at epochs  $t_1$  and  $t_2$ , it is in principle possible to solve accurately the 3-D matching problem. In that case, the 3-D matching problem can be reformulated as a 2-D matching problem as illustrated in Figure 10. The 3-D vector can indeed be retrieved from measuring offsets between images projected on a reference surface, in practice a reference ellipsoid.

In this chapter, we refer to the offset field as the horizontal vector field retrieved from matching two 'images.' The 'image' can be the intensity measured from an optical camera or the elevation.

In the case of optical images of the same ground area taken from different view angles, the offsets measured from matching the images projected on the ellipsoid will represent stereoscopic parallax effect if the images are synchronous or a combination of stereoscopic effect and ground displacement. The most general procedure to measure displacements in 3-D with optical images is therefore measuring offsets using two pairs of stereoscopic images (Figure 10). Three independent offset fields can then be derived.

The determination of the respective contribution of stereoscopic effects and ground displacement to these offsets is then simply determined by the geometry (Figure 10). For the sake of simplicity in Figure 10, the focal points of the imaging system corresponding to all four images are supposed to be coplanar. The intersection of this plane with the reference ellipsoid defines the epipolar direction, the direction of offsets induced by stereoscopic effects. The offsets measured along the perpendicular direction would in principle be free of stereoscopic effects due to the topography and should result only from misregistration and ground displacement. In reality, the four focal points would not be coplanar so that a different epipolar direction is defined for each pair of images.

In principle, the three offset fields, which result in six independent measurements at each point on the ground, can be

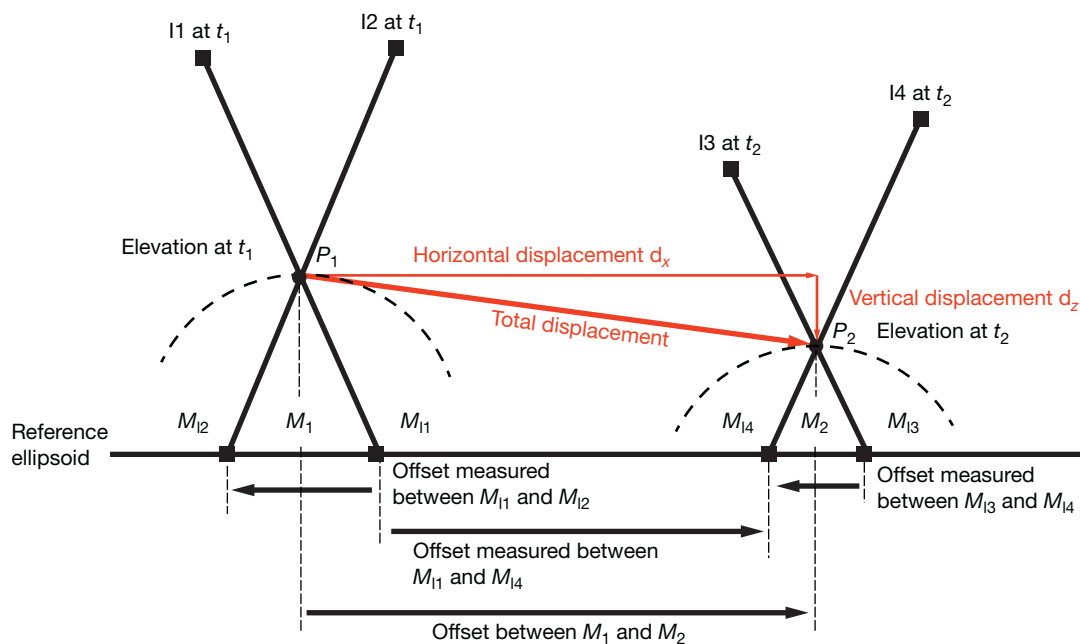


**Figure 10** Given two pairs of stereo images (I1 and I2) and (I3 and I4), respectively, acquired at times  $t_1$  and  $t_2$ , the 3-D displacement of a point P at the Earth's surface can be retrieved from the apparent offsets measured between each image pair projected onto a reference ellipsoid. Point  $P_1$ , which lies at the Earth's surface, is projected at  $M_1$  and  $M_2$ . After deformation of the Earth's surface,  $P_1$  is displaced to  $P_2$ , which will be projected at  $M_3$  and  $M_4$  from images I3 and I4. Knowing the position of the optical center of the imaging systems using the imaging system ancillary data, the 3-D position of  $P_1$  and  $P_2$  can be triangulated, from which the 3-D displacement vector from  $P_1$  to  $P_2$  can be deduced. The procedure also yields a determination of the elevation of point P at epochs  $t_1$  and  $t_2$ . If the elevations at epochs  $t_1$  and  $t_2$  are known or assumed, then the horizontal displacement is directly determined from measuring the offset between the orthoprojections  $M_1$  and  $M_2$  of point P at epochs  $t_1$  and  $t_2$ . In that case, only two images are needed.

inverted for the topography (one unknown) and the 3-D vector field (three unknowns). The problem is overdetermined because the topography should contribute to an offset along the epipolar direction at each pixel. Thus, the two components of the offset field should add redundant information on the topography. The procedure can be extended to the joint analysis of any  $n$  pairs of images following the bundle adjustment techniques described in the preceding text, which are customary in photogrammetry (Wolf and Dewitt, 2000). This is thus the most general and accurate approach with optical images. The horizontal displacement can also be determined from measuring the offset between the orthoprojections  $M_1$  and  $M_2$  of point P at the two epochs of image acquisition.

In the case of satellite images with near-vertical incidence, it is often assumed, provided that a reliable DEM is available as well, that the stereoscopic distortions due to topographic errors or to changes of elevation between the two epochs are negligible. In that case, only two images in addition to the DEM are needed. Only the horizontal displacement field can be determined. Vertical displacements cannot be determined in that case.

#### 3.13.4.2 Algorithms for 3-D Matching

Various algorithms are available, which in principle can be used to match optical remote sensing datasets directly in 3-D. The 3-D surface matching problem is a well-covered topic in computer vision, computer graphics, and medical imaging (Besl and McKay, 1992; Grenander and Miller, 1998; Zhang,

1994). The goal is to determine a nonrigid spatial transformation that maps a surface onto another surface. The difficulties result from the fact that the problem is ill-posed in general and that the sampling 'grids' of the surfaces are in general independent (requiring some sort of interpolation). Because sampling does not satisfy the Nyquist conditions in general, as the real surface has always irregularities at a scale smaller than the GSD, the interpolation is always approximate.

The ill-posedness always requires some regularization strategy. This can be achieved by a priori assumptions on the transformation. For example, it might be assumed that the transformation is approximated locally by a rigid body translation and rotation. The matching problem is regularized if the scale at which this assumption is supposed to hold is significantly larger than the sampling distance and if the surface is nonplanar, neither cylindrical nor spherical, at this scale. Another more general strategy consists in defining a regularization energy penalizing large deformations, for example, by defining an 'elastic' energy so as to penalize bending and stretching of the surface during transformation (Grenander and Miller, 1998). Different algorithms are available, which might be adapted to geodetic optical remote sensing.

For example, the ICP algorithms (Besl and McKay, 1992) were successfully applied to reconstruct the displacement field of a slow-moving rockslide using terrestrial LiDAR data (Oppikofer et al., 2009; Teza et al., 2007). Nissen et al. (2012) had, for example, evaluated the performance of the ICP when applied to airborne LiDAR data. They found the

algorithm based on the point-to-plane metric of [Chen and Medioni \(1992\)](#) to perform best, so we briefly describe this particular algorithm.

For each point in the first dataset, the closest point in the second dataset is determined. For all points within a prescribed window, the rigid body transformation is determined so as to minimize the squared sum of the distances,  $l_i$ , between each point  $P_i$  of the second dataset and the tangential plane at its paired point  $M_i$  in the first dataset ([Figure 11](#)):

$$l_i = \vec{n}_i \cdot \overrightarrow{\phi(M_i)P_i} \quad [5]$$

The first iteration yields the rigid body transformation,  $\phi_1$ , that minimizes the quantity  $\sum_i l_i^2$ . The process is iterated until some minimum is reached and the local transformation is the composition of the transformations determined at each iteration. This algorithm is very effective, converges better, and is less susceptible to yielding a local minimum than the original closest point metric ([Low and Lastra, 2003](#)).

[Nissen et al. \(2012\)](#) carried on synthetic tests in which they applied a known displacement to a subset of the B4 dataset, which was acquired along the major faults of the San Andreas Fault system in central and southern California ([Bevis et al., 2005](#)). The dataset consists of a point cloud with a sampling rate of about 2 points  $\text{m}^{-2}$  (mean GSD of 0.7 m) with nominal uncertainties of 25 cm on horizontal positions and 6 cm on elevation. Using sliding windows of  $100 \times 100 \text{ m}^2$ , within which the transformation is approximated by a single rigid body transformation, they were able to recover the imposed displacements with  $1\text{-}\sigma$  uncertainties of 13 and 15 cm for E and N displacements and of 4 cm for vertical displacements. In this particular example, the uncertainty on horizontal displacement is estimated to be about 1/5 of the GSD and the uncertainty on vertical displacement, which is on the order of the nominal uncertainty on elevation measurements. This particular test was carried out by applying a known displacement field to the original LiDAR dataset. The advantage of this approach

is that it does not require any explicit resampling of the original dataset. One major inconvenience is that there is no proof that the algorithm converges. The algorithm is very sensitive to noise because the determination of the normal vectors is very sensitive to horizontal registration errors and elevation errors. It can very easily get trapped in local minima especially when ground displacements or registration errors are in excess of the GSD. So even in the case of terrestrial LiDAR data, for which co-registration can be achieved with a better accuracy than with airborne data, ICP techniques do not perform better than the 2-step procedure involving first the determination of horizontal offsets from a 2-D matching algorithm ([Daehne and Corsini, 2012](#)).

### 3.13.4.3 Algorithms for 2-D Matching

This section presents an overview of different matching methods commonly used to measure the deformation between images of the same scene. The literature on image matching is abundant. The reader is referred, for example, to reviews by [Zitova and Flusser \(2003\)](#) or [Scharstein and Szeliski \(2002\)](#) (see also the associate website <http://vision.middlebury.edu/stereo/>). Here, we only mention those techniques that have already proven suitable to remote sensing applications for Earth sciences. In the context of this review, image matching is used to measure the disparity field that best morphs a slave onto a master image.

#### 3.13.4.3.1 Homogeneous rotation and heterogeneous translation

Any transformation of a continuous field can be locally approximated by a homogenous transformation, that is, the combination of a rigid body rotation and a translation. In geodetic imaging from remote sensing data, it is generally admitted that the rotation component is homogeneous so that strain results dominantly from spatial variations of the

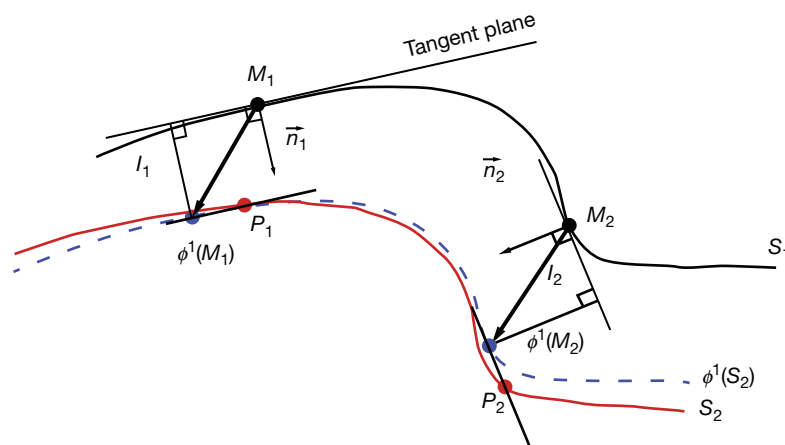


**Figure 11** Matching of 3-D from the Iterative Closest Point technique, using the plane to point error metric ([Low and Lastra, 2003](#)). We consider that the surface has been sampled at two epochs  $t_1$  and  $t_2$ . For each point  $M_i$  in the first dataset, the closest point  $P_i$  in second dataset is determined. For all points within a prescribed domain, the rigid body transformation  $\phi$  is determined so as to minimize the squared sum of the distances,  $l_i$ , between each point  $P_i$  of the second dataset and the tangential plane at its paired point  $M_i$  in the first dataset (eqn [5]). So, the first iteration yields the rigid body transformation,  $\phi_1$ , that minimizes the quantity  $\sum_i l_i^2$ . The process is then iterated until some minimum is reached. The local transformation is the composition of the transformations determined at each iteration.

translation component. As a result, the common practice is to first determine and correct for the homogeneous rotation component. This is generally achieved through the orthorectification procedure as, in most Earth sciences applications, local residual rotations are generally small. The next step is to determine the heterogeneous translation component. Any heterogeneous translation, provided that it is a continuous differentiable functional, can be locally approximated by a homogeneous translation. We therefore define matching as finding a globally nonrigid deformation between data, but that is approximated locally by a rigid translation. We will see that these assumptions and approximations hold for the applications reviewed here.

### 3.13.4.3.2 Optical flow

Optical flow methods were introduced by Horn and Schunck (1980) and Lucas and Kanade (1981), and many different implementations have been proposed since (e.g., Sun et al., 2010). The basic idea behind these methods is that the radiometric differences between the master and slave images are only due to plane deformation of the scene. This assumes that other factors of radiometric changes due to the imaging system and scene illumination have stayed unchanged or corrected for.

Let us consider the intensity  $i_1$  (respectively  $i_2$ ) measured a pixel location  $X, Y$  in master image 1 (respectively slave image 2). One may then write

$$i_2(X, Y) = i_1(X - d_x, Y - d_y) \quad [6a]$$

where  $(d_x, d_y)$  is the disparity vector field in the image space describing the heterogeneous translational transformation, which maps image 1 onto image 2. For small offsets, this equation can be approximated from its Taylor expansion to first order yielding

$$i_2(X, Y) - i_1(X, Y) \approx -d_x(X, Y) \frac{\partial i_1}{\partial X}(X, Y) - d_y(X, Y) \frac{\partial i_1}{\partial Y}(X, Y) \quad [6b]$$

This equation shows that the deformation between two images is encoded in the image's brightness differences, just like eqn [4] that shows that horizontal advection of the ground surface is encoded in elevation changes.

This equation yields an ill-posed problem, as only the component of the offset vector field parallel to the image brightness gradient  $(\partial i_1 / \partial X(X, Y), \partial i_1 / \partial Y(X, Y))$  can be determined. The problem can be regularized if solved at the scale of a local window, assuming that the disparity field is constant over a certain area (Lucas and Kanade, 1981) or using a global regularization approach (Horn and Schunck, 1980).

Under ideal conditions, the performance should only be limited by the radiometric noise. So, in theory, disparities might be measured with an accuracy better than 1/100 of the pixel size with 8-bit images and relatively small sliding window size (say  $11 \times 11$  pixels) (Sabater et al., 2012). The technique has proven efficient and is adapted to measure strain from photogrammetry in laboratory analogue experiments (Bernard et al., 2007). This approach fails if disparities exceed about 1 pixel, as in this case, the Taylor approximation is not valid anymore. This problem occurs, for example, when the

two images have different view angles and the surface roughness at the pixel scale is large (e.g., with high-resolution images of urban areas). This approximation also fails along a fault trace as the displacement field is locally discontinuous. The technique is very sensitive to variations of brightness not due to deformation of the scene. Optical flow methods have been extended to higher-order deformations, in particular, to the measurement of locally affine deformations and also to account for slight contrast variations (Broxton et al., 2009; Sabater et al., 2012). However, optical flow methods are often not robust enough to the strong illumination differences encountered in multitemporal remote sensing imagery, and they are therefore seldom used for geodetic imaging.

### 3.13.4.3.3 Statistical correlation

The idea behind statistical correlation is to use the Pearson's statistical correlation coefficient between an image patch taken in the master image and a multitude of neighboring candidate patches in the slave image (e.g., Barnea and Silverma, 1972). This technique is the basis for the particle imaging velocimetry method used to track fluid flow in fluid mechanics (Dudderar and Simpkins, 1977; Willert and Gharib, 1991) or sample deformation in experimental mechanical engineering (Hild and Roux, 2006). The technique has been used in Earth sciences, for example, to track glaciers, earthflows, and oceanic currents (Aryal et al., 2012; Debella-Gilo and Kaab, 2011; Marcello et al., 2008; Scambos et al., 1992).

The matching position of the two patches, hence the displacement between the patches, is found when the cross correlation attains its maximum. In order to take into account contrast and brightness variations, the cross correlation coefficient is normalized:

$$\rho(X, Y) = \frac{\sum_{X, Y} (i_2(X, Y) - \bar{i}_2) (i_1(X - d_x, Y - d_y) - \bar{i}_1)}{\sqrt{\left[ \sum_{X, Y} (i_2(X, Y) - \bar{i}_2) \right]^2 \left[ \sum_{X, Y} (i_1(X, Y) - \bar{i}_1) \right]^2}} \quad [7]$$

In practice, this simple formulation has been found to be one of the most robust against noise, affine changes of illumination, and temporal changes between images, and it is used in most implementations of image matching for remote sensing data (Marcello et al., 2008). There also exist a wide range of variations of correlation algorithms, with most variations depending on whether the correlation score is invariant by linear contrast changes and whether it uses an L1 or L2 norm (Zabih and Woodfill, 1994).

In a discrete correlation scheme, the slave correlation window can be seen as a moving window, moving with a step of 1 pixel at a time, therefore only sampling potential translation between master and slave images with integer displacements. Subpixel approximation is usually achieved by interpolating, or approximating, the maximum of the correlation peak with a quadratic or a Gaussian function (e.g., Debella-Gilo and Kaab, 2012). Although interpolation of the correlation maximum improves the correlation accuracy, it is, however, biased, and depending on the specific implementation, accuracy is often limited to about 1/5–1/4 of the pixel size. This bias can be

understood if we consider the correlation function, which involves the product of the master and slave images. Therefore, the correlation function exhibits a frequency support that is twice as large as the one of the images. Therefore, in order to avoid aliasing in the correlation function, one should in principle upsample both master and slave images by a factor of two. In practice, due to memory constraints, this upsampling is rarely implemented, leading to small biases. Another possible alternative to remove the subpixel bias is to iterate the correlation scheme with warping of the slave image between iterations. As it can be shown that the aliasing bias is always a fraction of the quantity to be measured, iterating the measurement will lead to a negligible bias. In practice, one iteration removes enough bias to allow measurement accuracy better than 1/10 of the pixel size but has an increased computational cost and assuming the warping does not introduce additional artifacts.

### 3.13.4.3.4 Phase correlation

Phase correlation methods take advantage of the Fourier shift property, whereby a translation in the image domain is equivalent to a phase shift in the Fourier domain.

Accordingly, the Fourier transform of eqn [6a] yields

$$\tilde{i}_2(\omega_X, \omega_Y) = \tilde{i}_1(\omega_X, \omega_Y) e^{-j(d_X \omega_X + d_Y \omega_Y)} \quad [8]$$

The local translation  $(d_X, d_Y)$  can therefore be retrieved using the inverse Fourier transform (noted  $\mathbb{F}^{-1}$ ) of the images cross spectrum, such that

$$\delta(X - d_X, Y - d_Y) = \mathbb{F}^{-1} \left( \frac{\tilde{i}_1(\omega_X, \omega_Y) \tilde{i}_1^*(\omega_X, \omega_Y)}{|\tilde{i}_1(\omega_X, \omega_Y) \tilde{i}_1^*(\omega_X, \omega_Y)|} \right) \quad [9]$$

When the displacement  $(d_X, d_Y)$  is not an integer number of pixels, an interpolation problem arises, and proper peak interpolation often requires iterating the correlation with image resampling (Vadon and Massonnet, 2000).

Another solution to avoid interpolation problems is to directly solve for the displacement  $dx$  in the Fourier domain via an inverse problem. Indeed, one can solve for  $(d_X, d_Y)$  that minimizes

$$\int \left[ \frac{\tilde{i}_1(\omega_X, \omega_Y) \tilde{i}_2^*(\omega_X, \omega_Y)}{|\tilde{i}_1(\omega_X, \omega_Y) \tilde{i}_2^*(\omega_X, \omega_Y)|} - e^{j(d_X \omega_X + d_Y \omega_Y)} \right]^2 d\omega \quad [10]$$

This nonlinear minimization problem can be efficiently solved using linearization if initialized close to the solution given by the inverse Fourier transform from the preceding text.

Comparing with a statistical correlation, phase correlation methods are usually computationally more efficient taking advantage of the FFT algorithm, and since no aliasing problem occurs in this formulation, it has the potential to be highly accurate, often providing results with accuracy on the order of 1/20–1/10 of the pixel size using small window sizes (e.g.,  $32 \times 32$  pixels). The normalization in the Fourier domain has also shown to be very robust against illumination changes and even against sharp contrast differences. Overall, practice has shown that phase correlation has the potential to be more

accurate and less sensitive to contrast or shadow changes than statistical methods. They, however, tend to be more sensitive to noise, and correlation windows need to be larger than  $16 \times 16$  pixels, which reduces the spatial resolution of the displacement field retrieved. This approach has proven efficient to measure coseismic deformation from satellite optical images, glacier flows, and earthflows (Leprince et al., 2007, 2008a; Van Puymbroeck et al., 2000).

### 3.13.4.3.5 Regularized solutions and large displacements

Particularly in the context of topography extraction or in the context of 3-D measurement of displacement fields, large pixel offsets may need to be measured. To lower the complexity of the matching algorithm by reducing its search space, it is customary to proceed in a multiscale fashion, where master and slave images are downsampled by a factor that allows a reasonable complexity for the matching algorithm (e.g., Pierrot-Deseilligny and Paparoditis, 2006). The offset field found at the coarser scales is then upsampled to higher scales, where the slave image at higher scales is warped according to the offset field measured at lower scales. Iteratively, only a differential offset field needs to be computed at each scale, lowering the complexity of the algorithm.

This multiscale approach also allows matching deformations that can depart significantly from a local translation. Indeed in this context, the condition to be met for good matching is only that the deformation field between successive scales be locally approximated by a translation.

One major drawback of multiscale schemes is that errors can easily be propagated between scales. The matching algorithm must therefore be augmented with a regularization term to ensure that spurious matches do not occur and to ensure that every point at every scale is assigned a likely match, to be propagated. As a result, missing matches cannot be tolerated within a multiscale approach.

The state-of-the-art regularization that is the most widely used at the time this paper is being written is the regularization on the L1 norm on the gradient of the offset field, solved by Semi-Global Matching (Hirschmuller, 2005; Hirschmuller and Scharstein, 2009). This approach offers a good compromise between the maximization of the correlation coefficient and the smoothness of the offset field. Such regularization technique is usually applied to image-based matching functions such as the normalized cross correlation presented in the preceding text (Pierrot-Deseilligny and Paparoditis, 2006), entropy, or census matching.

## 3.13.5 Geometric Modeling and Processing of Passive Optical Images

### 3.13.5.1 The Orthorectification

The orthorectification is the process that projects an image on the topography surface by assigning absolute geolocation coordinates  $(x, y, z)$  to each image pixel. An orthorectified image, or orthoimage, is therefore free of stereoscopic effects, since it simulates an image as if each pixel had been acquired with a viewing angle normal to the projection datum. To achieve this result, the orthorectification is composed of two processing

steps: (1) computing the mapping between the image pixel coordinates and the ground coordinates and (2) resampling of the image according to this projection mapping.

### 3.13.5.1.1 The orthorectification mapping

Generating the orthorectification mapping is solving a ray-tracing problem, which is a geometric problem. It requires the knowledge of the camera geometry so that the direction of light rays hitting every pixel in the image can be established. Given a camera model, its position, and its orientation in space, it is then possible to determine which points on the ground reflected the sunlight that hits a particular pixel using the reverse light propagation principle. Simple models usually assume a standard pinhole camera model with light propagating along straight lines in the atmosphere. More complex models will include the camera optical and sensor distortions, the variation of the atmospheric refraction index, and the relative speed of the camera with the speed of light to determine precise orthorectification mappings. For instance, a simple model for a push broom sensor (Figure 9) can be given by the following equation (Leprince et al., 2007):

$$M(p) = O(t) + \lambda \cdot T(t) \cdot R(t) \cdot \vec{u}(p) \quad [11]$$

where  $M(p)$  is the ground point seen by the pixel of coordinates  $p(X, Y)$ ,  $t$  is the time at which the pixel  $p$  was acquired,  $O$  is the location of the optical center when the pixel  $p$  was acquired,  $\vec{u}(p)$  is the reverse direction of the light ray for the pixel  $p$ ,  $R(t)$  is the 3-D rotation matrix recording the 3-D rotation of the camera in space at time  $t$ ,  $T(t)$  is the system reference change matrix from the camera (orbital) to the terrestrial reference system, and  $\lambda$  is the distance between the optical center and the object seen by the pixel  $p$ .

Parameters describing the camera, that is, the set of vectors  $u$ , are defining the internal orientation (IO) model of the system, and the parameters describing the camera positions and orientations in space, that is,  $O$  and  $R$ , are defining the external orientation (EO) model of the system.

Knowledge of a fine model of the topography is also needed to determine  $\lambda$ , as  $M$  lies at the intersection between the imaging pointing vector  $T \times R \times u$  and the topographic surface.

### 3.13.5.1.2 Resampling the image

Producing an orthoimage implies producing an image that is regularly sampled in a given georeferenced system, so it can be displayed. However, because of the topography variations and changes in camera viewing angle, the mapping associating the pixel coordinates to the ground coordinates is often highly irregular (Figure 12). To avoid solving a complex irregular resampling problem, it is often convenient to assume that the sensor delivers a regularly sampled image. This assumption can be considered exact for frame cameras as the sensor is composed of a unique and flat focal plane, but it is only a local approximation for push broom sensors that exhibit varying attitude over time, with the quality of this assumption depending on the attitude stability of the sensor in time. Therefore, instead of attributing ground coordinates to each image pixel, we preferentially solve the inverse problem, which attributes

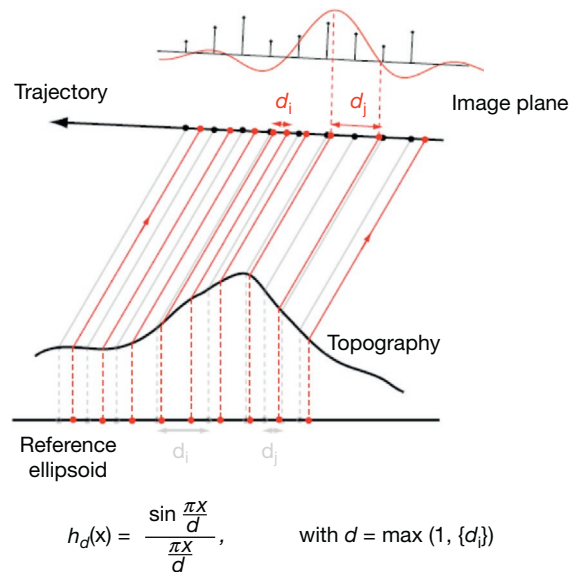


**Figure 12** Due to the topography, the orthoprojection of the ground spots sensed by regularly spaced CCD is irregularly spaced. Instead of attributing ground coordinates to each image pixel, we solve the inverse problem, which attributes pixel coordinates to every point of the orthorectification grid (Leprince et al., 2007). The intensity at those points can be estimated with well-known resampling kernels (ideally a sinc function) in the image space.

pixel coordinates to every point of the orthorectification grid (Leprince et al., 2007).

This method allows the use of more traditional, and much simpler, resampling methods with well-known resampling kernels. When the sampling density of the orthoimage is similar, or less than, the raw acquisition, the image resampling simply turns to an interpolation problem, where the raw image simply needs to be interpolated at the pixel coordinates given by the orthorectification mapping. One needs to be careful when the sampling density of the orthoimage is less than the sampling density of the raw image. In this case, the resampling kernel can be approximated by the interpolation kernel, dilated by the change in sampling density (Figure 13). Intuitively, the change in the sampling density can be seen as the local ratio between the raw image sampling and the orthogrid sampling. This operation can be seen as a local aggregate of the raw image pixels whenever the orthogrid resolution is coarser than the raw image resolution. Formally, the local dilation of the resampling kernel can be represented as the Jacobian of the orthorectification mapping, and the sampling density variation is represented by the absolute value of its determinant (Leprince et al., 2010).

How to adapt the resampling kernel to the orthomapping applies to any resampling kernels. In practice, the choice of a particular resampling kernel will depend on the constraints of the application at hand, with typically a compromise between accuracy and processing time (or algorithmic complexity). For geodetic applications, it is recommended to select a resampling kernel belonging to the cardinal-sine family. The cardinal-sine function (sinc) is the theoretically exact sampling kernel for regularly spaced samples.

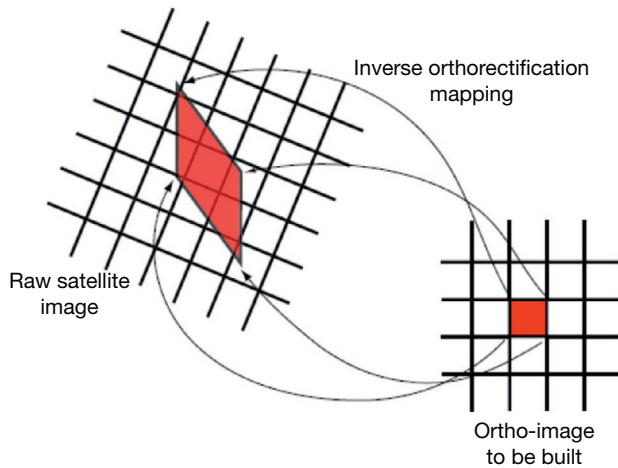


**Figure 13** The resampling kernel used to calculate the orthoimage needs to be adjusted to the distortions induced by the topography. Formally, the local dilation of the resampling kernel can be represented as the Jacobian of the orthorectification mapping, and the sampling density variation is represented by the absolute value of its determinant. Leprince S, et al. (2010) Rigorous adaptive resampling for high resolution image warping. In: *IGARSS: Proceedings of the 2010 IEEE International Geoscience and Remote Sensing Symposium*, pp. 1943–1946.

$$h_d(X) = \frac{\sin \frac{\pi x}{d}}{\frac{\pi x}{d}}, \quad \text{with } d = \max(1, \{d_i\})$$

It exhibits low phase distortion and therefore introduces less subpixel biases in the orthoimage (Van Puymbroeck et al., 2000). Whenever the geometric accuracy of the orthoimage is important, truncated or weighted sinc resampling kernels are usually recommended.

### 3.13.5.2 Bundle Adjustment

The orthorectification mapping relies on the precise knowledge of the parameters defining the interior and exterior orientations of the optical system. Interior orientation parameters are usually determined through optical bench calibration, and EO parameters are usually recorded during the image acquisition using GPS and IMU devices. Unfortunately, these parameters (in particular for the exterior orientation) are often not known with enough accuracy to provide geodetic measurements from optical images. They are therefore usually refined using GCP. GCPs are recorded during ground surveys, and they associate ground coordinates to recognizable features in the image. External parameters are then optimized such that, for a given pixel coordinates in a GCP, the distance between the ground coordinates predicted by the orthomapping for this given pixel and the actual GCP ground coordinate is minimum.

When presented with a system composed of frame cameras, the positions in space and orientations of the cameras are optimized, leading to six external parameters to be optimized per image. When the system is composed of scanning devices such as push broom sensors, the exterior orientations are composed of varying positions and orientation angles in time. In this case, it is customary to model the error on the positions

and orientation angles as second-order polynomials varying in time, leading to 18 EO parameters to be optimized per image.

When several images of the same area are available, corresponding pairs of pixels between images, called tie points, can be selected. This selection is usually automatic using feature matching algorithms (e.g., SIFT and Forstner operator) (Forstner and Gulich, 1987; Lowe, 2004), and false matches are rejected using robust statistics (RANSAC) (Beckouche et al., 2011; Fischler and Bolles, 1981). However, visual verification of tie points is still customary in practical applications.

Here again, the viewing parameters of the imaging systems can be optimized thanks to the tie points. Formally, the objective is to find the sets of EO parameters such that the rays issued from the tie points intersect as closely as possible. However, in the absence of absolute GCPs, the solution of this system will not be well constrained and the optimization of the parameters is only relative. For instance, it is easy to see that in the absence of absolute GCPs, the optimization of the tie points could lead to a system that could be arbitrarily translated and scaled in space. Therefore, in the absence of GCPs, additional a priori information on the maximum deviation of the given exterior parameters is required. Whenever possible, it is usually best to jointly optimize a set of tie points and GCPs to insure precise absolute location of all images. This global optimization that consists of sets of images is called the bundle adjustment. This is a standard approach in photogrammetry when DEMs are produced from various sets of overlapping images (Wolf and Dewitt, 2000).

In our experience, performing a bundle adjustment is always necessary to deliver absolute geodetic measurements with an optical imaging system. The accuracy of the rectified imagery depends on the accuracy of the bundle adjustment, which itself depends not only on the accuracy of the tie points and GCPs provided but also on the quality of the sensor modeling. From a user's perspective, providing tie points and GCPs with subpixel accuracy (with accuracy better than the image pixel size) is always necessary to ensure a near-geodetic quality of the measurements.

### 3.13.5.3 Stereo Imaging

Stereoscopic imaging refers to the possibility of extracting the 3-D shape of a surface imaged using at least two images of the same scene from different viewpoints. A bundle adjustment of the images is often required to provide digital surface models with acceptable accuracy. Assuming that light travels along straight lines, the concept of stereo imaging can be described as solving a simple geometric problem (Figure 9). From the camera interior orientation, we know how to model the light rays hitting each pixel of the image. From the exterior orientation, we know the location in space of the optical centers and orientation of the cameras. Now, if we add another function to the system that provides matching pairs of pixels between the different images, it is possible to find the intersection of light rays between the corresponding pixels of the different images. The intersection of light rays therefore defines the location of the surface that reflected the light to the sensor. Repeated over the common pixels between the set of images, it becomes possible to reconstruct the imaged terrain in three dimensions.

It is clear that the higher the angle between intersecting rays (referred to as the stereoscopic, convergence, or parallax angle),

the better constrained the location of the intersection will be. However, large convergence angles are also likely to produce occlusions, where parts of the scene will be hidden behind high slopes. In addition, the matching algorithms tend to have lower failure rates when images are acquired with lower convergence angles, which minimize the relative distortion between images. In practice, it is preferable to keep the convergence angle between  $10^\circ$  and  $45^\circ$ , with the lower angles being used in areas with the highest topographic slopes to limit occlusions.

In stereo imaging, it is assumed that stereo images are acquired simultaneously or at least that potential changes between acquisitions can be neglected. In a multitemporal stereo set up, we add another step, where we can associate pixels from images acquired at different times. From a stereo pair at a given time, we determine the 3-D coordinates of the surface, we determine where this point on the surface is in the other stereo pairs, and the other stereo pairs are used to give the 3-D coordinates of the given point, at another time, hence producing a 3-D displacement vector (Figure 10).

#### 3.13.5.4 Processing Flowchart

When one uses only two images bracketing a deformation event, only the horizontal displacement field can be recovered. If the two images were taken from exactly the same viewpoint, displacement of the ground parallel to the image plane (i.e., horizontal) would be the only cause of distortion in principle. The topography is, however, needed in order to register the measured displacement through orthorectification of the two images.

This is never the case in practice. At best, the two images have close view angles but the look angle vectors are variable so that stereoscopic effects are always present. In principle, one would need to know the topography at the two epochs. The offsets measured between the two orthorectified images would then represent horizontal displacement in the geographic coordinate system defined by the GCP used for registration. In case

of two images with close and near-vertical incidence view angles, the distortions are small, and it is then valid to use even a coarse DEM and neglect topographic changes. As we will see in the examples later, this assumption is often challenged. Images acquired within a few degrees of nadir looking help mitigate this constraint.

Within this setup, the analysis of the images can be performed either in the ground geometry or in the image geometry. Performed in the image geometry, it would mean that the slave image would be projected in the master image geometry using the DEM to suppress stereoscopic parallax, and the disparity map, in the master geometry, would have to be orthorectified according to the master geometry in order to produce a ground displacement map.

Performed in the ground geometry, the master and slave images are both orthorectified, and the disparity map is computed between the orthomaster and the orthoslave images. The main advantage is that the disparity map therefore directly produces the ground displacement map, without the need to further resample the disparity.

We generally prefer using the ground geometry, as is the case in the examples reviewed in the succeeding text, because the implementation is less dependent on the modeling of the sensors, making it easier to mix different types of imagery together; it also makes the different blocks of the processing chain more independent, allowing the use of potentially different software solutions along the processing chain; and it also avoids the delicate task of resampling the disparity field. However, the reader should be aware that disparity fields computed in the ground geometry may be slightly noisier than disparity fields computed in image geometry, because images are subject to less manipulation when left in image geometry.

The processing in ground geometry typically involves the following steps (see flowchart of Figure 14):

- Select tie points and GCP between the master image and the topography model.

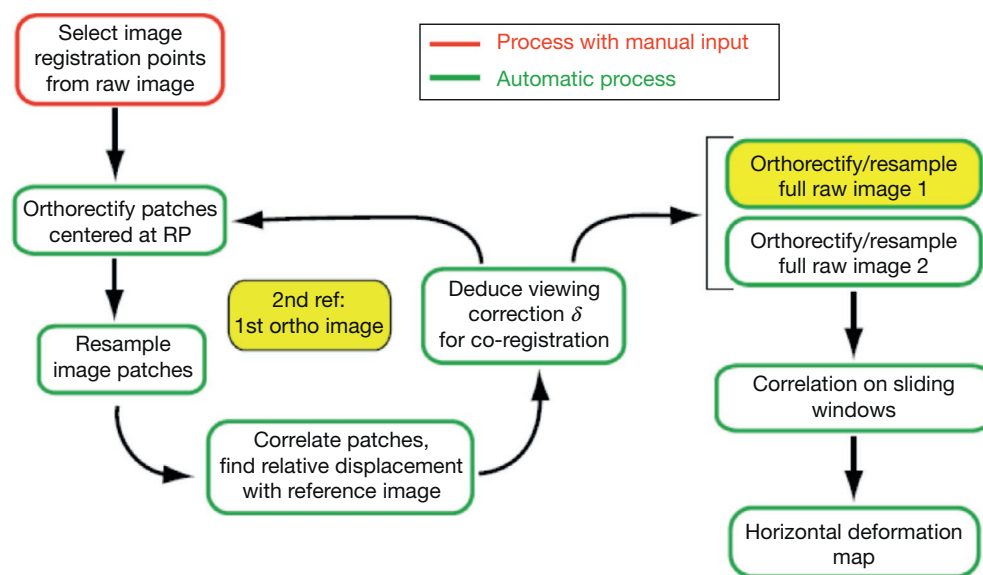


Figure 14 Flowchart for the measurements of horizontal displacements from two optical images and a DEM. See text for details.

- Optimize the exterior orientation parameters of the master image according to the GCP selected and orthorectify the master image.
- Select tie points and GCP between the slave image and the orthomaster image, in areas of stable ground.
- Optimize the exterior orientation parameters of the slave image according to the GCP selected and orthorectify the slave image.
- Perform dense image matching between the orthomaster and orthoslave images to produce the displacement field.

When measuring 3-D displacements, it is assumed, by definition, that the DEM available is not sufficient to describe the ground motion. In this case, if a DEM is available, it will be used in the process as a seed to speed up computation by reducing the search range of the stereo processing.

As for the estimation of 2-D displacement fields, the estimation of 3-D displacement fields can be formulated in image geometry or in ground geometry. However, even in ground geometry, the disparity field recovered may need to be resampled because the large incidence angles commonly used for 3-D processing may not allow the derivation of a proper orthomaster image.

A typical processing chain for the estimation of 3-D ground motion can be the following:

- Select tie points between all stereo pairs.
- Select tie points between the multitemporal pairs in areas of stable ground only.
- Perform a bundle adjustment of all data.
- Orthorectify all images on a seed DEM.
- Perform image matching between orthoimages for stereo pairs and for multitemporal pairs.
- Triangulation of stereo pairs produces 3-D points.
- Matching of the multitemporal pairs associates 3-D points before and after the event, thereby producing 3-D ground displacement vectors.

### 3.13.5.5 Performance, Artifacts, and Limitations

Most artifacts and limitations to the measurement of ground deformation from optical imagery can be grouped in a small number of categories, which are geometric errors, topographic errors, improper placement of tie points/GCP, shadowing effects, and poor image matching. We point to the figures illustrating these various effects, which are commented later on in the text (chronological ordering of figures is not respected here). Quantitative estimates of these errors are provided when these examples are reviewed.

- Geometric errors

Uncertainties in the geometry of the imaging sensor will introduce biases in the ground deformation measured. Common sources are

- jitter/attitude artifacts due to push broom motion (unmodeled platform attitude variations) (Figures 21 and 22),
- CCD misalignment or miscalibration in the focal plane (Figure 19),
- scanning artifacts (when using film archives) (Figure 20(b)),

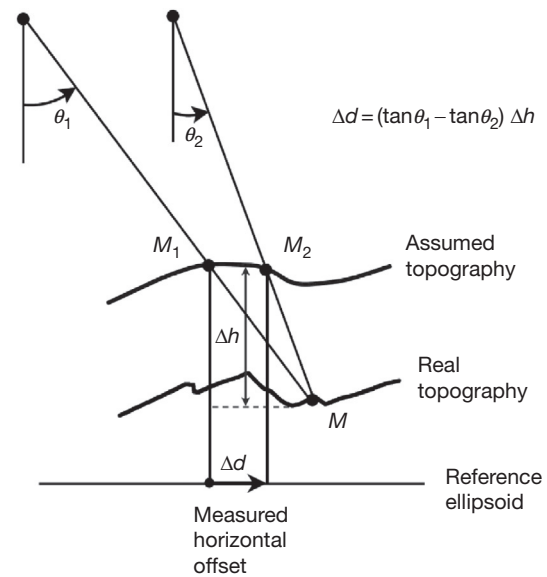


**Figure 15** Sketch illustrating artifacts due to topographic errors in the case where surface displacements are measured from matching optical images orthorectified based on a preexisting DEM. Any DEM is a first-order approximation of the real topography. It follows that the position in the images 1 and 2 of a particular point  $M$  on the ground is determined by the real topography and the look angle vectors. If the view angles,  $\theta_1$  and  $\theta_2$ , are different, the orthorectification procedure will yield positions  $M_1$  and  $M_2$ , which are biased due to the difference between the real and assumed topographies. An apparent horizontal displacement will result. This bias will in particular be important with images with high incidence view angles, when the topography is rugged. The topographic error can be due to the uncertainty on the determination of the topography and to the advective transport of the topography.

- unknown film distortions (when using film archives) (Figure 20(a)).
- Topographic errors
  - If only two images bracketing an event are available, then it is assumed that the DEM should properly account for the height modeling. If the DEM resolution is too coarse with respect to the image resolution, a bias will be introduced in the ground deformation measurement, which depends on the difference between the incidence angles of the two images (Figure 15).
  - In general, topographic errors occur when as follows:
    - The DEM has insufficient horizontal or vertical resolution (Figure 17).
    - The topography between acquisitions has changed and a single DEM is used (Figure 28).
    - Images are not well registered to the DEM.
- Location of GCPs
  - All the processes require optimization of the viewing geometry of the sensor (a least exterior orientation via bundle adjustment), and optimization requires GCP and tie points between images. One has to be careful to select these points on stable ground, or the bundle will try to absorb the ground deformation into the sensor modeling. Particular difficulties can arise when the swath of the imaging sensor is limited (e.g., airborne sensors) and when

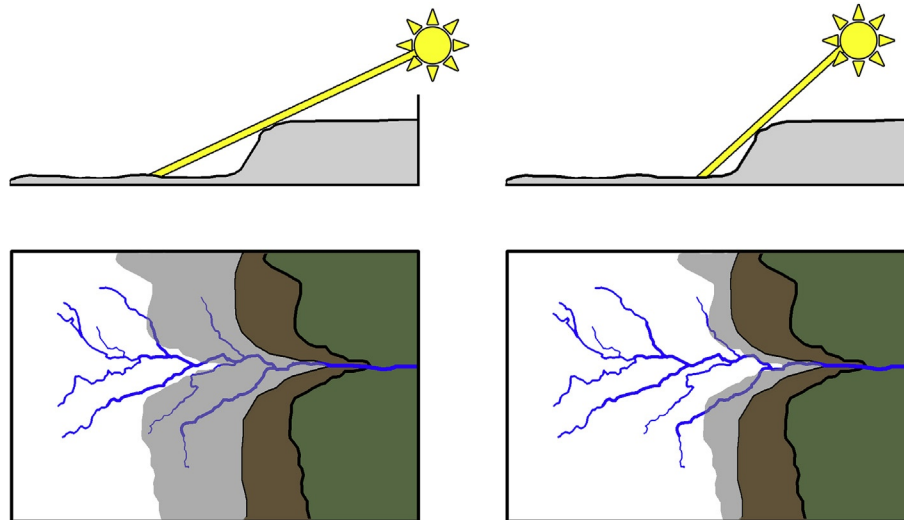


**Figure 16** Sketch illustrating artifacts due to shadows. Generally, two nonsynchronous images of a same scene will show different shadows due to the difference of sun azimuth and sun elevation. Strong cast shadows may overwhelm ground features. If the texture of the image at the scale of the sliding window used for 2-D matching is dominated by such topographic shadows, then the image matching algorithm will likely track the moving shadows rather than the moving ground.

ground deformation is present in most of the field of view. When tie points/GCP is taken on moving grounds, long-wavelength biases are usually introduced in the deformation maps (Figure 25).

- Shadowing effects

Although most Earth-observing satellites are placed on Sun-synchronous orbits (the satellite always sees a given point at the same local time), seasonal variations still induce changes in the orientation and length of shadows during the year. Problems may arise when strong cast shadows are present, as their contrast may overwhelm the contrast of the ground objects (Figure 16). If the texture of the image at the scale of the sliding window is dominated by topographic shadows, then the image matching algorithm will likely track the moving shadows rather than the moving ground, thereby introducing a bias (Figure 17). If using a matching algorithm with contrast invariance features, diffused shadows are usually not a problem.

- Image matching failure

Whenever image matching fails, ground displacement cannot be estimated. Image matching can fail for a variety of reasons, most commonly because the scene has drastically changed between acquisition dates and corresponding points cannot be identified between images. Drastic changes are usually due to changes in snow/cloud/vegetation cover. Areas with steep slopes that create hidden parts (occlusions) also cannot be matched. The likelihood of occlusion increases with the increase of the off-nadir angle of the images. Occlusion problems are common in urban and mountainous areas.

As an illustration, Figure 17 shows the result of a 'blank' test (Leprince et al., 2007). Two SPOT 5 images from the same scene in the Mojave Desert area were chosen. The two images were acquired 6 months apart. No significant deformation event is known to have occurred in that period so that

the measurements should only reflect the various sources of noise and bias mentioned in the preceding text. These images have a GSD of 5 m, incidence view angle of  $-1.642^\circ$  and  $-1.726^\circ$ , and sun elevation of  $68^\circ$  and  $33^\circ$  and about the same sun azimuth. The two images were orthorectified using the 1/3 arcsec NED DEM from USGS, co-registered, and correlated following the flowchart of Figure 14. Offsets were calculated using the phase method using a  $32 \times 32$ -pixel sliding window with a step of eight pixels (80 m on the ground). The exterior orientation is satisfyingly modeled as we do not see the typical oscillating pattern due to jitter errors (roll, pitch, or yaw variation residuals). Offsets are at places correlated with the topography. They are too large to be explained by parallax effects given the near-nadir incidence. The artifacts, which reach up to a few meters, are seen only in the N-S component and are therefore more consistent with a shadowing effect. No other biases are visible, meaning that precise orthorectification and co-registration have been achieved. Other sources of errors result in some sort of a white noise with no spatial pattern. The histogram of offsets measured over the whole scene yields a close to normal distribution with a mean of 5.8 cm and a variance of 80 cm (Figure 18). The mean is 5 cm and the variance is 57 cm, on the E-W component that is less affected by shadowing. These errors are about one order of magnitude larger than those expected from the performance of the matching technique and are probably mostly due to natural changes of the scene.

Figure 20 illustrates the noise and artifacts of geodetic imaging with air photos. These images have a ground resolution of the order of 50 cm. The blank tests presented in this figure show that film distortions generally prevent measuring deformation at a wavelength larger than about 1 km. At shorter wavelengths, the noise level yields an rms of only 5 cm (so about 1/10 of the pixel size) essentially due to scan artifacts, temporal decorrelation, and shadow effect. This performance

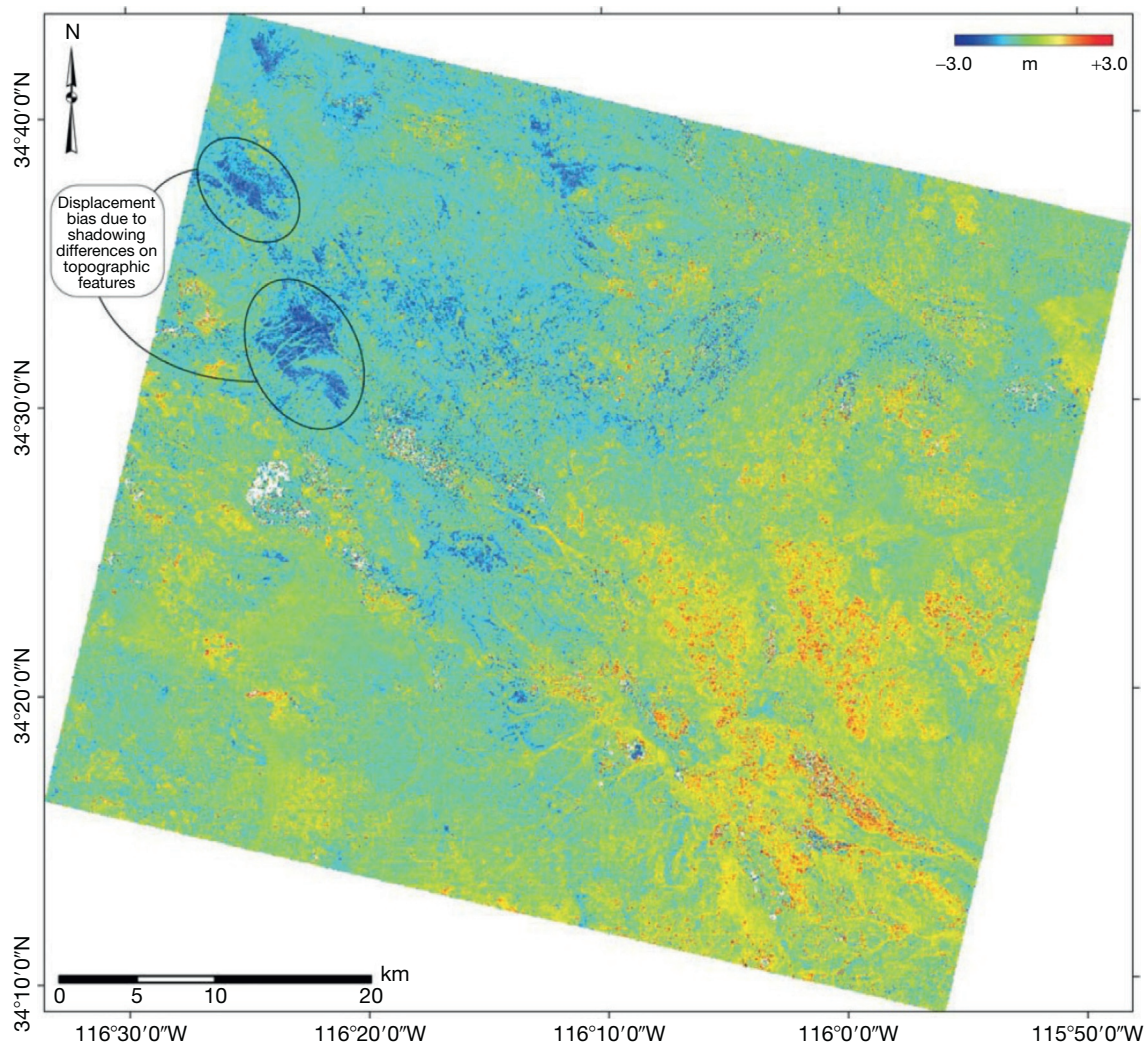


**Figure 17** N–S component of offsets between two orthorectified SPOT 5 images measured from the phase correlation method using a  $32 \times 32$ -pixel matching window (Leprince et al., 2007). The images show the 1999 Hector Mine earthquake area in the Mojave Desert. They were taken 6 months apart on 26 July 2002 and 24 January 2003. No significant earthquake occurred over that period and postsismic displacements are negligible. Shadowing biases are mostly visible in this component since the Sun azimuth of the two images is mostly N–S-oriented ( $127.72^\circ$  and  $158.15^\circ$ ). Decorrelation points are shown in white.

allows detecting and measuring surface slip on faults with as little as 10–20 cm of displacement (Ayoub et al., 2008; Michel and Avouac, 2006). These performances are achievable only if the quality of the scan is sufficient. Figure 19(b) shows the typical pattern and amplitude of scan artifacts resulting from a lower-quality scanning (here, the slave image has a nominal ground resolution of 80 cm). In that case, scan artifacts reach up to 20 cm and are clearly the main source of errors at short wavelengths ( $<1$  km).

### 3.13.6 Applications to Coseismic Deformation

#### 3.13.6.1 Usefulness of Coseismic Deformation Measurement from Image Geodesy

Earthquakes are associated with sudden slip events on faults. Large earthquakes therefore produce permanent surface

deformations, which might be measured from geodesy or remote sensing. When a fault rupture during an earthquake reaches the surface, as is often the case for  $M_w > 7$  crustal earthquakes, surface fault slip might also be measured directly from field investigations (e.g., Sieh et al., 1993). Field investigations take time so that this information is generally not taken into account in early source model determination. They are known to provide key insight regarding faults geometry and the distribution of slip and help constrain earthquake source models, which are often ill-constrained without this information (e.g., Konca et al., 2010). Detailed observation of recent ruptures is also important as it provides clues for the interpretation of past ruptures as revealed from paleoseismic investigations (Yeats et al., 1996). In the field, fault slip is generally estimated from the offset of linear features assumed initially continuous across the fault such as a road, a fence, or a terrace riser. Such features are not densely distributed so that measurements are often sparse, typically a few per kilometer. In

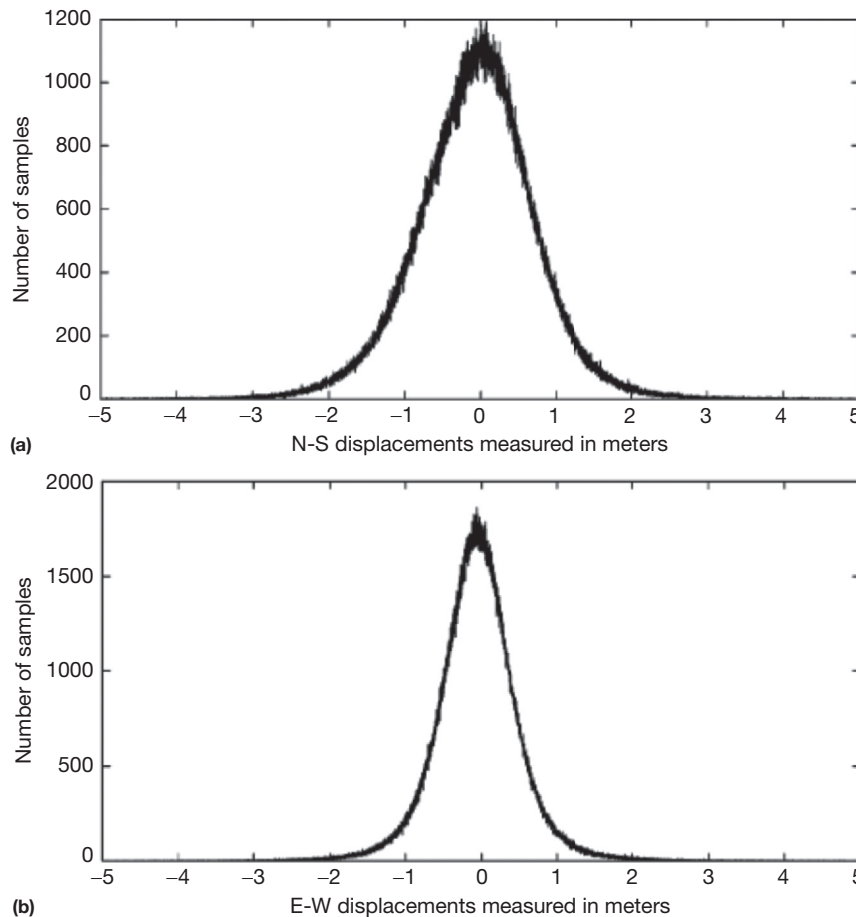


**Figure 18** Histograms of the offsets shown in Figure 17 (Leprince et al., 2007). (a) N–S component ( $\mu(\Delta NS) = -0.058$  m and  $\sigma(\Delta NS) = 0.80$  m). (b) E–W component ( $\mu(\Delta EW) = -0.051$  m,  $\sigma(\Delta EW) = 0.57$  m). The histograms are nearly Gaussian and can be seen as reflecting the noise on the measurements. The noise due to the correlation technique is probably only a very minor factor. Given the close incidence angles of the two images, topographic bias can only account for at most a few centimeters. The large difference in the Sun elevation then largely contributes in biasing the correlation measurements on topographic features.

addition, while the vertical and strike-slip component of fault slip can often be determined with some accuracy, the component perpendicular to the fault trace is most generally not measurable. Finally, these measurements are possible only across well-localized faults. If anelastic deformation is distributed, it is generally not possible to make any reliable measurement, unless the initial geometry of the linear feature can be assumed with confidence (e.g., in the case of well-aligned electrical poles). The measurement of surface fault slip from correlating images acquired before and after an earthquake is advantageous in that it does not suffer from any of those limitations and could in principle be produced quite early after an earthquake and taken into account for damage assessment. As it provides surface displacement in map view, the technique can in principle be self-sufficient to determine the distribution of fault slip at depth. This can in principle be achieved based on the theory of dislocations in an elastic half space (Okada, 1985) as commonly done with geodetic measurements and SAR interferograms. Geodetic imaging from optical methods is very complementary to these techniques as it provides information on near-fault deformation where geodetic measurements are rarely available and where SAR interferometry generally fails due to decorrelation induced by

ground deformation or damages or due to strain exceeding the fringe rate limit of one fringe per pixel (Chapter 3.12; Michel et al., 1999).

Numerous applications based on passive optical images have now been published (e.g., Avouac et al., 2006; Ayoub et al., 2009; Binet and Bollinger, 2005; Chini et al., 2011; Copley et al., 2011, 2012; Dominguez et al., 2003; Karabacak et al., 2011; Klinger et al., 2006; Konca et al., 2010; Michel and Avouac, 2002, 2006; Oskin et al., 2012; Taylor et al., 2008; Van Puymbroeck et al., 2000; Wei et al., 2011). A few major faults in California and elsewhere have been surveyed with LiDAR (Bevis et al., 2005; Phillips et al., 2008; Prentice et al., 2003). These data have been exploited to analyze the geomorphic signature of past earthquakes (Arrowsmith and Zielke, 2009; Hudnut et al., 2002; Zielke et al., 2010, 2012) or for method development (Borsa and Minster, 2012; Nissen et al., 2012). To date, the El Mayor–Cucapah earthquake of 2010 is the only earthquake for which LiDAR data had been acquired before the event (Oskin et al., 2012). We review in the succeeding text a selection of examples to illustrate the performance and limitations of the optical geodetic approach to measure coseismic deformation.

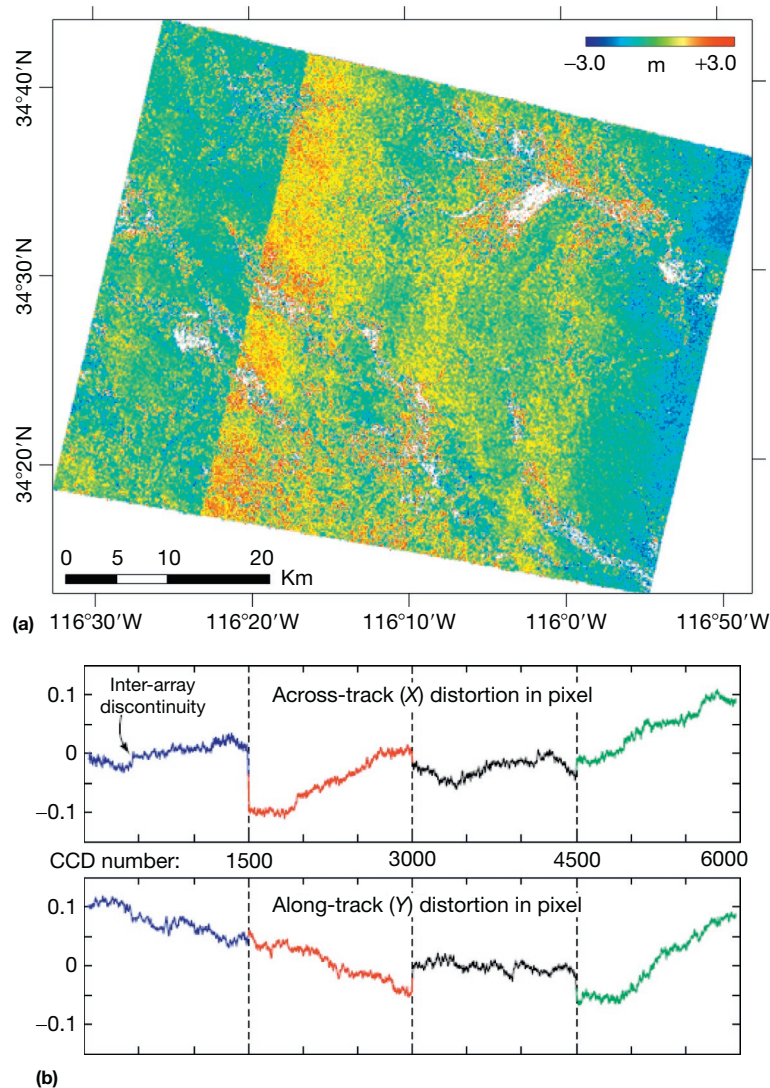


**Figure 19** (a) E–W component of the offset field measured from the subpixel correlation of a reference SPOT 5-HRG1 5 m panchromatic image acquired on 24 January 2003 and a slave SPOT 4-HRV1 10 m panchromatic image acquired on 11 March 2000 of same area of Mojave Desert as in Figures 22 and 19 (Leprince et al., 2008b). Both images were orthorectified using the 1/3 arcsec NED DEM from USGS. Thirty subpixel GCPs were used to tie the SPOT 5 image to the DEM, and six subpixel GCPs were used to tie both orthorectified images together. Correlation analysis was performed on  $32 \times 32$ -pixel matching windows, sliding with a step of 8 pixels (80 m on the ground). Linear artifacts reveal the SPOT 4 CCD distortions. (b) Measured distortions, in pixels, in the focal plane of the SPOT 4-HRV1 panchromatic sensor derived from the offset field shown in Figure 16 (Leprince et al., 2008b). The CCD line sensor is composed of four CCD line arrays of 1500 pixels each (vertical dotted lines). Both across-track and along-track distortions are measured with an uncertainty below 0.01 pixel rms. Distortions of up to 0.12 pixel ( $\sim 1.2$  m on the ground) are estimated allowing for precise geometric calibration of the whole CCD line sensor.

### 3.13.6.2 Surface Displacement in 2-D due to the 1999 Mw 7.6 Chichi Earthquake, Measured from SPOT Images

As a first illustration, Figure 21 shows the east–west (E–W) offset field measured from correlating two panchromatic SPOT images (pixel size of 10 m) acquired 29 January 1999 and 23 November 1999, respectively, 8 months before and 2 months after the earthquake (Dominguez et al., 2003). This earthquake resulted from thrusting on the Chelungpu fault along the western foothills of the Central Range in Taiwan. Field investigations provided tight constraints on the cartography of surface ruptures and the vertical and strike-slip

component of fault slip across the fault trace (Chen et al., 2001). The component of the slip perpendicular to the fault strike could not be measured in the field (hence, the E–W component as the fault is striking approximately N–S).

This example is interesting in that a quite dense dataset of near-field GPS data was available (Yu et al., 2001). Also, it illustrates well the benefit of the technique and the importance of a good modeling of image geometry when GPS data are not available. Given that no significant preseismic deformation was observed from the GPS permanent stations and that only a few centimeters of horizontal postseismic displacements were measured in the near-field areas over the 3 months that

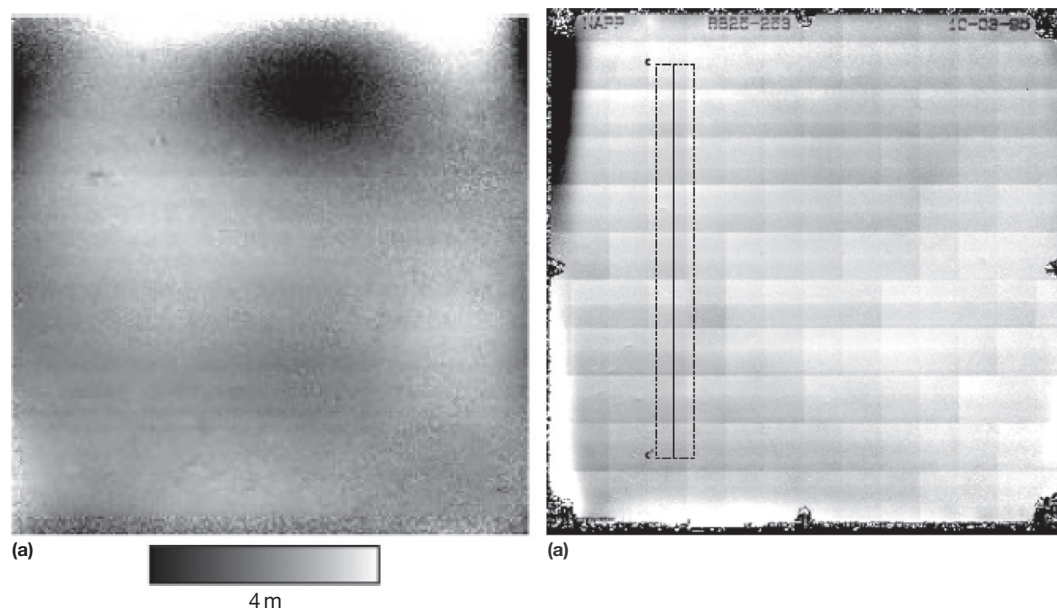


**Figure 20** (a) Offset field computed for two air photos from the 1992 Landers earthquake area (US National Aerial Photography Program) (Michel and Avouac, 2006). These images were acquired 3 and 10 years after the earthquake, respectively, and should therefore not show any significant ground deformation. Offsets were measured from the phase correlation technique with a matching window of  $32 \times 32$  pixels. These images, with a nominal film resolution of 10 mm corresponding to a ground resolution of 0.4 m, were scanned with a microdensitometer designed for astronomy with a theoretical positional accuracy of 0.6 mm and a root-mean-square error (RMSE) of 0.2 mm. The offsets field illustrates typical noise on measurement of ground deformation as measured from aerial photos. The low-frequency pattern results from unrecoverable thermomechanical deformation of films and prevents analysis of deformation of the ground at wavelength larger than about 1 km. Scan artifacts, temporal decorrelations, and shadow effects account for the noise at shorter wavelength. This noise has an rms of about 5 cm. (b) Along-line offsets measured from matching two scans of the same air photo from 1995 with the phase correlation method (Ayoub et al., 2008). One image was scanned with the microdensitometer and is used as the reference image. The other is the digital image downloaded from the US National Aerial Photography Program in 2006 (with a nominal 21 mm resolution). Correlation used a  $64 \times 64$  window with a 32-pixel step. Scan artifacts are obvious from the typical gridded pattern and reach up to 5 mm (equivalent to 20 cm on the ground). Other long-wavelength deformations are due to film distortion and misregistration.

followed the earthquake (Yu et al., 2001), we consider that the SPOT offsets essentially represent coseismic displacements.

Images acquired with similar near-vertical incidence angles ( $2.9^\circ$  and  $2.6^\circ$ ) were chosen in order to minimize orthorectification errors. It was assumed that distortions due to topographic errors could be neglected. With this assumption, the horizontal displacement field can be measured from correlating the orthorectified images taken before and after the earthquake. The DEM was produced from digitization of topographic maps with a data spacing of 30 m and an uncertainty estimated to about 20 m RMS. Orthorectification was performed without taking into account the information on the changing attitude of the satellite. Offsets between the two orthorectified images were next computed from the phase shift of the Fourier transform as described in the previous section using a multiscale procedure. They were first computed for a  $16 \times 16$ -pixel correlation window. If the uncertainty on the offset at a particular pixel was found to be larger than 0.3 pixel, the size of the correlation window was locally increased first to  $32 \times 32$  pixels and then to  $64 \times 64$  pixels if necessary. Only 5% of the measurements were filtered out by this procedure, yielding independent measurements every 160 m, in general (Figure 21(a)). The offsets show the surface rupture but are also clearly affected by residual artifacts with typical  $>20$  km wavelengths (Figure 21(b)). These artifacts result from the changing attitude (roll, pitch, and yaw) of the

satellite during image acquisition. These effects can now be modeled and optimized following the procedure described in the preceding text. In this early study, they were actually modeled based on the GPS measurements. A total of 59 GPS geodetic measurements were available in the area covered by the SPOT images (see circles in Figure 21(c)). The offset field was first filtered using a median filter to remove very short-wavelength ( $<1$  km) noise related to local temporal decorrelation. Differences between offsets and GPS were next calculated for both E-W and N-S components revealing the artifacts introduced by the changing attitude of the satellite. The residuals (Figure 21(c)) were then interpolated using bicubic spline functions. These residuals show that jitter effects can bias offset measurements by up to 15 m if they are not properly modeled or compensated for. Figure 21(d) shows the amplitude of the offset field after compensation for these biases. This procedure yields a displacement field that benefits from the dense spatial coverage provided by SPOT offsets and the accuracy of the sparse GPS measurements. Jitter effects have been relatively well filtered out. The fault trace is clearly revealed, and the two components of the horizontal slip vector along the fault trace can be measured with an accuracy of a few tenths of centimeters.

This example shows the artifacts potentially introduced by improper modeling of the jitter and how these artifacts can be mitigated when geodetic measurements in the near-field area are available.

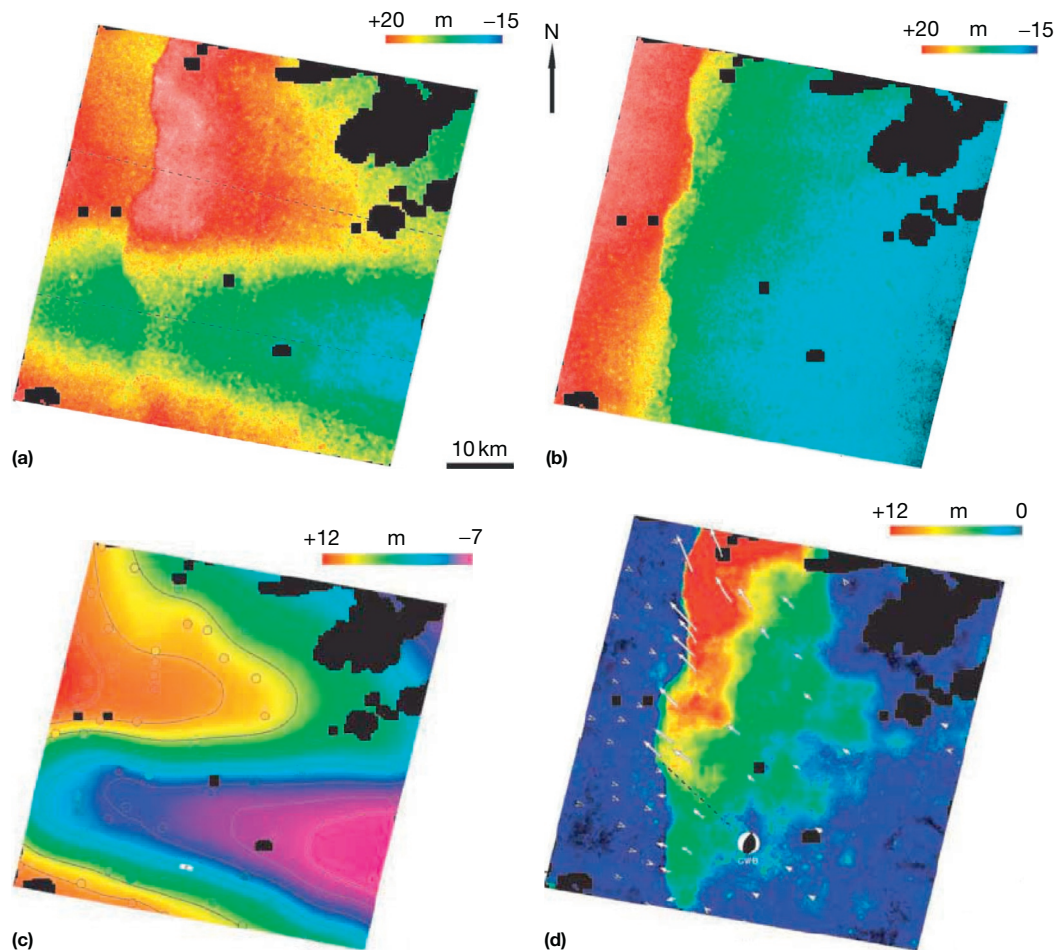


**Figure 21** N–S (a) and E–W (b) horizontal offsets determined from the correlation of two SPOT images with 10 m GSD acquired 10 months before and 2 months after the Mw 7.6 Chi-Chi earthquake in 1999. Offsets are determined from the subpixel phase correlation of orthorectified images. Independent measurements every 160 m. The offset field reveals a sharp discontinuity along the fault trace. Long-wavelength artifacts due to the satellite jitter (the changing attitude characterized by the roll, yaw, and pitch) during image acquisition are also obvious especially on the N–S component. These artifacts were modeled based on the residuals (shown in (c)) between those measurements and the GPS measurements collected at 59 sites (circles). Panel (d) shows the amplitude of the offset field after compensation for these residuals filtered at wavelength larger than 20 km. Modified from Dominguez S, et al. (2003) Horizontal coseismic deformation of the 1999 Chi-Chi earthquake measured from SPOT satellite images: Implications for the seismic cycle along the western foothills of central Taiwan. *Journal of Geophysical Research-Solid Earth* 108(B2), art. no.-2083.

### 3.13.6.3 Surface Displacement in 2-D due to the 2005 Mw 7.6 Kashmir Earthquake, Measured from ASTER Images

Another application to a thrust earthquake is illustrated in [Figure 22](#). In that case, two ASTER images ([Abrams, 2000](#)) with a ground resolution of 15 m were used to map surface ruptures due to the Mw 7.6 Kashmir earthquake, which struck the northwestern Himalaya near the town of Muzaffarabad on 8 October 2005 ([Avouac et al., 2006](#)). This example was particularly challenging due to a number of factors. First, ASTER images have a lower ground resolution of 15 m and less accurate telemetry as compared with the SPOT 2 and SPOT 4 images used in the previous example. The relief in the epicentral area is extremely rugged, enhancing the risk of strong topographic artifacts. Because of the necessity to use images with similar incidence angles so as to limit the topographic errors, two images with quite close view angles were chosen. The first image was acquired on 14 November 2000 and the

second on 27 October 2005. The large time span between the two images was enhancing the risk of temporal decorrelation. Finally, there was no geodetic measurement of coseismic displacement in the near-field area, which could have been used to compensate jitter effects.

The images were orthorectified on a common 15 m resolution grid using a 30 m DEM computed from a stereo pair of ASTER images. Offsets were measured from the local cross correlation of the two orthorectified visible near infrared (VNIR) 3 N bands ([Figure 22\(a\)](#)). These measurements show that the surface rupture reached the surface, although field evidence for fault ruptures was scant. In addition to the coseismic signal, a wave pattern, running in the satellite along-track direction, reflects the undersampling of the satellite attitudes that therefore could not be accurately accounted for during orthorectification. This pattern is characteristic of unmodeled pitch variations. A similar pattern on the E–W component reflects roll variations. The Terra onboard attitude

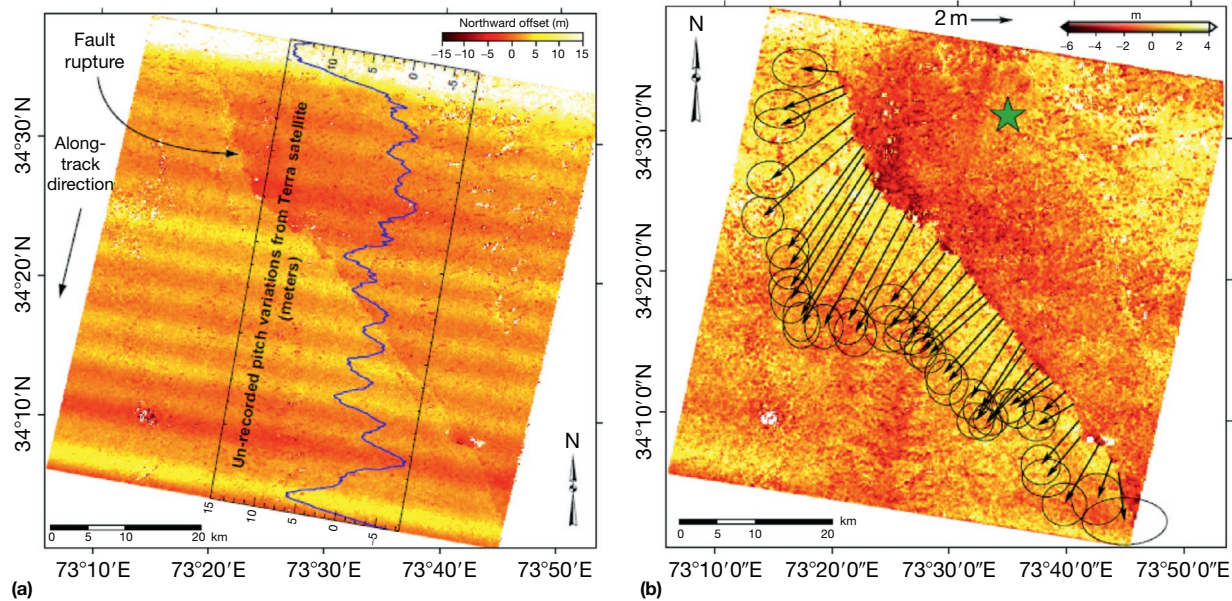


**Figure 22** (a) Northward component of offset field measured from correlating ASTER images with 15 m GSD acquired before and after the 2005 Kashmir earthquake. This correlation was obtained with a sliding  $32 \times 32$  pixels correlation window and a 8 pixels step, leading to a ground resolution of 120 m. The points where no measurements were retrieved due to loss of correlation are shown in white. Correlation was lost mostly due to landslides. The fault rupture is visible as a discontinuity in the offset field. The ground displacement signal due to the earthquake is overprint with a wave pattern due to the jitter during the image acquisition. This signal can be estimated by stacking the offset along the lines yielding the blue curve overlaying the offset measurements. (b) Same as (a) after filtering out the jitter effect. Vectors show horizontal slip vectors at about 2 km spacing along the fault trace, measured from the discontinuity of E-W and N-S ground displacement measured at the fault on 18 km long, 6 km wide profiles run perpendicular to the fault. NS and EW offsets at the fault are measured from linear least-squares adjustment on each side of the fault. Ellipses show 2-s uncertainties (95% confidence level) on each measurement.

recorders have a sensitivity of 1 arcsec (corresponding to around 3.4 m on the ground for VNIR images) and a sampling rate of 0.97 Hz corresponding to one measurement every 500 lines or 7.5 km on the ground. This sampling rate is insufficient to record properly the spacecraft jitter observed in Figure 22(a). Similar artifacts in amplitude and frequency were also reported in other studies (Ayoub et al., 2008; Iwasaki and Fujisada, 2003). The relatively short wavelength of the jitter artifacts (5 km, corresponding to vibration around 1 Hz of the Terra platform) would prevent the possibility of compensating them based on geodetic ground measurements as discussed in the previous section. In this particular example, the jitter pattern could be extracted by running profiles in the along-track direction and not intersecting the fault trace. The profiles were next stacked in the across-track direction and subtracted from the original measurements. This yielded the offset field of Figure 22(b) where jitter artifacts are hardly visible any more. This rather crude dejittering procedure thus appears to be quite effective in the context of ASTER images. A more sophisticated optimization procedure could be applied if another image with better controlled attitude was available.

The offset field reveals a clear discontinuity, which can be traced over a distance of about 75 km. Despite the 5-year interval between the two images, the correlation is good, except at locations where major landslides were triggered by the earthquake. The horizontal slip vector on the fault can be measured accurately from profiles run across the fault trace with an accuracy of about 1 m on average at the 95%

confidence level. This example shows that images with relatively low ground resolution (15 m in that case) and poor telemetry can nonetheless yield useful measurements.

#### 3.13.6.4 Surface Displacement in 2-D due to the 1999 Mw 7.1 Hector Mine Earthquake Measured from SPOT Images

We now comment on the measurements of coseismic surface displacement due to the Mw 7.1 Hector Mine earthquake in 1999. This earthquake is purely strike slip and a relatively dense measurement of surface fault slip was collected in the field (Treiman et al., 2002) and could be compared with the measurements obtained from optical image correlation. Figure 23 shows the offset field measured from correlating SPOT 4 and SPOT 2 images, with an  $\sim 10$  m ground resolution, bracketing the earthquake (Leprince et al., 2007). In this example where the two images have a near-vertical incidence angle ( $< 2^\circ$ ), it was assumed that distortions due to topographic errors could be neglected. With this assumption, the horizontal displacement field can be measured from correlating orthorectified images taken before and after the earthquake. Two images taken at about the same date in the year were chosen so that the Sun elevation be as close as possible to avoid shadowing artifacts: a SPOT 4 image (image 1) acquired in August 1998 and a SPOT 2 image (image 2) acquired in August 2000. The two images were orthorectified using the 1 arcsec SRTM DEM (Farr et al., 2007), which has a ground resolution of 30 m.

Correlation was performed with  $32 \times 32$  pixel ( $320 \times 320$  m<sup>2</sup>) sliding windows and with a step of eight pixels (80 m) (Figure 23).

Correlation errors are mostly the consequence of surface changes that occurred during the 2 years separating the acquisitions. Other sources of noise include errors of geometric modeling of the orthoimages due to the topographic errors, CCD misalignments, and mismodeling of the satellite attitude during image acquisition. Altogether, these various sources of errors are estimated to contribute to the noise level with closely unbiased Gaussian distribution and a standard deviation of about 0.8 m on the north–south (N–S) component and 0.57 on the E–W component of displacement. The noise due to correlation errors can be filtered out, for example, using the nonlocal means filter (Buades et al., 2008), which has the advantage of not smoothing out discontinuities. This filter has been applied in the filtered version of Figure 23 shown in Figure 6. The discontinuity due to the surface rupture is therefore well preserved with this filtering technique. The surface rupture appears as a discontinuity in the displacement field. Some systematic errors remain, however. Some are clearly due to CCD misalignments (Figure 23), which were not corrected for with sufficient accuracy. The filtered image (Figure 6) also shows a slight residual jitter effect in the form of a wave pattern in the N–S component of the displacement field. This wave pattern, which is hardly visible in the nonfiltered displacement field (Figure 23), is due to mismodeling of pitch variations and results in offset artifacts with amplitude of about 1 m. These artifacts are a limitation with regard to the measurement of absolute fault displacement.

However, they do not affect the measurement of surface fault slip. Due to improvement of telemetry onboard the SPOT program satellite, this kind of artifact is not seen with more recent imaging systems (SPOT 5 and up).

The horizontal slip vector was measured from 8 km long, 880 m wide swath profiles taken perpendicular to the fault trace and spaced every about 880 m (Figure 24). Each horizontal coseismic displacement measured on the fault is up to 6 m in the N–S direction and up to 3.5 m in the E–W direction. The horizontal coseismic fault slip at the surface is therefore accurately and densely (every 80 m) recovered from the proposed technique. With the nominal images resolution of 10 m, all the measurements are in the subpixel range, within  $\pm 3$  m. In the N–S correlation image, a secondary rupture branches to the north where the main rupture bends. The coseismic displacement measured on this secondary branch is up to 1 m. These examples show that surface ruptures with surface slip of  $< 1/10$  of the pixel size can be detected and measured from this technique.

The location of the fault trace and the surface fault slip recovered from the SPOT image compare well with the surface ruptures and fault slip measured in the field (Figure 24). In fact, fault slip measured from the SPOT images is close to the maximum slip measured in the field and varies smoothly along strike. A similar conclusion has been reached wherever it has been possible to compare field measurement and measurement made to geodetic imaging (Konca et al., 2010; Michel and Avouac, 2002; 2006; Taylor et al., 2008). This observation suggests that the variation of slip generally revealed from field

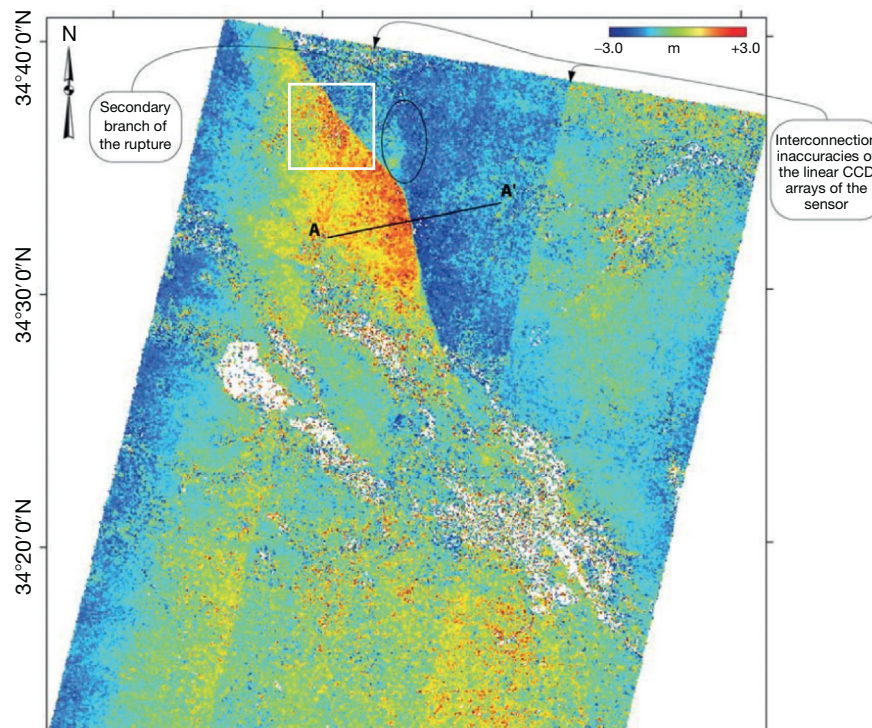


**Figure 23** North component (positive to the north) of the coseismic displacement field due to the 1999 Mw 7.1 Hector Mine earthquake in California measured from correlated SPOT 2 and SPOT 4 monochromatic images with 10 m GSD acquired on 12 August 1998 and 10 August 2000 (Leprince et al., 2007). Both images were orthorectified and co-registered on a 10 m-resolution grid, and the offsets were measured from subpixel correlation within a  $32 \times 32$ -pixel sliding window. The displacement field is shown at a ground resolution of 80 m. See Figure 6 for filtered version of these measurements. White box shows location of Figure 25

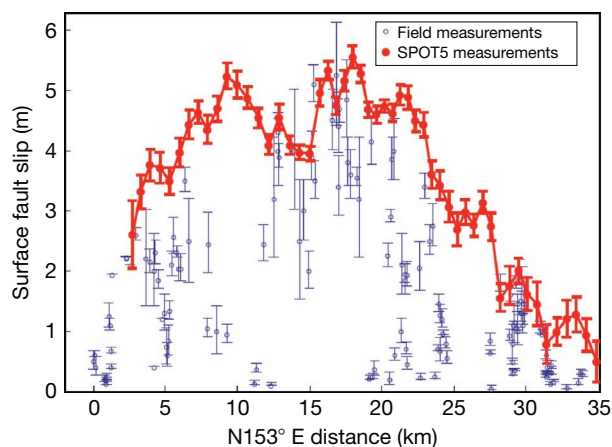


**Figure 24** Right-lateral slip along the Hector mine earthquake surface rupture. Slip is determined by projecting the horizontal slip vectors along the fault strike. Horizontal slip vectors are measured from linear least-square adjustment, on each side of the fault and on each N–S and E–W image of stacked profiles running perpendicularly to the rupture (as shown in Figure 6). Profiles are stacked over a width of 880 m and a length of 8 km. Error bars show 2- $\sigma$  uncertainties (95% confidence level). Field measurements (Treiman et al., 2002) are also reported for comparison. Modified from Leprince S, et al. (2007) Automatic and precise orthorectification, coregistration, and subpixel correlation of satellite images, application to ground deformation measurements. *IEEE Transactions on Geoscience and Remote Sensing* 45(6): 1529–1558.

investigation of surface rupture at the kilometeric scale or less is probably due to the fact that the total slip across the fault is in fact partitioned between slip on faults identifiable in the field and more distributed anelastic strain. This observation suggests that a significant portion of coseismic slip may in some cases escape detection by conventional field measurements alone. A corollary is that the along-strike variability in fault slip observed in the field may actually reflect lateral variations in the mechanical response of near-surface layers to the dynamics of earthquake rupture.

### 3.13.6.5 Surface Displacement in 2-D due to the 1999 Mw 7.1 Hector Mine Earthquake Measured from Air Photos

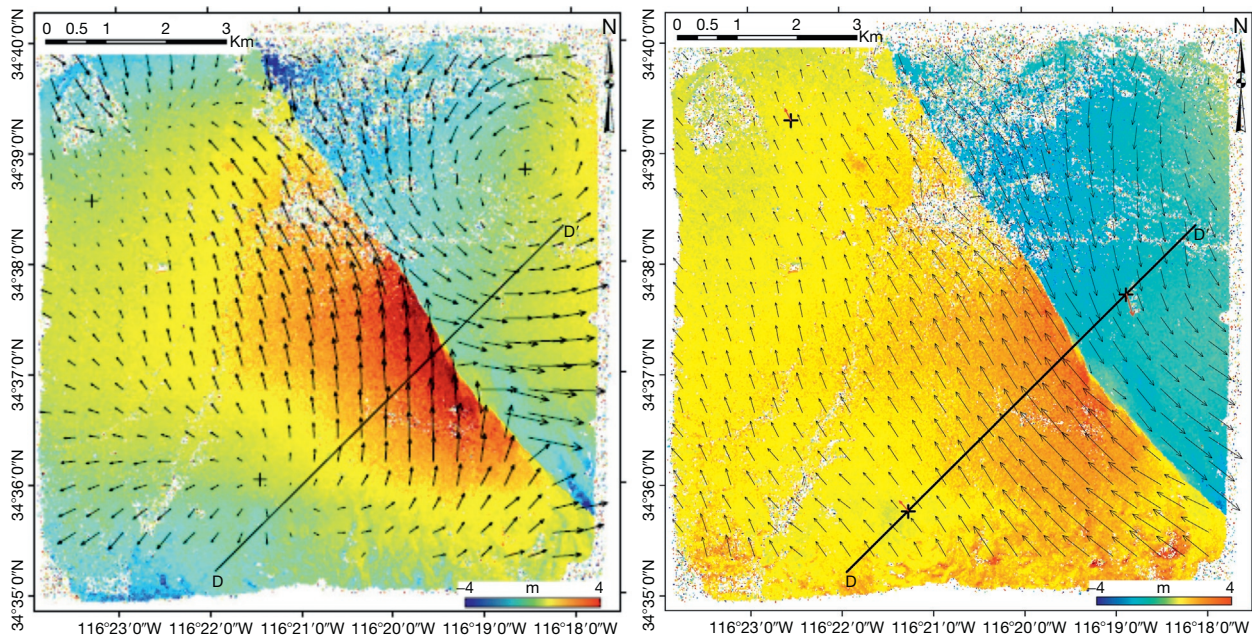
The spatial resolution and accuracy of ground displacement resolution scale in principle with the resolution of the optical images. There is nowadays a good archive of satellite imagery with decametric resolution like the SPOT and ASTER images exploited in the examples presented in previous subsections. In principle, these data are appropriate to study Mw > 7 earthquakes, which generally produce surface slips in excess of 1–2 m. The measurement of more subtle deformation would require images with higher ground resolution as now available from a number of satellite programs (e.g., IKONOS, WorldView, and Pleiades). In most countries, air photos with a submetric resolution collected by national surveying agencies are available providing the possibility to revisit past events. The exploitation of such data can be challenging due to scanning artifacts and possible distortions of the prints or films but some success was reached (Ayoub et al., 2009; Michel and Avouac, 2006).

Figure 25 shows, for example, the N–S component of the displacement determined from correlated air photos from the USGS–NAPP (US Geological Survey–National Aerial Photography Program), taken in 1989 and 2002 and covering a portion of the rupture produced by of the Hector Mine earthquake (see Figure 23 for location of footprint). The footprint of these images is about  $10 \times 10 \text{ km}^2$ . The original film nominal resolution of about  $10 \mu\text{m}$  corresponds to a ground resolution of about 0.4 m.

The two images were orthorectified using the 1 arcsec SRTM RTM DEM. The IO models of the 1989 and 2002 images were established based on the camera calibration reports provided by the USGS. The 2002 image was co-registered first to the topography as the SRTM mission was carried out in 2000 (both postearthquake). A shaded image of the DEM was generated with illumination parameters estimated from the 1989 image shadow pattern. A handful of GCPs were selected between the image and the shaded DEM. Horizontal and vertical coordinates were both obtained from the georeferenced DEM. The average residual misregistration after GCP optimization was estimated to be 2.4 m, while the standard deviation residual was estimated to be 18 m. This latter uncertainty is slightly higher than the 15 m relative horizontal accuracy of the SRTM DEM. More GCPs would have helped improve the co-registration, but the limited radiometric texture due to the desertic setting did not allow it. The 1989 image was orthorectified on a 1 m-resolution grid. Three GCPs, indicated by the black crosses in Figure 25, were optimized to co-register the two images. First, the ground displacement at these locations was ignored. After GCP optimization, the average residual misregistration was evaluated to 1 mm and the standard deviation residual to 35 cm. Ground displacements were next determined from correlating the two co-registered images using a  $64 \times 64$ -pixel sliding window with a 16-pixel step. The discontinuity of ground displacement along the fault trace is nicely revealed. We observed that long-wavelength distortions are introduced to satisfy the no displacement constraints at the location of the GCPs used to co-register the two images. This is obviously an artifact of the procedure. The optimization of the EO model is biased so that the displacements at the location of the GCPs are minimum.

Such artifacts would happen if the footprint of the image is smaller than the deforming zone, as is the case here, and if no a priori information on GCPs displacement is available. In this particular case, the displacement at the location of the GCP can be estimated based on the results obtained from the SPOT images correlation. Panel (b) in Figure 25 shows the results obtained in that case. The long-wavelength distortions have been removed. Only the long-wavelength distortions caused by the SPOT correlation error may remain, along with those introduced by film distortions. These are relatively small and would not impair a precise measurement of fault slip.

This example illustrates one difficulty that generally arises with high-resolution imagery. Due to their limited footprint, it might not be possible to define GCPs outside the deformation zone. If displacements at the location of the GCPs used for the co-registration are unknown, ground deformation at wavelengths larger than the typical wavelength defined by the geographic distribution of the GCPs is filtered out. Deformation at smaller wavelengths is preserved so that this is generally not a



**Figure 25** Displacement due to the 1999 Hector Mine earthquake measured from correlation of air photos from 1989 and 2002 with 1 m GSD. The color shade shows amplitude of N–S displacement and vectors show the horizontal displacement vectors. Images were orthorectified on a 1 m grid and correlated using a  $64 \times 64$ -pixel window with a 16-pixel step. Three GCPs, indicated by the black crosses, were optimized to co-register the master and slave images. (a) Long-wavelength distortions are introduced to satisfy the constraint of no displacement at the location of the GCPs during the co-registration. (b) Long-wavelength distortions are removed if the displacements measured from the SPOT image correlation at the location of the GCPs are accounted for during co-registration.

limitation to measure coseismic slip. The general procedure would require a bundle optimization of all the overlapping images. The referencing to a known geodetic reference frame requires that some of the images would extend to non-deforming zones or independent measurements of the displacement at a subset of GCPs.

### 3.13.6.6 Surface Displacement in 3-D due to the 2010 Mw 7.2 El Mayor–Cucapah Earthquake from LiDAR and Optical Images Stereomatching

The Mw 7.2 El Mayor–Cucapah earthquake that struck southern California on 4 April 2010 is the first earthquake for which pre- and postearthquake LiDAR data were available (Oskin et al., 2012). Pre- and postearthquake images with an  $\sim 50$  cm GSD and varied viewing angles are also available from WorldView. This exceptional dataset makes it possible to determine the near-field ground displacement in 3-D.

We first show and comment on the 2-D measurements of surface deformation that were produced as early as 1 week after the quake (Wei et al., 2011). These measurements were produced from correlating a pair of panchromatic SPOT 5 images with 2.5 m ground resolution acquired on 26 May 2009 and 8 April 2010, which cover the northern half of the rupture length. Images with near-nadir-looking angles and incidence angle difference of  $6^\circ$  were chosen to minimize topography parallax. These images were orthorectified using the 30 m NED DEM and processed for 2-D horizontal displacement (Figure 26). Matching was performed using the phase correlation method with a  $64 \times 64$ -pixel sliding window at every

16 pixels. It results in a displacement field sampled at 40 m ground resolution. Because of the rugged topography of the Sierra de Los Cucapah and the high resolution of the images compared with the DEM resolution, strong topographic distortions were to be expected. Slight topography residuals indeed show in the E–W component. The N–S component of the displacement field is nearly perpendicular to the epipolar direction of the image pair and is devoid of topography residuals. Both components clearly show the fault trace running through the Sierra de Los Cucapah. It should be pointed out that, due to its unexpected location within the core of the Sierra, these surface ruptures were initially missed during the helicopter reconnaissance carried on in the early days after the quake (Ken Hudnut, personal communication). These measurements reveal a continuous fault trace of about 120 km with an average surface slip of about 2 m. Ruptures with more than 50 cm of surface slip can be detected and mapped with this dataset.

The availability of LiDAR analysis of pre- and post-earthquake topographic data provides an opportunity to deliver the full 3-D displacement field of the ground's surface. However, as discussed in Section 3.13.2.1 and illustrated in Figure 2, direct differencing of a pre- and postearthquake digital topography model (DEM) generally leads to biased estimation of the vertical component of the deformation especially if the earthquake also produced significant horizontal motion. To overcome this limitation, we use the COSI-Corr subpixel correlation algorithm to estimate the relative horizontal offset between the pre- and post-2010 El Mayor–Cucapah earthquake high-resolution LiDAR acquisitions. This analysis

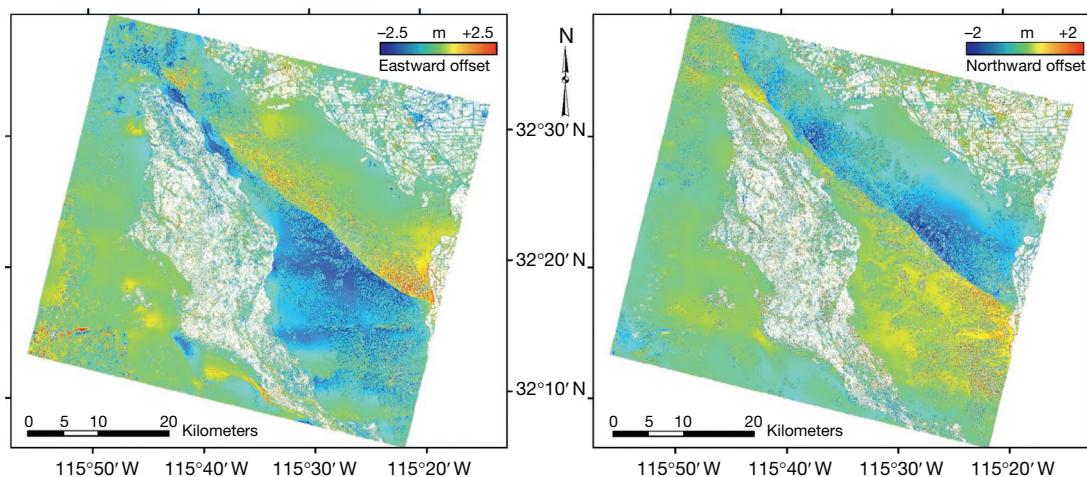


**Figure 26** N–S and E–W surface displacements (positive northward) induced by the 2010 Mw 7.2 El Mayor–Cucapah earthquake (Wei et al., 2011). These measurements were produced from a pair of panchromatic SPOT 5 images with 2.5 m GSD acquired on 26 May 2009 and 8 April 2010. These images cover the northern half of the rupture length. These images were orthorectified using the 30 m NED DEM. Image cross correlation was performed using a  $64 \times 64$ -pixel sliding window and step of 16 pixels, resulting in a displacement field sampled at every 40 m. Slight topography residuals are visible in the E–W component but the N–S component, which is nearly perpendicular to the epipolar direction of the image pair, is devoid of topography residuals.

shows an unprecedented view of the complete vertical slip component of the rupture induced by the Mw 7.2 2010 El Mayor–Cucapah earthquake, sampled at every 5 m, over a length of about 100 km, and with a vertical accuracy of a few centimeters (Figure 27) (Leprince et al., in preparation). These measurements reveal that the LiDAR data suffer from jitter and tiling artifacts, probably associated to the lower-quality pre-EQ dataset. Horizontal displacements are therefore strongly biased with systematic misregistration errors exceeding several meters. The tectonic signal is clear, however. By contrast, the measurements of vertical displacements are accurate to within 10 cm and reveal nicely details of the fault rupture at the 100 m scale.

We show in Figure 28 the surface displacements retrieved using the 2-D method applied to two WorldView images bracketing the El Mayor–Cucapah earthquake. Both were orthorectified using the 30 m NED DEM. The results show strong topographic artifacts in the N–S component, which is close to the epipolar direction (along the track of the sensor's motion which is mostly in the N–S direction). This example highlights the necessity of stereo acquisitions when images cannot be acquired at nadir.

The results obtained with the 3-D method illustrated in Figure 9 are presented in Figure 29. Four images with 50 cm GSD were used (QuickBird or WorldView). The standard deviation on the measurement of horizontal displacements is about 10 cm ( $1/5$  of the pixel size) and about 25 cm on the vertical. The spatial distribution of horizontal displacements suggests that errors are dominated by CCD and jitter artifacts.

### 3.13.7 Applications to Geomorphology and Glacier Monitoring

#### 3.13.7.1 Glacier Monitoring

In the current climatic context, the monitoring of continental ice and a better understanding of glaciers' dynamics are crucial

as the fate of mountain glaciers is very poorly constrained. This issue can be addressed from cross correlation of optical imagery (Berthier et al., 2005; Heid and Kaab, 2012; Scherler et al., 2008, 2011). The capability of correlation of passive optical images to measure glacier's surface velocities is illustrated in Figure 30. In this application, the technique tracks surface features of the glacier such as crevasses, debris, and ogive bands (Figure 31). These features are assumed to be advectively transported with ice flow. This is a first-order approximation that ignores the effect of ablation and accumulation. The horizontal displacements in the Mer de Glace area (Alps), over 26 days (23 August 2003 to 18 September 2003), were derived from SPOT 5 images with 2.5 m GSD (Leprince et al., 2008a). Very few areas of decorrelation are observed and, when present, are mainly due to changes in length and orientation of the mountain shadows between the two dates. Around the main glaciers, many small disconnected regions (subkilometric size) have measurable motion, then showing a complete picture of the ice flow field. This study reveals details of the ice surface velocity field, which can help calibrate and validate glacier-flow models. The measurements made from the SPOT image compare well with ground-based GPS measurements along a central flow line. The GPS displacements are larger by about 10% probably mostly because they do not cover the exact same time period as the SPOT measurements. The time period covered by the GPS (12 August to 03 September 2003) starts indeed slightly earlier in the summer at the time of the peak heat wave of August 2003 (Berthier et al., 2005). The consistency between the two datasets validates the method despite that some ablation must have occurred in the time period separating the acquisition of the two SPOT images. The measurement was successful most probably because surface features are preserved during ablation as debris remains at the surface and crevasses and ogive bands are bulk properties that extend at depth. As ice is ablated, the surface pattern of crevasses and ogive bands remains approximately stationary.

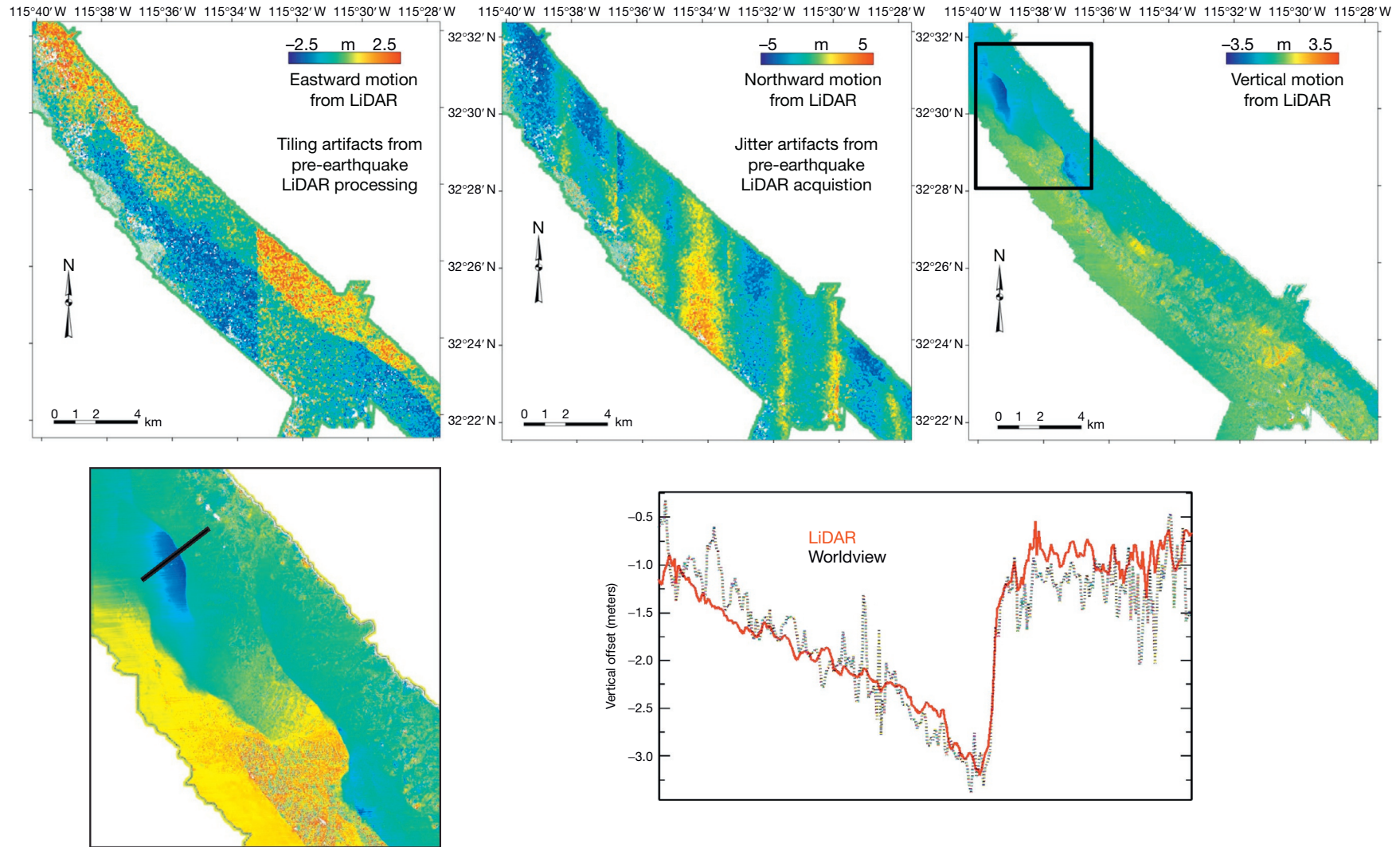


**Figure 27** 3-D offset recovered from LiDAR and comparison of the vertical offset recovered using WorldView data (Figure 28). We see that the LiDAR horizontal components show strong tiling and jitter artifacts due to uncorrected aircraft attitude control and processing inaccuracies. The pre-earthquake LiDAR was gridded at 5 m, and the postearthquake LiDAR, although acquired at a resolution of 50 cm, was resampled on a 5 m grid to match the pre-earthquake LiDAR dataset. Box in upper-right panel shows close-up view of lower left panel where location of profile shown in lower right panel is indicated. Red line shows LIDAR measurement and black dotted line shows World view measurements.

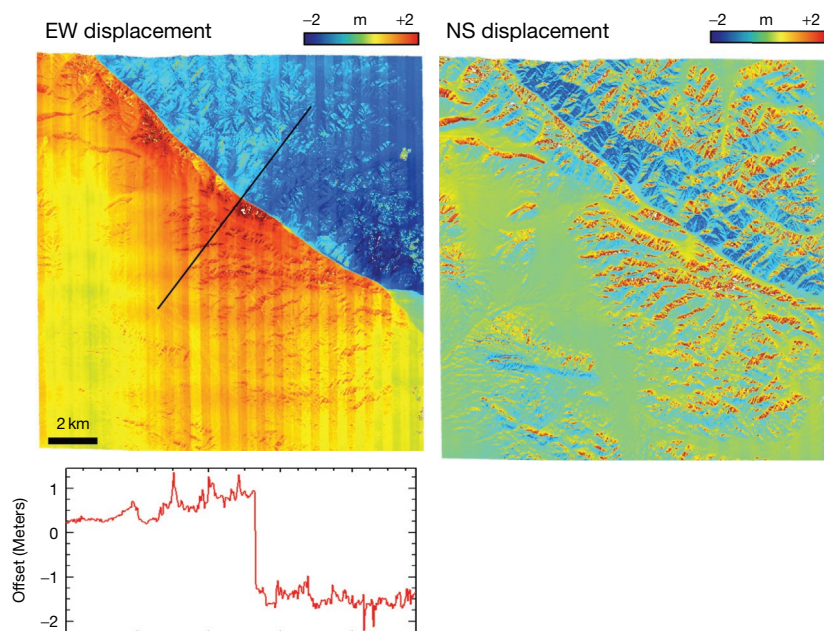


**Figure 28** E–W and N–S surface displacements retrieved using only two WorldView images bracketing the El Mayor–Cucapah earthquake. Pre-earthquake images: WorldView 16 September 2008 (along-track angle:  $-10.8^\circ$  and across-track angle:  $13.5^\circ$ ). Postearthquake images: WorldView 10 April 2011 (along-track angle:  $-13.8^\circ$  and across-track angle:  $-22.5^\circ$ ). We see that large artifacts are introduced in the N–S component, which are due to topographic residuals along the epipolar direction (along-track sensor, which is mostly in the N–S direction). This example highlights the necessity of stereo acquisitions when images cannot be acquired at nadir.

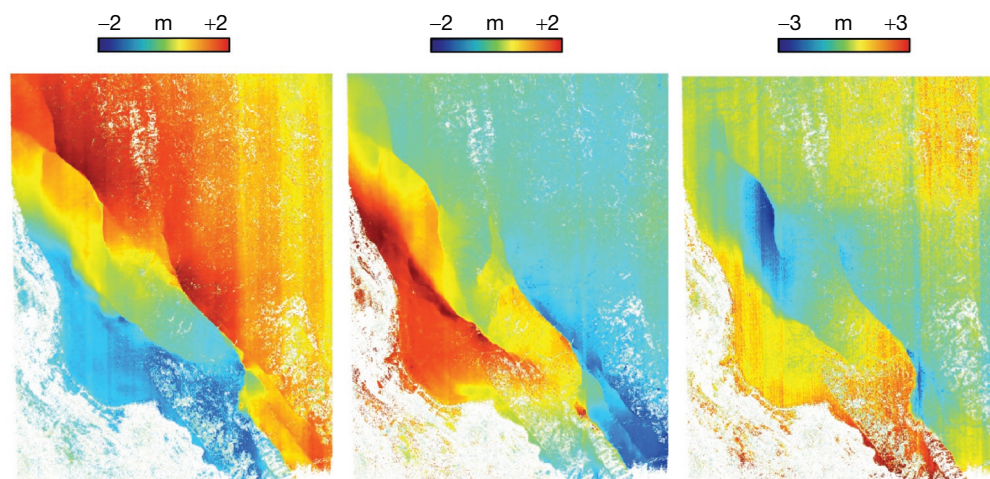


**Figure 29** 3-D displacement field of the 4 April 2010, El Mayor–Cucapah earthquake retrieved using the method in [Figure 10](#). Four images were used: pre-earthquake images, QuickBird 21 September 2006 (along-track angle:  $-1.23^\circ$  and across-track angle:  $-9.8^\circ$ ) and WorldView 16 September 2008 (along-track angle:  $-10.8^\circ$  and across-track angle:  $13.5^\circ$ ) and postearthquake images, WorldView 10 April 2011 (along-track angle:  $-13.8^\circ$  and across-track angle:  $-22.5^\circ$ ) and WorldView 19 May 2011 (along-track angle:  $14.1^\circ$  and across-track angle:  $21.6^\circ$ ).

Some bias could be introduced due to the dip angle of the bands. This bias seems negligible here.

This example demonstrates the potential and performance of optical image correlation for the measurement of surface ice flow. In principle, the mass balance of glaciers could be tracked from repeated stereo pairs of optical images or LiDAR survey using the 3-D matching techniques described in the preceding text. Such an approach should be more precise than simple DEM differencing ([Berthier et al., 2006](#)) as it should in

principle mitigate misregistration bias and provide a better resolution provided that glacier surface features remain coherent in the dataset.

### 3.13.7.2 Earthflows

Earthflows resulting from slow-moving mass movement are a common phenomenon on clayey hillslopes. Earthflows might be a major geomorphic factor, capable of eroding hillslopes at

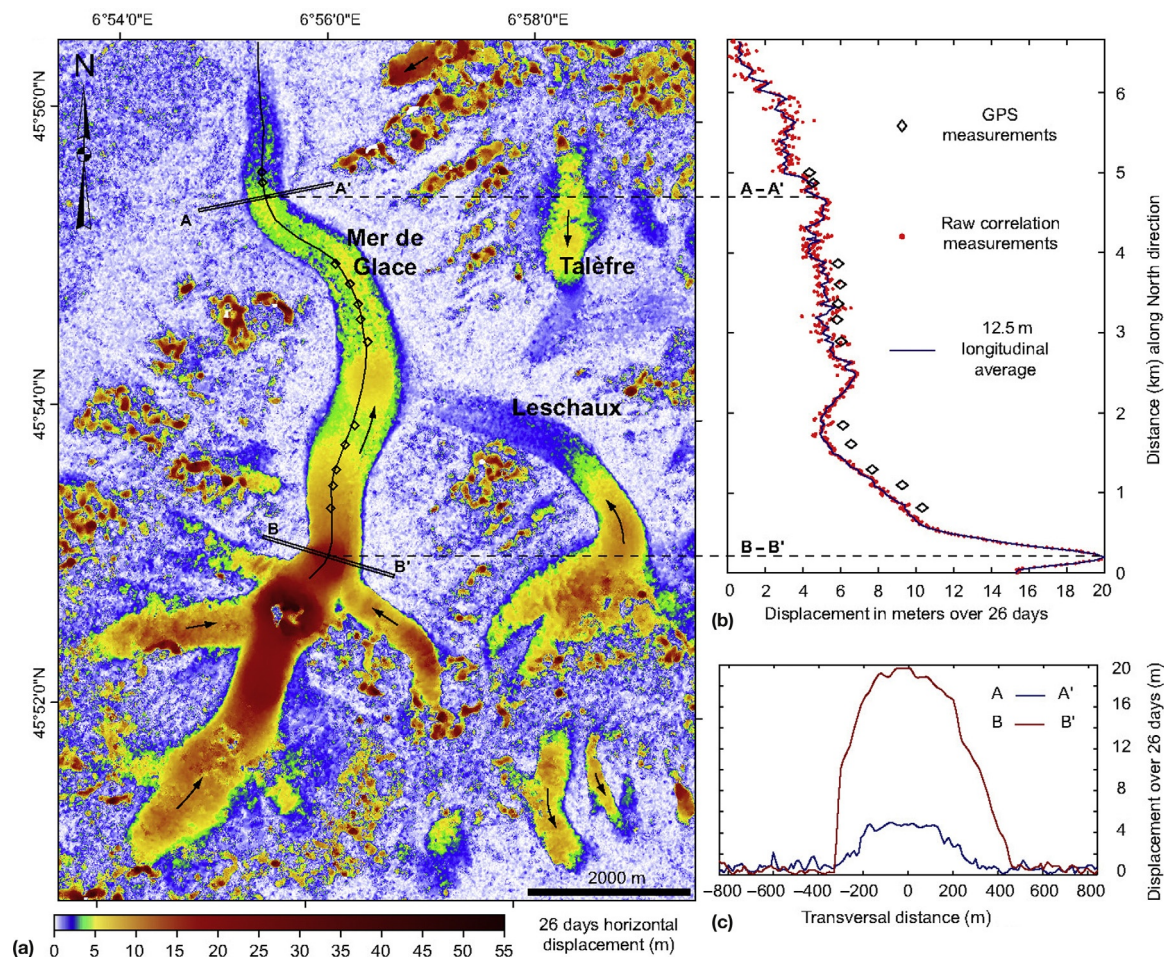


**Figure 30** (a) Amplitude of the horizontal displacement over the Mer de Glace area from 23 August 2003 to 18 September 2003 (Leprince et al., 2008a). The displacement field was computed from the subpixel correlation of two panchromatic SPOT 5 images with 2.5 m GSD, using a sliding window of size  $32 \times 32$  pixels and a step of 16 pixels. Arrows show the flow direction. Displacements as high as 55 m (about  $800 \text{ m year}^{-1}$ ) are recorded over this 26-day period. Box shows location of Figure 30. (b) Displacements along a central flow line of the Mer de Glace measured from SPOT 5 images and from GPS campaign measurements. The time period covered by the GPS (12 August 2003 to 03 September 2003) starts slightly earlier in the summer and includes the August 2003 European heat wave, explaining the faster velocities observed over this period (Berthier et al., 2005). (c) Displacements along transverse profiles AA' and BB' across the glacier. Displacements were stacked within a 12.5 m wide swath. No topography or baseline artifacts can be noticed.

rates on the order of  $\text{mm year}^{-1}$  (Mackey and Roering, 2011; Kelsey, 1980). They are also a major natural hazard in mountainous areas. Slow landslides generally have a complex dynamics highly sensitive to climatic factors, which remain poorly understood (Malet et al., 2003). Assessing how they might evolve with time is therefore a challenge. Conventional geodetic measurements (tachometry, leveling, and GPS geodesy) are commonly used to monitor the temporal evolution of landsliding, but it cannot capture the spatial heterogeneities of mass movement, which may be best assessed using multi-temporal optical data or inSAR (e.g., Delacourt et al., 2007; Roering et al., 2009; Tranelletti et al., 2012). Displacement rates associated with active earthflows cover a large range from a few  $\text{mm year}^{-1}$  to a several  $\text{m h}^{-1}$ . The small scale of these features ( $< 1 \text{ km}^2$ ) and often large surface strain makes geodetic imaging from optical methods particularly appropriate. As an example, Figure 32 shows the cumulative horizontal displacement of the La Valette landslide (southern French Alps,

Ubaye Valley) over about 11 months, measured from the subpixel correlation of two SPOT 5 images (2.5 m GSD) (Leprince et al., 2008a,b). This displacement field is consistent with inSAR measurements of that same area (Squarzone et al., 2003) but provides better spatial resolution and resolves displacements not only in the line of sight direction. A network of benchmarks had been settled for repeated geodetic measurements. Even though the targets were correctly placed according to the morphology of the landslide, it turns out that the most active areas revealed by our technique are not covered by the network and otherwise may have remained undetected. Interestingly, the velocity field does not coincide with the geomorphic expression of the landslide and is highly heterogeneous.

Measurement of surface displacements in 3-D is certainly preferable to study earthflows. Based on the mass conservation principle, 3-D measurements can indeed be used to evaluate the geometry of the slip surface at depth (Casson et al., 2005). This information can then be used to determine the volume

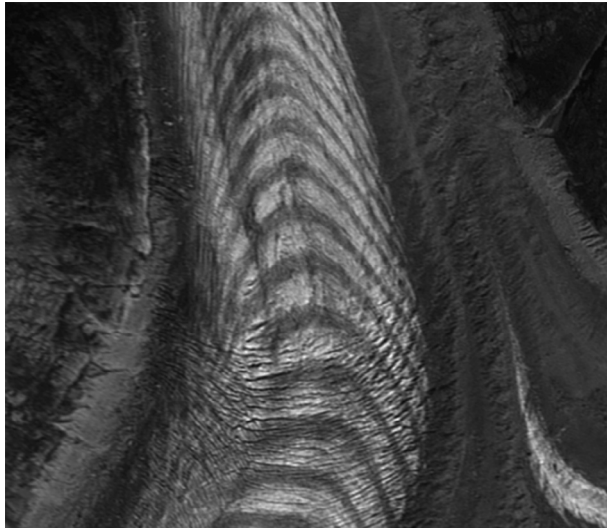


**Figure 31** Close-up view of surface features of the Mer de Glace as seen in the SPOT 5 image of 23 August 2003. Note crevasse, ogive bands, and debris cover.

and mass flux involved in the landslide or the factors controlling the depth extent and kinematics of the earthflow. Such measurements can be achieved from the stereo matching of optical images described in the preceding text, from 3-D matching of point clouds derived from LiDAR measurements or stereo photogrammetry (Teza et al., 2007), from combining 2-D displacements measured from correlation of optical images, or from shaded DEMs followed by DEM differencing (Casson et al., 2005; Daehne and Corsini, 2012; Teza et al., 2007).

For example, Daehne and Corsini (2012) had used terrestrial LiDAR data with sampling density of about  $8\text{--}10$  point  $\text{m}^{-2}$  (GSD of 0.3 m) to study a  $1.5$  km<sup>2</sup> earthflow in the northern Apennines. They first generated DEMs with 1 m posting and measured horizontal displacements from matching slope maps using normalized cross correlation with a  $128 \times 128$ -pixel sliding window. Vertical displacements were determined next from DEM differencing. They were able to measure displacements as large as 60 m. Measurements carried on undeformed areas show that  $1\text{-}\sigma$  uncertainty on the horizontal displacements is on the order of 0.7 m (hence twice the GSD of the original dataset) and also about 0.7 m on the vertical.

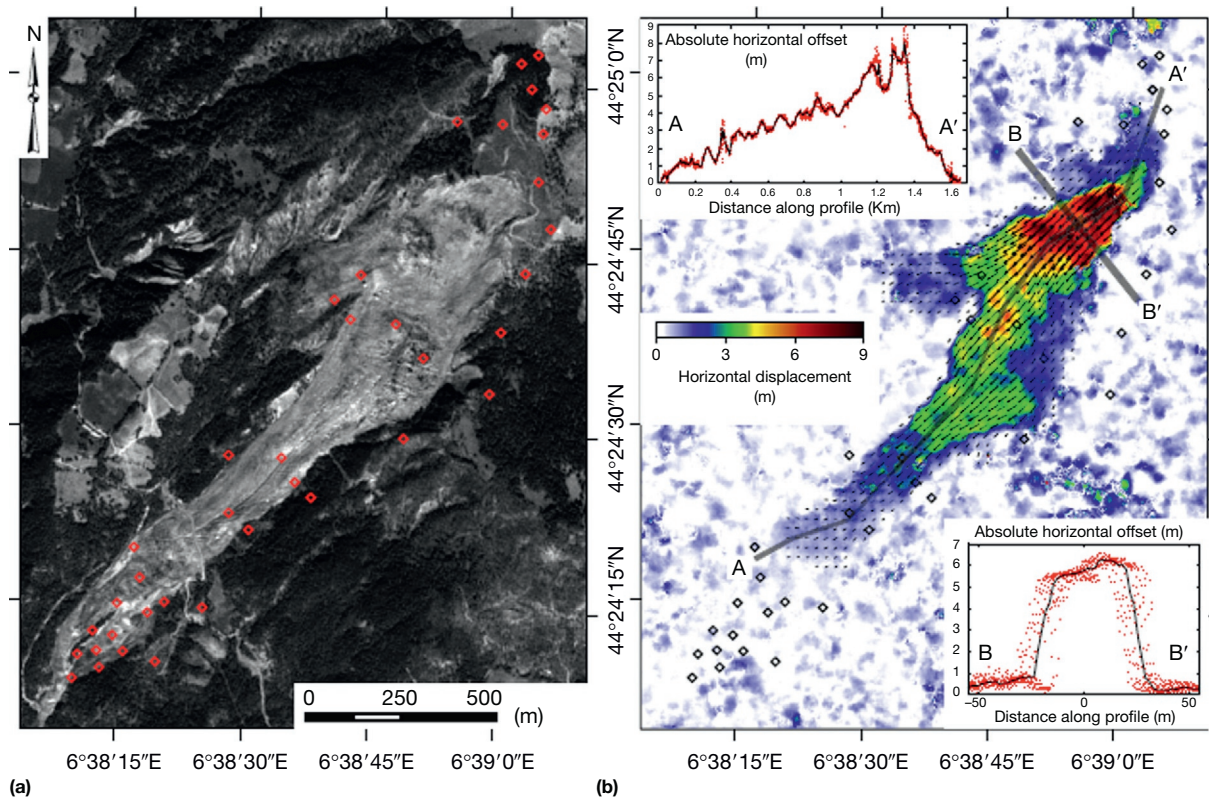


**Figure 32** (a) Orthorectified SPOT 5 image of the La Valette landslide area (southern French Alps, Ubaye Valley). Red diamonds show location of geodetic benchmarks for field geodetic measurements. (b) Amplitude of horizontal displacement and displacement vectors determined from the correlation of two SPOT 5 images with two 2.5 m GSD acquired on 19 September 2003 and 22 August 2004. The maximum displacement is 9 m. Longitudinal and transversal profiles, along AA' and BB', respectively, show the raw data (red points) and the average over a 15 m wide swath (black line). The displacements revealed from the images would have been unnoticed in the geodetic measurements (black diamonds). Modified from Leprince S, et al. (2008) Monitoring earth surface dynamics with optical imagery. *EOS, Transactions, American Geophysical Union* 89(1).

### 3.13.7.3 Dune Migration

Geodetic imaging has proven quite efficient to study sand dunes activity (Bridges et al., 2012; Necsoiu et al., 2009; Vermeesch and Drake, 2008). In this application, the signal that is tracked is actually the change of the topography due to erosion of the stoss slope, the dune slope facing incoming winds, and deposition on the lee slope where sand is avalanching from the crest down the 'slip face.' Due to the coupling between winds and topography, the transport of sediment in sand sheet can be seen as the result of migrating bedforms of various scales (Andreotti et al., 2002b). Large-scale dunes are thus often covered with smaller-scale ripples, which migrate at a higher rate (Figure 33). In this context, the geodetic imaging does not track ground displacements but variation of reflectance induced by topographic slopes because the albedo is approximately uniform. The images have then to be registered to the underlying bedrock. Precise co-registration requires that the images covered bedrock areas. Note that in principle, not all the images have to contain bedrock features if they can be registered through a bundle adjustment procedure. Hence, we are in the situation represented as in Figure 2, but rather than DEM differencing, the technique designed to track ground displacement provides a more appropriate measurement. Image correlation yields the migration rate of the bedforms, which dominate the radiometric texture within the correlation window. This information can then be used directly to compute the sand flux involved in the migration of these bedforms. As an illustration, Figure 34 shows sand ripple migration rates measured from correlating HiRISE images (with GSD of 25 cm) from the Nili Patera dune field on Mars (Bridges et al., 2012). The insets shows the azimuthal distribution of migration direction, which was found to be consistent with the orientation of the barchans. These measurements show that ripple migration rates increase linearly with elevation over the dune in a manner consistent for the dune morphology to be at steady state. Comparing the sand flux involved in the migration of, respectively, the ripples and the whole dunes allowed determining the relative proportion of low-energy sand grains hopping over short distances, the 'reptons,' and the higher-energy 'saltons' that do not contribute much to ripple migration but are involved in whole dune migration. Finally, by

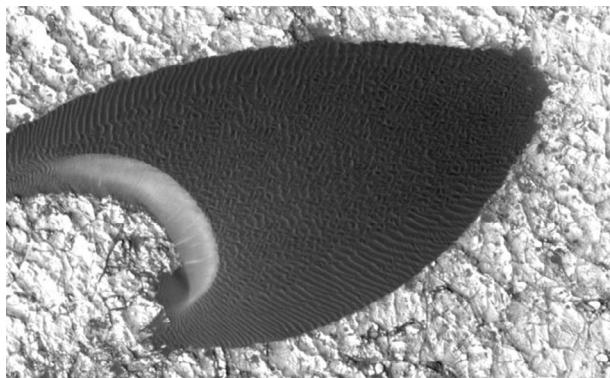


**Figure 33** Close up view of an HiRISE image of a barchan dune at Nili Patera. These images have a GSD of 25 cm, sufficient to resolve the ripples, which adorn the dunes.

comparing the dune volume with the sand flux or the dune width with migration rates, we were able to estimate the turn-over time (the time needed for a complete remobilization of its sand). This is a key quantity to characterize dune activity, which is generally measured on Earth from luminescence or cosmogenic dating (e.g., Bristow et al., 2007; Singhvi and Porat, 2008; Vermeesch et al., 2010).

This example, together with a number of other studies of dune migration using remote sensing (Hugenholtz et al., 2012), demonstrates the potential of these techniques to monitor eolian activity. This is of major interest as the data provided through these techniques would help address fundamental questions in eolian geomorphology (Bourke et al., 2010; Titus et al., 2008). Such data would in particular allow validation and calibration of numerical models of sand transport and dune dynamics (e.g., Claudin and Andreotti, 2006; Elbelrhiti et al., 2008; Fenton and Richardson, 2001; Kok and Renno, 2009; Richardson et al., 2007); they would complement geologic indicators of dune dynamics to help infer the time evolution of eolian bedforms and past climate change (Beveridge et al., 2006; Hayward et al., 2009) and help assess the impact of current climate change on dune activity (in relation to wind regime, vegetation, and humidity changes) and atmospheric dust. They would also improve our understanding of how various dune forms (e.g., simple and compound barchans and transverse and longitudinal linear dunes) and their morphometric characteristics emerge and evolve due to their interactions and in relation to the wind regime and boundary conditions (Andreotti et al., 2002a,b; Bristow et al., 2007; Ewing and Kocurek, 2010; Reffet et al., 2010).

### 3.13.8 Conclusion

Thanks to the increasing availability of LiDAR dataset, high-quality optical satellite images, and advances in optical image modeling and matching techniques, it is now possible to detect and measure accurately changes of the Earth's surface due to a variety of processes. These techniques cannot compete with conventional geodesy with regard to the accuracy of pointwise measurements, but they provide a spatial coverage that would be impossible to match with ground-based techniques.

These techniques are sufficiently mature that they can be used to address a variety of topics in Earth sciences and for disaster mitigation. They can be used in particular to provide rapid information on ground deformation and damages in the epicentral area of large earthquakes, to measure the Earth's surface changes due to catastrophic and slow-moving landslides, to monitor ice flow and the mass balance of mountain glaciers, or to monitor eolian sand transport. There are a number of limiting factors: passive optical imaging works only at daytime under clear sky condition to limit occlusions by clouds; misregistration due to jitter, CCD and scan artifacts; image matching failure; view angles must differ by less than about 10° or images must be augmented with stereo acquisitions to compensate parallax artifacts.

Various techniques can be used to match passive optical images and generally allow determining horizontal offsets with an accuracy better than 1/10th the pixel size with typically a

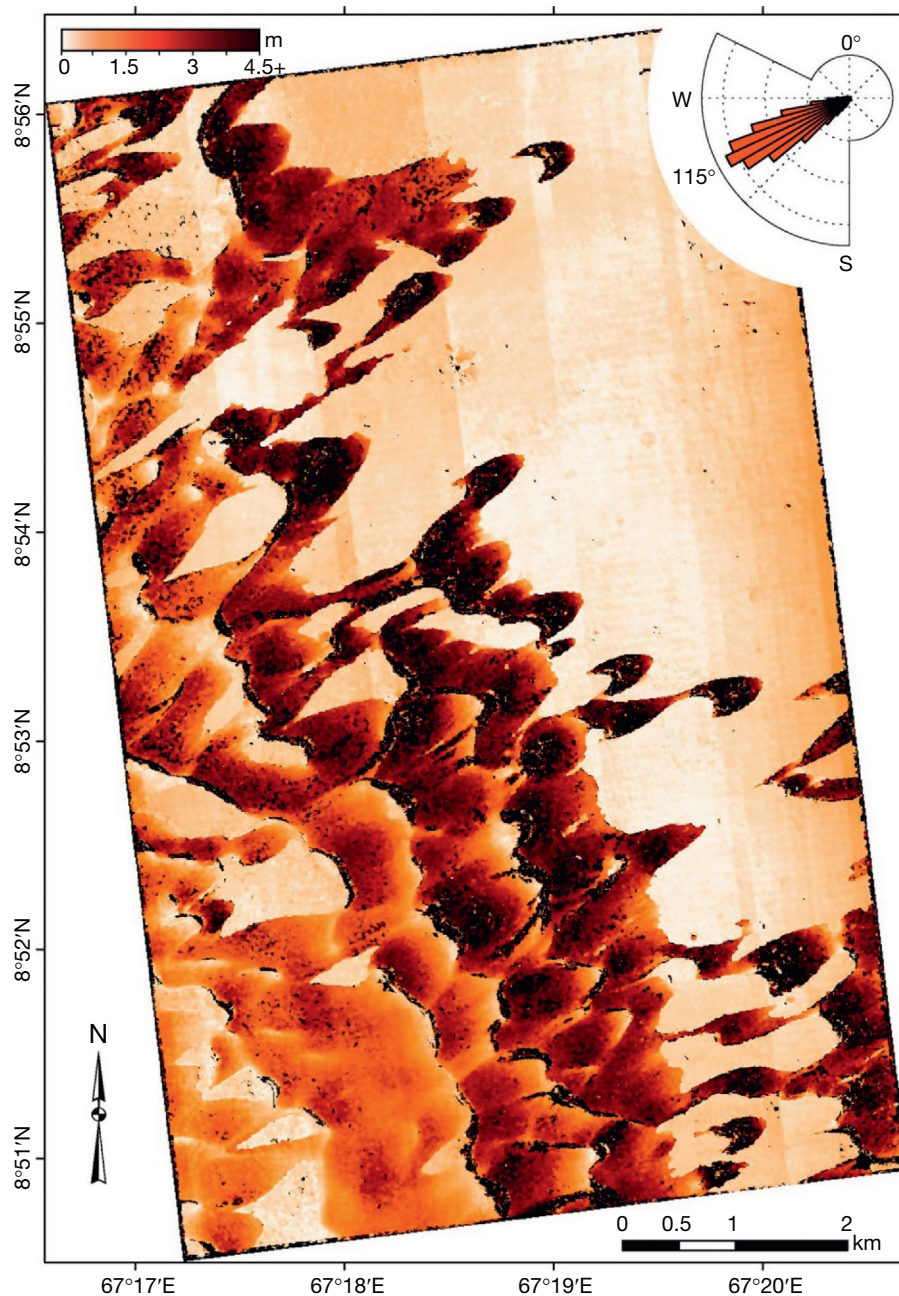


**Figure 34** Amplitude of sand ripple migration in the Nili Patera dune field on Mars obtained from the correlation of two HiRISE images 3 months apart (Bridges et al., 2012). The wind rise in inset represents the azimuthal distribution of ripple displacement vectors. Box shows location of HiRISE close-up view shown in Figure 32

$32 \times 32$ -pixel window and images with ground sampling of 1 m and lower, and view angles differing by less than about  $10^\circ$ . These techniques perform less well on images with submetric resolution and view angles differing by more than  $10^\circ$  as disparity gradients tend to be larger and more variable locally especially with rugged topography or in urban areas. The assumptions that the transformation field can be approximated by a homogeneous rotation globally combined with a locally homogeneous translation (at the scale of the matching window generally used for regularization) does not hold

anymore. Geodetic imaging would therefore benefit from more sophisticated matching techniques. It would improve the performance achievable with high-resolution ( $<1$  m) images or with lower-resolution images but large difference of view angles ( $>10^\circ$ ).

Thanks to improved attitude control of most modern satellite imaging systems and the optimization techniques described in this chapter, jitter artifacts have been reduced considerably to be typically subpixel. These artifacts are often the major source of errors over areas with good correlation.

CCD artifacts can in principle be measured and calibrated with accuracy on the order of the percent of the pixel size, but this procedure is heavy and requires appropriate calibration datasets.

Repeating LiDAR measurements offer the possibility to measure vertical displacement with <10 cm accuracy. Horizontal displacements might also be measured from 2-D or 3-D matching of the point cloud but errors can be as large, as the GSD due to misregistrations (mostly jitter during image acquisition). It is hard to correct for these artifacts in a post-processing step. Controlling the orientation model of LiDAR acquisition is therefore required to improve the accuracy of geodetic imaging with such data. Measurements in 3-D are best achieved with passive optical imaging at the moment using a full 3-D co-registration and correlation scheme described in this chapter. Future efforts should focus on improving the capability of these techniques for 3-D matching, the development of more robust matching algorithms that would allow matching accurately high-resolution images.

The temporal resolution of geodetic imaging from optical techniques is currently limited. Optical imaging from satellite is generally Sun-synchronous and on near-polar orbits leading to a typical revisit time at nadir on the order of several months. Even with steering capability, the repeatability is limited as high incidence angles viewed are impaired by occlusions. Repeatability is improved when images from different imaging systems can be combined. This approach requires matching to be performed on ground-projected images following the procedures described in this chapter. In the future, higher temporal resolution will be available as the number of Earth-observing optical imaging system increases. In principle, such systems might be used opportunistically to measure very transient deformation. For example, it has already been proved that oceanic wave propagation can be tracked from current systems, taking advantage of the fact that the CCD arrays of multispectral imaging systems are generally offset in the focal plane of the telescope and image the same spot on the ground at different times (de Michele et al., 2012). It is probable that video imaging system will become operational in the near future opening the possibility for more systematic monitoring of transient phenomena such as seismic waves or catastrophic landslides (Michel et al., 2013).

## References

- Abrams M (2000) The advanced spaceborne thermal emission and reflection radiometer (ASTER): Data products for the high spatial resolution imager on NASA's Terra platform. *International Journal of Remote Sensing* 21(5): 847–859.
- Altamimi Z, et al. (2002) ITRF2000: A new release of the International Terrestrial Reference frame for earth science applications. *Journal of Geophysical Research-Solid Earth* 107(B10).
- Andreotti B, et al. (2002a) Selection of dune shapes and velocities—Part 2: A two-dimensional modelling. *European Physical Journal B* 28(3): 341–352.
- Andreotti B, et al. (2002b) Selection of dune shapes and velocities—Part 1: Dynamics of sand, wind and barchans. *European Physical Journal B* 28(3): 321–339.
- Arnold K (1967) Use of satellites for geodetic studies. *Space Science Reviews* 7(1): 4–68.
- Arrowsmith JR and Zielke O (2009) Tectonic geomorphology of the San Andreas Fault zone from high resolution topography: An example from the Cholame segment. *Geomorphology* 113(1–2): 70–81.
- Aryal A, et al. (2012) Displacement fields from point cloud data: Application of particle imaging velocimetry to landslide geodesy. *Journal of Geophysical Research-Earth Surface* 117.
- Avouac JP, et al. (2006) The 2005, M-w 7.6 Kashmir earthquake: Sub-pixel correlation of ASTER images and seismic waveforms analysis. *Earth and Planetary Science Letters* 249(3–4): 514–528.
- Ayoub F, et al. (2008) Influence of camera distortions on satellite image registration and change detection applications. In: *Proc. IGARSS, Boston, MA, USA, July 2008*.
- Ayoub F, et al. (2009) Co-registration and correlation of aerial photographs for ground deformation measurements. *ISPRS Journal of Photogrammetry and Remote Sensing* 64(6): 551–560.
- Baltsavias EP (1999) Airborne laser scanning: Basic relations and formulas. *ISPRS Journal of Photogrammetry and Remote Sensing* 54(2–3): 199–214.
- Barnea DI and Silverma HF (1972) Class or algorithms for fast digital image registration. *IEEE Transactions on Computers, C* 21(2): 179–186.
- Beckouche S, et al. (2011) Robust Outliers Detection in Image Point Matching.
- Bernard S, et al. (2007) Kinematics of fault-related folding derived from a sandbox experiment. *Journal of Geophysical Research-Solid Earth* 112(B3).
- Berthier E, et al. (2005) Surface motion of mountain glaciers derived from satellite optical imagery. *Remote Sensing of Environment* 95(1): 14–28.
- Berthier E, et al. (2006) Biases of SRTM in high-mountain areas: Implications for the monitoring of glacier volume changes. *Geophysical Research Letters* 33(8).
- Besl PJ and McKay ND (1992) A method for registration of 3-D shapes. *IEEE Transactions on Pattern Analysis and Machine Intelligence* 14(2): 239–256.
- Beveridge C, et al. (2006) Development of spatially diverse and complex dune-field patterns: Gran Desierto Dune Field, Sonora, Mexico. *Sedimentology* 53(6): 1391–1409.
- Bevis M, Hudnut K, Sanchez R, et al. (2005) The B4 project: Scanning the San Andreas and San Jacinto fault zones. *EOS Transactions AGU* 86: 52, abstract H34B-01.
- Binet R and Bollinger L (2005) Horizontal coseismic deformation of the 2003 Bam (Iran) earthquake measured from SPOT-5 THR satellite imagery. *Geophysical Research Letters* 32: L02307. <http://dx.doi.org/10.1029/2004GL021897>.
- Bishop MP, et al. (2012) Geospatial technologies and digital geomorphological mapping: Concepts, issues and research. *Geomorphology* 137(1): 5–26.
- Borsa A and Minster JB (2012) Rapid determination of near-fault earthquake deformation using differential LiDAR. *Bulletin of the Seismological Society of America* 102(4): 1335–1347.
- Bourke MC, et al. (2010) Extraterrestrial dunes: An introduction to the special issue on planetary dune systems. *Geomorphology* 121(1–2): 1–14.
- Brecher HH (1986) Surface velocity determination on large polar glaciers by aerial photogrammetry. *Annals of Glaciology* 8: 22–26.
- Bridges NT, et al. (2012) Earth-like sand fluxes on Mars. *Nature* 485(7398): 339–342.
- Bristow CS, et al. (2007) Age and dynamics of linear dunes in the Namib Desert. *Geology* 35(6): 555–558.
- Broxton MJ, et al. (2009) 3D Lunar Terrain Reconstruction from Apollo Images. In: *Bebis G, et al. (eds.) Advances in Visual Computing*, pp. 710–719. Berlin/Heidelberg: Springer, Proceedings, Part 1.
- Buades A, et al. (2008) Nonlocal image and movie denoising. *International Journal of Computer Vision* 76(2): 123–139.
- Burbank D and Anderson R (2001) *Tectonic Geomorphology*, p. 274. Oxford: Blackwell Science.
- Carter WE, et al. (2007) Geodetic laser scanning. *Physics Today* 60(12): 41–47.
- Casson B, et al. (2005) Contribution of multi-temporal remote sensing images to characterize landslide slip surface—Application to the La Clapiere landslide (France). *Natural Hazards and Earth System Sciences* 5(3): 425–437.
- Chen Y and Medioni G (1992) Object modeling by registration of multiple range images. *Image and Vision Computing* 10(3): 145–155.
- Chen Y-G, et al. (2001) Surface rupture of 1999 Chi-Chi earthquake yields insights on active tectonics of Central Taiwan. *Bulletin of the Seismological Society of America* 91(5): 977–985.
- Chini M, et al. (2011) Co-seismic surface effects from very high resolution panchromatic images: The case of the 2005 Kashmir (Pakistan) earthquake. *Natural Hazards and Earth System Sciences* 11(3): 931–943.
- Claudin P and Andreotti B (2006) A scaling law for aeolian dunes on Mars, Venus, Earth, and for subaqueous ripples. *Earth and Planetary Science Letters* 252(1–2): 30–44.
- Copley A, Avouac JP, Hollingsworth J, and Leprince S (2011) The 2001 M(w) 7.6 Bhuj earthquake, low fault friction, and the crustal support of plate driving forces in India. *Journal of Geophysical Research-Solid Earth* 116. <http://dx.doi.org/10.1029/2010jb008137>.
- Copley A, et al. (2012) Constraints on fault and lithosphere rheology from the coseismic slip and postseismic afterslip of the 2006 M(w)7.0 Mozambique earthquake. *Journal of Geophysical Research-Solid Earth* 117.

- Corsini A, et al. (2009) Estimating mass-wasting processes in active earth slides—Earth flows with time-series of high-resolution DEMs from photogrammetry and airborne LiDAR. *Natural Hazards and Earth System Sciences* 9(2): 433–439.
- Crippen RE (1992) Measurement of subresolution terrain displacements using SPOT panchromatic imagery. *Episodes* 15(1): 56–61.
- Daehne A and Corsini A (2012) Kinematics of active earthflows revealed by digital image correlation and DEM subtraction techniques applied to multi-temporal LiDAR data. *Earth Surface Processes and Landforms* 38: 640–654.
- de Michele M, et al. (2012) Direct measurement of ocean waves velocity field from a single SPOT-5 dataset. *Remote Sensing of Environment* 119: 266–271.
- Debella-Gilo M and Kaab A (2011) Sub-pixel precision image matching for measuring surface displacements on mass movements using normalized cross-correlation. *Remote Sensing of Environment* 115(1): 130–142.
- Debella-Gilo M and Kaab A (2012) Measurement of surface displacement and deformation of mass movements using least squares matching of repeat high resolution satellite and aerial images. *Remote Sensing* 4(1): 43–67.
- Delacourt C, et al. (2007) Remote-sensing techniques for analysing landslide kinematics: A review. *Bulletin de la Societe Geologique de France* 178(2): 89–100.
- Dominguez S, et al. (2003) Horizontal coseismic deformation of the 1999 Chi-Chi earthquake measured from SPOT satellite images: Implications for the seismic cycle along the western foothills of central Taiwan. *Journal of Geophysical Research-Solid Earth* 108(B2), art. no.-2083.
- Dudderar TD and Simpkins PG (1977) Laser speckle photography in a fluid medium. *Nature* 270(5632): 45–47.
- Eibelrhiti H, et al. (2008) Barchan dune corridors: Field characterization and investigation of control parameters. *Journal of Geophysical Research-Earth Surface* 113(F2).
- Ewing RC and Kocurek G (2010) Aeolian dune-field pattern boundary conditions. *Geomorphology* 114(3): 175–187.
- Farr TG, et al. (2007) The shuttle radar topography mission. *Reviews of Geophysics* 45(2).
- Fenton LK and Richardson MI (2001) Martian surface winds: Insensitivity to orbital changes and implications for aeolian processes. *Journal of Geophysical Research-Planets* 106(E12): 32885–32902.
- Fischler MA and Bolles RC (1981) Random sample consensus—A paradigm for model-fitting with applications to image-analysis and automated cartography. *Communications of the ACM* 24(6): 381–395.
- Forstner W and Gulch E (1987) A fast operator for detection and precise location of distinct points, corners and centres of circular features. In: *Proceedings of ISPRS Intercommission Conference on Fast Processing of Photogrammetric Data*, Interlaken.
- French JR (2003) Airborne LiDAR in support of geomorphological and hydraulic modelling. *Earth Surface Processes and Landforms* 28(3): 321–335.
- Grenander U and Miller MI (1998) Computational anatomy: An emerging discipline. *Quarterly of Applied Mathematics* 56(4): 617–694.
- Hayward RK, et al. (2009) Aeolian dunes as ground truth for atmospheric modeling on Mars. *Journal of Geophysical Research-Planets* 114.
- Heid T and Kaab A (2012) Evaluation of existing image matching methods for deriving glacier surface displacements globally from optical satellite imagery. *Remote Sensing of Environment* 118: 339–355.
- Hild F and Roux S (2006) Digital image correlation: From displacement measurement to identification of elastic properties—A review. *Strain* 42(2): 69–80.
- Hirschmuller H (2005) Accurate and efficient stereo processing by semi-global matching and mutual information. In: Schmid C, et al. (eds.), *2005 IEEE Computer Society Conference on Computer Vision and Pattern Recognition, Vol. 2, Proceedings*, pp. 807–814.
- Hirschmuller H and Scharstein D (2009) Evaluation of stereo matching costs on images with radiometric differences. *IEEE Transactions on Pattern Analysis and Machine Intelligence* 31(9): 1582–1599.
- Horn BKP and Schunck BG (1981) Determining optical flow. *Artificial Intelligence* 17: 185–203.
- Hudnut KW, et al. (2002) High-resolution topography along surface rupture of the 16 October 1999 Hector Mine, California, earthquake (M-w 7.1) from airborne laser swath mapping. *Bulletin of the Seismological Society of America* 92(4): 1570–1576.
- Hughenoltz CH, et al. (2012) Remote sensing and spatial analysis of aeolian sand dunes: A review and outlook. *Earth-Science Reviews* 111(3–4): 319–334.
- Iwasaki A and Fujisada H (2003) Image correlation tool for ASTER geometric validation. In: Fujisada H, et al. (eds.) *Sensors, Systems and Next-Generation Satellites VI*, pp.111–120, SPIE Press.
- Jensen JR (2006) *Remote Sensing of the Environment: An Earth Resource Perspective*. Upper Saddle River, NJ: Prentice Hall.
- Kääb A, et al. (1997) Analysing the creep of mountain permafrost using high precision aerial photogrammetry: 25 years of monitoring Gruben Rock Glacier, Swiss Alps. *Permafrost and Periglacial Processes* 8(4): 409–426.
- Karabacak VKV, et al. (2011) Monitoring aseismic surface creep along the North Anatolian Fault (Turkey) using ground-based LiDAR. *Earth and Planetary Science Letters* 304(1–2): 64–70.
- Kelsey HM (1980) A sediment budget and an analysis of geomorphic process in the van-Duzen River Basin, North Coastal California, 1941–1975 – Summary. *Geological Society of America Bulletin* 91(4): 190–195.
- Kirby E and Whipple KX (2012) Expression of active tectonics in erosional landscapes. *Journal of Structural Geology* 44: 54–75.
- Klinger Y, et al. (2006) Evidence for an earthquake barrier model from Mw similar to 7.8 Kokoxii (Tibet) earthquake slip-distribution. *Earth and Planetary Science Letters* 242(3–4): 354–364.
- Kok JF and Renno NO (2009) A comprehensive numerical model of steady state saltation (COMSALT). *Journal of Geophysical Research-Atmospheres* 114. <http://dx.doi.org/10.1029/2009jd011702>.
- Konca AO, et al. (2010) Rupture Process of the 1999 M-w 7.1 Duzce earthquake from joint analysis of SPOT, GPS, InSAR, strong-motion, and teleseismic data: A supershear rupture with variable rupture velocity. *Bulletin of the Seismological Society of America* 100(1): 267–288.
- Kovalovsky J and Barlier F (1967) Geodesie terrestre et geodesie par satellites. *Space Science Reviews* 7(1): 69–134.
- Krabill WB, et al. (1984) Airborne laser topographic mapping results. *Photogrammetric Engineering and Remote Sensing* 50(6): 685–694.
- Laussedat A (1854) Mémoire sur l'emploi de la chambre claire dans les reconnaissances topographiques. *Comptes Rendus Hebdomadaires Des Seances De L Academie Des Sciences* 16.
- Laussedat A (1859) Mémoire sur l'emploi de la photographie dans la levée des plans. *Comptes Rendus Hebdomadaires Des Seances De L Academie Des Sciences* 49: 732–734.
- Leprince S, et al. (2007) Automatic and precise orthorectification, coregistration, and subpixel correlation of satellite images, application to ground deformation measurements. *IEEE Transactions on Geoscience and Remote Sensing* 45(6): 1529–1558.
- Leprince S, et al. (2008a) Monitoring earth surface dynamics with optical imagery. *Eos, Transactions American Geophysical Union* 89(1).
- Leprince S, et al. (2008b) In-flight CCD distortion calibration for pushbroom satellites based on subpixel correlation. *IEEE Transactions on Geoscience and Remote Sensing* 46(9): 2675–2683.
- Leprince S, et al. (2010) Rigorous adaptive resampling for high resolution image warping. In: *IGARSS: 2010 IEEE International Geoscience and Remote Sensing Symposium*, pp. 1943–1946.
- Low KL and Lastra A (2003) Reliable and rapidly-converging ICP algorithm using multiresolution smoothing. In: Kawada S (ed.) *Fourth International Conference on 3-D Digital Imaging and Modeling, Proceedings*, pp 171–178.
- Lowe DG (2004) Distinctive image features from scale-invariant keypoints. *International Journal of Computer Vision* 60(2): 91–110.
- Lucas D and Kanade T (1981) An iterative image registration technique with an application to stereo vision. In: *IJCAI Proceedings of the 7th International Conference on Artificial Intelligence*. San Francisco, CA: Morgan Kaufmann Publishers.
- Lucchitta BK and Ferguson HM (1986) Antarctica—Measuring glacier velocity from satellite images. *Science* 234(4780): 1105–1108.
- Mackey BH and Roering JJ (2011) Sediment yield, spatial characteristics, and the long-term evolution of active earthflows determined from airborne LiDAR and historical aerial photographs, Eel River, California. *Geological Society of America Bulletin* 123(7–8): 1560–1576.
- Mackey BH, et al. (2009) Long-term kinematics and sediment flux of an active earthflow, Eel River, California. *Geology* 37(9): 803–806.
- Malet J-P, et al. (2003) Soil surface characteristics influence on infiltration in black marls: Application to the Super-Sauze earthflow (Southern Alps, France). *Earth Surface Processes and Landforms* 28(5): 547–564.
- Marcello J, et al. (2008) Motion estimation techniques to automatically track oceanographic thermal structures in multisensor image sequences. *IEEE Transactions on Geoscience and Remote Sensing* 46(9): 2743–2762.
- Massonnet D and Feigl KL (1998) Radar interferometry and its application to changes in the Earth's surface. *Reviews of Geophysics* 36(4): 441–500.
- McKean J and Roering J (2004) Objective landslide detection and surface morphology mapping using high-resolution airborne laser altimetry. *Geomorphology* 57(3–4): 331–351.

- Michel R and Avouac JP (2002) Deformation due to the 17 August 1999 Izmit, Turkey, earthquake measured from SPOT images. *Journal of Geophysical Research-Solid Earth* 107(B4), art. no. 2062.
- Michel R and Avouac JP (2006) Coseismic surface deformation from air photos: The Kickapoo step over in the 1992 Landers rupture. *Journal of Geophysical Research-Solid Earth* 111(B3).
- Michel R, et al. (1999) Measuring near field coseismic displacements from SAR images: Application to the Landers earthquake. *Geophysical Research Letters* 26(19): 3017–3020.
- Michel R, et al. (2013) A geostationary optical seismometer, proof of concept. *IEEE Transactions on Geoscience and Remote Sensing* 51(1): 695–703.
- Necsoiu M, et al. (2009) Monitoring migration rates of an active subarctic dune field using optical imagery. *Remote Sensing of Environment* 113(11): 2441–2447.
- Nissen E, et al. (2012) Three-dimensional surface displacements and rotations from differencing pre- and post-earthquake LiDAR point clouds. *Geophysical Research Letters* 39.
- Okada Y (1985) Surface deformation to shear and tensile faults in a half space. *Bulletin of the Seismological Society of America* 75: 1135–1154.
- Oppikofer T, et al. (2009) Characterization and monitoring of the Aknes rockslide using terrestrial laser scanning. *Natural Hazards and Earth System Sciences* 9(3): 1003–1019.
- Oskin ME, et al. (2012) Near-field deformation from the El Mayor–Cucapah earthquake revealed by differential LiDAR. *Science* 335(6069): 702–705.
- Phillips DA, Jackson ME, and Meertens C (2008) GeoEarthScope airborne LiDAR and satellite InSAR imagery. *EOS Transactions AGU* 89: 53, abstract G53A-0630.
- Pierrot-Deseilligny M and Paparoditis N (2006) A multiresolution and optimization-based image matching approach: An application to surface reconstruction from SPOT5-HRS stereo imagery. In: *ISPRS Workshop on Topographic Mapping from Space (With Special Emphasis on Small Satellites)* Ankara: IAPRS.
- Prentice CS, Crosby CJ, Harding DJ, et al. (2003) Northern California LiDAR data: A tool for mapping the San Andreas fault and Pleistocene marine terraces in heavily vegetated terrain. *EOS Transactions, AGU* 84: 46, abstract G12A-06.
- Reffet E, et al. (2010) Formation and stability of transverse and longitudinal sand dunes. *Geology* 38(6): 491–494.
- Richardson MI, et al. (2007) PlanetWRF: A general purpose, local to global numerical model for planetary atmospheric and climate dynamics. *Journal of Geophysical Research-Planets* 112(E9).
- Roering JJ, et al. (2009) Using DInSAR, airborne LiDAR, and archival air photos to quantify landsliding and sediment transport. *Geophysical Research Letters* 36.
- Sabater N, et al. (2012) Contrast invariant and affine sub-pixel optical flow. In: *19th IEEE International Conference on Image Processing (ICIP)*, pp. 53–56.
- Scambos TA, et al. (1992) Application of image cross-correlation to the measurement of glacier velocity using satellite image data. *Remote Sensing of Environment* 42(3): 177–186.
- Scharstein D and Szeliski R (2002) A taxonomy and evaluation of dense two-frame stereo correspondence algorithms. *International Journal of Computer Vision* 47(1–3): 7–42.
- Scherler D, et al. (2008) Glacier-surface velocities in alpine terrain from optical satellite imagery—Accuracy improvement and quality assessment. *Remote Sensing of Environment* 112(10): 3806–3819.
- Scherler D, et al. (2011) Spatially variable response of Himalayan glaciers to climate change affected by debris cover. *Nature Geoscience* 4(3): 156–159.
- Shan S, et al. (2007) Kinematic GPS solutions for aircraft trajectories: Identifying and minimizing systematic height errors associated with atmospheric propagation delays. *Geophysical Research Letters* 34(23).
- Sieh K, et al. (1993) Near-field investigations of the Landers earthquake sequence April to July 1992. *Science* 260: 171–176.
- Singhvi AK and Porat N (2008) Impact of luminescence dating on geomorphological and palaeoclimate research in drylands. *Boreas* 37(4): 536–558.
- Slatton KC, et al. (2007) Airborne laser swath mapping: Achieving the resolution and accuracy required for geosurficial research. *Geophysical Research Letters* 34(23).
- Squarozzi C, et al. (2003) Nine years of spatial and temporal evolution of the La Valette landslide observed by SAR interferometry. *Engineering Geology* 68(1–2): 53–66.
- Sun D, et al. (2010) Secrets of optical flow estimation and their principles. In: *2010 IEEE Conference on Computer Vision and Pattern Recognition*, pp. 2432–2439.
- Tarolli P, et al. (2009) Understanding earth surface processes from remotely sensed digital terrain models. *Geomorphology* 113(1–2): 1–3.
- Taylor MH, et al. (2008) Detecting co-seismic displacements in glaciated regions: An example from the great November 2002 Denali earthquake using SPOT horizontal offsets. *Earth and Planetary Science Letters* 270(3–4): 209–220.
- Teza G, et al. (2007) Terrestrial laser scanner to detect landslide displacement fields: A new approach. *International Journal of Remote Sensing* 28(16): 3425–3446.
- Titus TN, et al. (2008) Priorities for future research on planetary dunes. *Eos, Transactions American Geophysical Union* 89(45): 447–448.
- Travelletti J, et al. (2012) Correlation of multi-temporal ground-based optical images for landslide monitoring: Application, potential and limitations. *ISPRS Journal of Photogrammetry and Remote Sensing* 70: 39–55.
- Treiman J, et al. (2002) Primary surface rupture associated with the M 7.1 16 October 1999 Hector Mine Earthquake, San Bernardino County, California. *Bulletin of the Seismological Society of America* 92(4): 1171–1191.
- Vadon H and Massonnet D (2000) Earthquake displacement fields mapped by very precise correlation. Complementarity with radar interferometry, Igarss 2000. In: *IEEE 2000 International Geoscience and Remote Sensing Symposium, Vol. I–VI, Proceedings*, pp. 2700–2702.
- Van Puymbroeck N, et al. (2000) Measuring earthquakes from optical satellite images. *Applied Optics* 39(20): 3486–3494. <http://dx.doi.org/10.1029/2008gl035921>.
- Vermeesch P and Drake N (2008) Remotely sensed dune celerity and sand flux measurements of the world's fastest barchans (Bodele, Chad). *Geophysical Research Letters* 35(24). <http://dx.doi.org/10.1029/2008g035921>.
- Vermeesch P, et al. (2010) Sand residence times of one million years in the Namib Sand Sea from cosmogenic nuclides. *Nature Geoscience* 3(12): 862–865.
- Wei SJ, et al. (2011) Superficial simplicity of the 2010 El Mayor–Cucapah earthquake of Baja California in Mexico. *Nature Geoscience* 4(9): 615–618.
- Willert CE and Gharib M (1991) Digital image particle image velocimetry. *Experiments in Fluids* 10(4): 181–193.
- Wolf PR and Dewitt BA (2000) *Elements of Photogrammetry with Application in GIS*, 3rd edn. India: McGraw-Hill Education.
- Woolard JW and Colby JD (2002) Spatial characterization, resolution, and volumetric change of coastal dunes using airborne LiDAR: Cape Hatteras, North Carolina. *Geomorphology* 48(1–3): 269–287.
- Yeats RS, et al. (1996) *The Geology of Earthquakes*, p. 568. New York: Oxford University Press.
- Yu S-B, et al. (2001) Preseismic deformation and coseismic displacements associated with the 1999 Chi-Chi, Taiwan, Earthquake. *Bulletin of the Seismological Society of America* 91(5): 995–1012.
- Zabih R and Woodfill J (1994) *Paper Presented at 3rd European Conf. Computer Vision, Stockholm*.
- Zhang ZY (1994) In: Iterative point matching for registration of free-form curves and surfaces. *International Journal of Computer Vision* 13(2): 119–152.
- Zielke O, et al. (2010) Slip in the 1857 and earlier large earthquakes along the Carrizo Plain, San Andreas Fault. *Science* 327(5969): 1119–1122.
- Zielke O, et al. (2012) High-resolution topography-derived offsets along the 1857 Fort Tejon Earthquake Rupture Trace, San Andreas Fault. *Bulletin of the Seismological Society of America* 102(3): 1135–1154.
- Zitova B and Flusser J (2003) Image registration methods: A survey. *Image and Vision Computing* 21(11): 977–1000.